9-5-2013

Adatom Emission From Nanoparticles: Implications for Ostwald Ripening

Tyne Johns

Tyne Johns
Candidate

Chemical and Nuclear Engineering
Department

This dissertation is approved, and it is acceptable in quality and form for publication:

Approved by the Dissertation Committee:

Abhaya K. Datye, Chairperson

Timothy L. Ward

Boris Kiefer

Chang H. Kim

ADATOM EMISSION FROM NANOPARTICLES: IMPLICATIONS FOR OSTWALD RIPENING

by

TYNE RICHELE JOHNS

B.S., Chemical Engineering, University of New Mexico, 2009

DISSERTATION

Submitted in Partial Fulfillment of the
Requirements for the Degree of

Doctor of Philosophy

Engineering

The University of New Mexico
Albuquerque, New Mexico

July, 2013

ACKNOWLEDGEMENTS

I am especially grateful for all of the guidance and support I have received over the past four years from Professor Abhaya K. Datye, my advisor and dissertation committee chair. The skills that I have acquired during my time as a graduate student will be instrumental throughout my career. I would also like to thank my committee members, Professor Boris Kiefer (New Mexico State University), Dr. Chang H. Kim (General Motors Global R&D), and Professor Timothy L. Ward (University of New Mexico), for the numerous discussions we have had pertaining to this doctoral research and for their recommendations on my project. I greatly appreciate the synthesis of all model catalysts by Dr. Ronald S. Goeke at Sandia National Laboratories. Dr. Jeffrey T. Miller (Argonne National Laboratory) and Dr. Jason R. Gaudet (University of New Mexico but currently a post-doc at the University of Michigan) provided essential guidance in X-ray absorption spectroscopy (XAS). I would also like to thank Dr. Eric A. Stach (Brookhaven National Laboratory), Professor J.W. (Hans) Niemantsverdriet, Professor Peter C. Thüne, and the rest of the research group I had the privilege of working with at Eindhoven University of Technology in The Netherlands. I enjoyed working with the members of the Chemical and Materials Systems Lab at General Motors Global R&D. Thank you to Michael P. Balogh for his expertise in energy dispersive X-ray spectroscopy (EDS) and aberration-corrected scanning transmission electron microscopy (AC-STEM). His assistance with EDS was immensely helpful when quantifying emission of nanoparticles on model catalysts. I would like to thank Dr. Ying-Bing Jiang (University of New Mexico) for teaching me how to use the high resolution TEM and for being available every time I had a TEM-related question over the past several years. I would like to acknowledge Nalin Fernando (New Mexico State University) for his involvement with this project as well as the members of the catalysis research group at the University of New Mexico, especially Dr. Andrew T. De La Riva, Dr. Hien Pham, and Eric J. Peterson, for their mentoring in the areas of high resolution transmission electron microscopy (HR-TEM), scanning electron microscopy (SEM), X-ray diffraction (XRD), and XAS. I would also like to thank Heather Armstrong for her assistance with everything relating to my minor in Nano Science and Micro Systems.

I acknowledge financial support from the following grants: NSF GOALI CBET-1067803, NSF IGERT DGE-0504276, and NSF PIRE OISE-0730277. Portions of this work were performed at beamline 10-ID-B (MRCAT) of the Advanced Photon Source at Argonne National Laboratory. MRCAT operations are supported by the Department of Energy and the MRCAT member institutions. Use of the Advanced Photon Source was supported by the U.S. Department of Energy, Office of Science, Office of Basic Energy Sciences, under Contract No. DE-AC02-06CH11357. Jeffrey T. Miller is supported as part of the Institute for Atom-Efficient Chemical Transformations (IACT), an Energy Frontier Research Center funded by the U.S. Department of Energy, Office of Science, Office of Basic Energy Sciences. Some of this work was performed using the JEOL JEM 2100F AC at General Motors Global R&D, and some work was performed using the FEI Titan 80-300 environmental transmission electron microscope (E-TEM) at the Center for Functional Nanomaterials at Brookhaven National Laboratory, supported by the U.S. Department of Energy, Office of Basic Energy Sciences, under contract No. DE-AC02-98CH10886. I also acknowledge NSF support for acquisition of the XRD via the Major Research

Instrumentation grant CBET-0960256. I would also like to acknowledge Sandia National Laboratories for the use of the 10kV Temescal electron beam evaporator. Sandia National Laboratories is a multi-program laboratory managed and operated by Sandia Corporation, a wholly owned subsidiary of Lockheed Martin Corporation, for the U.S. Department of Energy's National Nuclear Security Administration under contract DE-AC04-94AL85000.

ADATOM EMISSION FROM NANOPARTICLES: IMPLICATIONS FOR OSTWALD RIPENING

By

Tyne Richele Johns

B.S., Chemical Engineering

Doctor of Philosophy, Engineering

ABSTRACT

To achieve clean air in our cities, all modern means of ground transportation make use of catalytic converters. Precious metal-based catalysts such as Pt and Pd are currently used in catalytic converters. To achieve higher fuel efficiency, combustion can be carried out in excess air resulting in a reduction of greenhouse gas (GHG) emissions. Reduction of these emissions has emerged as a major challenge. Most of the pollutants are emitted within the first 30 seconds after starting an engine because the catalyst is cold. The development of catalysts which achieve high activity at low temperatures will improve fuel efficiency and therefore reduce the nation's dependence on foreign fossil fuels.

The supplies of precious metals are limited worldwide, but there is increasing demand for clean energy. Therefore, there is a need to develop more active catalysts that provide long-term stable performance at elevated temperatures with minimal use of precious metals such as platinum. A major problem is that catalysts lose activity during use. Pt particles sinter, leading to poor stability. There is universal agreement that addition of Pd improves the catalytic performance as well as the durability of the Pt catalysts; however, the mechanisms by which Pd improves the performance of Pt are less clear.

Conventional supported catalysts (Pt, Pd, and Pt-Pd) have been used to explore the microstructure of diesel oxidation catalysts (DOCs) in their working state (i.e. under oxidizing conditions). Model catalysts have been used to study the evolution of platinum and palladium nanoparticles. Both a statistical and a microscopic approach have been used to understand the ways in which Pd affects Pt. The catalytic activity and kinetics of various monometallic as well as bimetallic powder catalysts aged under different conditions has also

been studied. NO oxidation in the presence of NO, O_2, and NO_2 was the probe reaction used to distinguish between the differing activities of Pt/Al_2O_3 and $Pt\text{-}Pd/Al_2O_3$. The work described here focuses on important problems in the field of catalysis. A fundamental understanding of the role of palladium on both the catalytic activity and long-term performance of platinum catalysts has been gained.

TABLE OF CONTENTS

Chapter 1

Introduction and Review of the Literature

Platinum (Pt) and palladium (Pd) are two active metals used by the automotive industry in diesel oxidation catalysts (DOCs). [1-3] Platinum catalysts are very active, but previous reports in the literature indicate that platinum sinters and has poor durability under oxidizing conditions. [4-17] Two mechanisms of catalyst sintering are known. One is particle migration and coalescence, where particles migrate along the surface of the support and coalesce to form larger particles, and the second is Ostwald ripening. During Ostwald ripening particles emit atoms (or mobile species such as PtO_x) which migrate from smaller particles to form larger particles. The mobile species could travel along the surface of the support or through the vapor phase. In previous studies, it was shown that the sintering of platinum on an alumina support is primarily due to Ostwald ripening. [12, 13] Later in this work (Chapter 5), it will be shown that Pt nanoparticles sinter through Ostwald ripening on a SiO_2 model catalyst support.

Adams and Graham [4] showed that lean aging has a severe impact on NO_x trap performance. NO_x traps remove NO_x from diesel engine exhaust by combining three components: an oxidation catalyst such as Pt, an adsorbent, and a reduction catalyst. The adsorbers bind NO_x during lean (oxygen-rich) operation. Once the capacity is saturated, the NO_x is released and reduced to nitrogen during a period of rich engine operation. In the published work, the lean-aged NO_x trap reached only approximately 55% conversion whereas the rich-aged sample and degreened sample both achieved greater than 90% conversion. The deactivation was found to be irreversible due to platinum sintering. Graham *et al*. [8] also showed that platinum sinters under oxidizing conditions. Platinum particles which were around 6 nm in the as-prepared Pt/Al_2O_3 catalyst grew to about 11 nm after being aged under oxygen-rich hydrothermal conditions (5% O_2 and 10% H_2O in N_2) at 500ºC. The particles grew to sizes larger than 100 nm during aging at 900ºC.

There have been previous studies in the literature of Pd improving the durability of Pt catalysts [5, 6, 8-10, 16, 18] but it has been unclear how Pd enhances the durability and

performance of these catalysts: whether it is through a dispersion improvement, a lower rate of sintering on the bimetallic catalysts, or the presence of PdO in the catalyst. Previous work has suggested that in bimetallic Pt-Pd catalysts, any Pd not alloyed with Pt likely exists as PdO which could be a secondary active component. [1] However, it is well known that a Pd-only catalyst (which forms PdO under these conditions) is not as active as the Pt-only catalyst. Morlang *et al.* [10] reported that Pt-Pd catalysts supported on silica-doped alumina were more stable and had higher catalytic activity than the pure Pt catalysts. Based on their extended X-ray absorption fine structure (EXAFS) results, they concluded that Pd was present both as an oxide and in its metallic form on the bimetallic catalysts. They found an enrichment of Pt in the core of the particles and Pd in the shell. Persson *et al.* [19] also suggested that a metallic phase was maintained in an oxidizing atmosphere due to the alloying of Pt and Pd. Persson *et al.* [20] in a different account explained the morphology of the bimetallic Pt-Pd nanoparticles as being partially an alloy and partially rich in PdO. Ward *et al.* [21] used aberration-corrected scanning transmission electron microscopy (AC-STEM) to study the structure of fresh and aged Pt/SiO_2 and $Pt\text{-}Pd/\gamma\text{-}Al_2O_3$. They found that many of the aged bimetallic nanoparticles remained spherical and only about 30% became faceted core-shell particles with Pd segregated to the surface. About 60% of the particles did not show any segregation but instead were randomly alloyed. Significant PdO formation was not observed; this was thought to be the result of PdO reduction to Pd metal in CO/NO_x. Kaneeda *et al.* [9] found that the total NO oxidation activity was enhanced by the addition of Pd. Increasing the Pd fraction increased the dispersion but decreased the turn over frequency (TOF). They suggested that the Pt sintering, oxidation, and vaporization were inhibited by PdO on the surface. Kaya *et al.* [18] had a different account. They studied CO oxidation on different loadings of alumina-supported Pt-Pd catalysts and reported that as Pd content increased, so too did the nanoparticle diameter while the dispersion went down. They also suggested that Pd segregated to the surface, and their Monte Carlo simulations supported this. Ezekoye *et al.* [6] recently performed experiments that showed alumina-supported Pt-Pd catalysts sintered less than Pt/Al_2O_3 with little effect on the NO reaction rates. They saw no evidence for a layer of Pd or PdO. Particles less than 2.5 nm were primarily Pt-rich while those larger than 2.5 nm were Pd-rich.

These studies report average particle sizes as well as particle size distributions, but there is no agreement regarding the microstructure of the bimetallic Pt-Pd nanoparticles. It has been unclear how Pd modifies Pt in these catalysts, whether the Pd is present as a surface layer or as PdO, and the extent of alloying. Many of these studies were performed on alumina supports, but the automotive industry uses lanthanum-doped alumina supports. Recent studies show that addition of La to the alumina support modifies the reactivity of Pd.[22, 23] Therefore, an additional objective was to investigate how the presence of La modifies the stability of bimetallic catalysts.

This work has been divided into several areas, the first being the investigation of the microstructure of Pt-Pd nanoparticles on powder supports when aged under oxidizing conditions. For the first portion of this work, we have utilized scanning transmission electron microscopy (STEM) and energy dispersive X-ray spectroscopy (EDS) to determine compositional profiles within supported Pt-Pd particles. STEM is a local technique, whereas X-ray diffraction (XRD) and X-ray absorption spectroscopy (XAS) provide an average, which can be more conclusive. By using a combination of XRD and EXAFS, we obtained the average crystallite sizes. The sizes were verified using scanning electron microscopy (SEM). We have determined oxidation state via X-ray absorption near edge structure (XANES). These characterization techniques have helped us to explore the structure of bimetallic Pt-Pd catalysts as well as determine the oxidation state of Pd in the alloy after aging under oxidizing conditions.

Once we gained an insight into conventional powder catalysts, the work was expanded to model catalysts where it was possible to study the emission process. It is difficult to study the vapor phase processes in supported catalysts since atoms that are emitted can be adsorbed in other parts of the catalyst. When model catalysts are used, atoms emitted to the vapor phase are lost (swept away in the flowing gases) so it is possible to study the role of vapor phase processes. Pt sinters rapidly in air due to the formation of volatile PtO_2; [24] however, Pd shows very little sintering due to the low vapor pressure of PdO between 500°C and 800°C. As mentioned previously, the addition of Pd slows the rate of Pt sintering. The specific questions addressed in this portion of the work concerned the nature of the mobile species responsible for Ostwald ripening and the relative importance of the

vapor phase and surface diffusion processes. We also developed a technique using these model catalysts that provided a microscopic approach, where the behavior of individual nanoparticles could be tracked via TEM. Tracking individual nanoparticles allows the study of their mechanisms. Previously this had only been done using an environmental or in-situ TEM, where the pressures must be very low. Using our ex-situ approach, we were able to perform studies at atmospheric pressure so the volatility of Pt, Pd, and bimetallic Pt-Pd nanoparticles could be studied.

In the last phase of this work, the catalytic activity and kinetics of various monometallic and bimetallic catalysts aged under different conditions were examined. NO oxidation in the presence of NO, O_2, and NO_2 was the probe reaction used to distinguish between the differing activities of Pt/Al_2O_3 and $Pt\text{-}Pd/Al_2O_3$.

Chapter 2

Materials and Methods

Catalyst Preparation

Powder Catalysts for Microstructure Studies

Dispal (boehmite) from Sasol was calcined at 650°C for 10 hr to make γ-alumina, and the BET surface area was determined to be 153 m^2 g^{-1}. The BET surface area was measured on a Micromeritics Gemini 2360 instrument under liquid nitrogen at 77K. The La-alumina contains 4 wt. % La_2O_3 from W. R. Grace (MI-386) and has a BET surface area of 176 m^2g^{-1}. The Pt/La-Al_2O_3 and Pt/γ-Al_2O_3 catalysts were prepared by incipient wetness using an aqueous solution of chloroplatinic acid (8 wt. % H_2PtCl_6). The Pd/γ-Al_2O_3 and Pd/La-Al_2O_3 catalyst were prepared by incipient wetness using a Pd (II) nitrate solution (10 wt. % in 10 wt. % nitric acid). All monometallic samples had loadings of 0.8 wt. %. To synthesize the bimetallic samples, tetraamine Pd (II) nitrate (10 wt. % in water) was added to the 0.8 wt. % Pt catalysts by incipient wetness to make a 40:60 molar ratio of Pt to Pd. This led to a total metal loading of approximately 1.3 wt. %.

These six powder samples were first calcined in ambient air in a box furnace at 600°C for 4 hr. Then each sample was reduced in flowing 7% H_2/N_2 in a quartz tube furnace at 550°C for 2 hr. The samples were then aged in ambient air in a box furnace at 750°C for 10 hr. The catalysts in this state will be referred to as "aged" or "A." A portion of each catalyst was further reduced in 3.5% H_2/He at 250°C for 1 hr at the beamline for EXAFS experiments or reduced in 7% H_2/N_2 for 1 hr at 250°C in the laboratory for STEM analysis. These catalysts will be referred to as "aged + reduced" or "R." The BET surface area for the γ-Al_2O_3 support after these treatments was 139 m^2 g^{-1}, and the surface area for the La-Al_2O_3 was 172 m^2 g^{-1}.

Model Catalysts

Electron beam evaporation was used to synthesize all monometallic and bimetallic model catalysts. The high purity metals (99.999%) of both platinum and palladium used to fabricate the model catalyst samples were purchased from Materion Corporation. The metals were deposited directly onto the 2 mm x 2 mm SiO_2 TEM grid surface using a 10kV Temescal electron beam evaporator. This high vacuum cryo-pumped system was pumped to a base pressure of 1 x 10^{-7} torr prior to deposition. The film thickness was controlled by a quartz crystal microbalance (QCM), while the deposition rate was controlled to 0.03 Å/s. This system as configured is capable of controlling the film thickness to 0.1 Å. These noble metals are non-wetting on oxide surfaces so a continuous film is not formed during deposition at these very low loadings. All films were deposited to a value equivalent to 5 Å.

The TEM grids have a 200 µm x 200 µm silicon nitride membrane window with a thickness of 15 nm. [25] The top and bottom 3 nm have been formed into a surface oxide layer through calcination in air at 750°C for 24 hours. These silicon-based TEM grids allow for high temperature aging.

The samples were reduced for 10 minutes in flowing 7% H_2/N_2 (140 sccm) in a SabreTube^{TM} furnace created by Absolute Nano. The furnace allows for a 100°C/s heating rate over a 1 cm wide substrate. Temperatures up to 1000°C are possible with the SabreTube^{TM}. The short two-minute aging treatments were performed in the SabreTube in flowing air at 140 sccm. The 1.5 hour aging treatments were done in a quartz tube furnace in flowing air at 100 sccm due to limitations on that flow meter. The quartz tubes have an inner diameter of 2 cm. The ramp rate of the furnace was 20°C/min, and the temperature was held for 1.5 hours and then decreased to room temperature in the flowing air. The model catalysts used in the detailed mechanistic studies discussed in Chapter 5 were reduced in flowing 6% H_2/Ar and were aged in 21% O_2/Ar to simulate air. Both treatments were done in the SabreTube^{TM}.

Powder Catalysts for NO Oxidation

Monometallic Pt/Al_2O_3 and Pd/Al_2O_3 catalysts were synthesized by incipient wetness. Chloroplatinic acid and palladium nitrate were the precursors used. They were introduced to

a lanthanum-stabilized alumina support from Rhodia Catalysts (MI-386SP) after being diluted with water. These slurries were dried overnight in a fume hood. The next day they were crushed into fine powders using a mortar and pestle and dried at 135°C for 3 to 4 hours. Once the powders were dried, they were calcined at 500°C for 1 hr in ambient air.

The monometallic Pt/Al_2O_3 sample was milled with water and reagent grade acetic acid from JT Baker. The bimetallic sample was prepared by physically mixing the two monometallic catalysts and milling them with water and the reagent grade acetic acid. The monometallic and bimetallic samples were dried at 90°C to 100°C. According to inductively coupled plasma atomic emission spectroscopy (ICP-AES) the bimetallic sample contains 0.61 wt% Pd and 0.62 wt% Pt while the pure Pt sample contains 0.56 wt% Pt.

Catalyst Characterization

X-ray Diffraction (XRD)

X-ray diffraction measurements were performed on a Rigaku SmartLab diffractometer using Cu K_α radiation. The powders were lightly pressed into a cavity in a plastic sample holder. The samples were run using Bragg Brentano geometry using a D/tex position-sensitive detector and a Ni K_β filter. Data was acquired with a rate of 16°/min from 15° to 130°. A step size of 0.02 was used. Diffraction peak broadening due to instrumental effects was accounted for using NIST standard LaB_6. All analysis was done using GSAS software.

Transmission Electron Microscopy (TEM), Scanning Transmission Electron Microscopy (STEM), and Energy Dispersive X-ray Spectroscopy (EDS)

A JEOL 2010F 200kV FASTEM FEG (field emission gun) TEM/STEM was used to acquire STEM images. It has a GATAN GIF 2000 Energy Filter, JEOL bright and dark field STEM detectors, GATAN bright and dark field STEM detectors, and an Oxford Instruments ISIS/INCA EDS system with an Oxford Pentafet Ultrathin Window Detector (UTW). This microscope has a point-to-point resolution of 0.194 nm and a minimum spot size in STEM mode of 0.14 nm. However, for compositional analysis by EDS, we used a probe size of 1.0 nm to obtain adequate counting statistics. For high resolution compositional mapping, we

also used a JEOL JEM 2100F AC (aberration-corrected STEM). The nominal point resolution and ultimate probe size for this instrument was similar to that of the JEOL 2010F, but the aberration corrector provides a much higher probe current for EDS analysis. The 2100F has a TEM point resolution of 2.3Å and a lattice resolution of 1Å. In STEM mode, a resolution of 1.4Å is possible. The microscope is configured for both traditional TEM as well as STEM. Some images for this work were taken using a high angle annular dark field (HAADF) detector. The electron source on this microscope is a field emission gun, and the microscope is equipped with a STEM mode spherical aberration corrector (Cs).

High resolution TEM (HR-TEM) images were taken using the FEI Titan 80-300 environmental transmission electron microscope (E-TEM) at the Center for Functional Nanomaterials at Brookhaven National Laboratory. This microscope is equipped with an objective-lens aberration corrector and has a spatial resolution of 0.08 nm in HR phase contrast mode.

An advanced FEI Technai 20, type Sphera TEM was used at Eindhoven University of Technology (TU/e) to obtain TEM images of samples aged in the SabreTube furnace for the detailed mechanistic studies. This TEM operates with a 200 kV LaB_6 filament and a bottom-mounted 1024 x 1024 Gatan msc 794^{TM} CCD camera. The microscope is equipped with an EDAX unit for EDS elemental analysis.

Gatan Digital Micrograph was used for all image processing, and INCA was used for the analysis of all EDS data. Diameters of nanoparticles were determined by manual measurement within the Digital Micrograph software. EDS was used to obtain compositions as well as gather information on loss of metal. Pt and Pd L lines were used in the EDS analysis. To determine the loss of metal on each model catalyst sample, either the ratios of the metal to silicon or the absolute counts of the metal were compared before and after aging in air at the specific temperature. Each time EDS was performed on a model catalyst sample, it was done in at least ten areas around the sample. The electron transparent region of each sample was a 200μm x 200μm square. One area in each of the four corners and one area along each of the four edges were analyzed. Then, at least two random areas in the center of the square were analyzed. Two different techniques have been used to quantify emission on these model catalysts. Here we discuss how to determine loss of Pt, but the same can be

applied for Pd or the bimetallic model catalysts. One technique compares the ratio of the atomic percentage of platinum to the atomic percentage of silicon before aging and after aging. Using ratios factors out the efficiencies and inefficiencies associated with the microscope and the EDS detector. The SiO_2 membrane is thought to remain constant during the aging treatments. If, however, a volatile silica species (SiO_x) caused the loss of Si, using the ratio technique would not provide accurate loss of Pt. For this reason, another technique was employed comparing the absolute counts of Pt before and after aging. To accurately use this method, a set of parameters had to be constant each time a sample was analyzed in the microscope. Every time a sample had EDS performed on it, the sample holder had to be tilted to the same degree, and the magnification, spot size, apertures, process time, and live time had to be kept the same. The same area also had to be illuminated on the phosphor screen. There was some fluctuation of the current density so this was noted every time EDS was done so that the Pt counts could be normalized. The ratio technique and the method of using absolute counts provided very similar emission results. They were always within the experimental error of EDS (±5%).

Scanning Electron Microscopy (SEM)

The scanning electron microscope (SEM) used for this work was a Hitachi S-5200. This SEM is capable of a resolution of 1.7 nm at 1 kV and 0.5 nm at 30 kV. It was operated at 2kV to image the samples in backscattered mode as well as in the secondary electron mode. The catalyst sample was prepared by pressing the powder onto double-sided carbon tape which was attached to the sample holder.

X-ray Absorption Spectroscopy (XAS)

Pd K-edge and Pt L3-edge X-ray absorption measurements were conducted at room temperature on the insertion device beamline 10-ID-B at the Advanced Photon Source (APS) at Argonne National Laboratory using transmission mode. The amount of catalyst loaded into the sample holder was selected to obtain an edge step of 0.3 to 1.0 for the given experiment. Each aged catalyst was ground to a fine, uniform consistency and compressed into a stainless steel sample holder (die) with 6 cylindrical openings for up to 6 samples. The die was inserted into a quartz tube sample cell which had an inner diameter of 3/4” and X-ray

transparent end caps made of Kapton. The cell allowed for flow of gases, and it was mounted on a movable sample stage which allowed for sample alignment in the beam path. After XAS was completed on the aged samples, the sample cell was taken off-line to perform additional sample treatments. A flow of 50 cm^3/min of He was first delivered to the cell for 5 minutes to purge O_2. Then a reducing environment of 3.5% H_2/He was provided for 1 hour at 250°C, followed by a purge of He for 5 minutes at temperature. This was done to prevent formation of Pd hydrides during the cool-down. Then, the cell was removed from the furnace where it cooled to room temperature under flowing He. Once it reached room temperature, the sample cell was disconnected from the gas feed and sealed with He inside. X-ray absorption measurements were then performed on the aged plus reduced samples.

Linear combination fitting (LCF) of the data to both metallic and oxide standards was performed to determine the oxidation state of each metal in the near-edge portion of the spectra (XANES). Analysis of the extended portion of the spectra (EXAFS) provided bond distances and coordination of each metal, which indicated the extent of Pt-Pd alloying and particle sizes (nanoparticles versus bulk material). ATOMS [26] and FEFF6 [27] were the software packages used to generate *ab initio* photoelectron scattering models of structures containing Pt, Pd, and O. Face centered cubic (FCC) Pt and Pd paths were created using data from Kittel. [28] Data from Waser *et al.* [29] was used to generate a PdO structure (P42/mmc; antifluorite derivative) with an origin shift of (0,1/2,0) to comply with the positions listed in the International Tables for Crystallography [30] with Pd in site 2c and O in site 2f. To account for alloying of Pd and Pt, substitution of Pd sites with Pt (and vice versa) was used. Then a least squares fitting algorithm was used to fit the models to the experimental EXAFS spectra. This allowed the determination of bond distance as well as coordination number for Pt and Pd absorbers.

Inductively Coupled Plasma (ICP) Spectroscopy

Inductively Coupled Plasma (ICP) spectroscopy was the technique used to obtain elemental analysis of the monometallic and bimetallic catalyst samples prepared for NO oxidation. A Varian Vista Pro system which utilizes a radial view of the plasma was used. Pt and Pd concentrations were measured in the monometallic and bimetallic samples. Pt and Pd were leached from the substrate and the resulting solution was analyzed by ICP-AES.

99.999% pure materials were used for the calibration solutions. The detection limit was 5 ppm. Pt and Pd weight percentages were found by averaging three atomic emission lines.

Chapter 3

Microstructure of Bimetallic Pt-Pd Catalysts Under Oxidizing Conditions

This chapter is based on an extended abstract to be published in Microscopy and Microanalysis, and the complete chapter has been accepted for publication in ChemCatChem. This chapter is the pre-peer reviewed version of the following article. It is available online at the following link. http://dx.doi.org/10.1002/cctc.201300181

Johns, T.R., Gaudet, J.R., Peterson, E.J., Miller, J.T., Stach, E.A., Kim, C.H., Balogh, M.P., Datye, A.K., *Microstructure of Bimetallic Pt-Pd Catalysts Under Oxidizing Conditions*, ChemCatChem, 2013, DOI 10.1002/cctc.201300181.

The extended abstract to be published in Microscopy and Microanalysis is shown in the Appendix.

Abstract

Diesel oxidation catalysts (DOCs), which reduce harmful carbon monoxide (CO), nitrogen oxide (NO), and hydrocarbon (HC) emissions in engine exhaust, typically utilize Pt and Pd as the active phase. There is universal agreement that addition of Pd improves the catalytic performance as well as the durability of the Pt catalysts. However, the mechanisms by which Pd improves the performance of Pt are less clear. Since these catalysts operate under oxidizing conditions, it is important to understand these catalysts in their working state. Here we report the microstructure of Pt-Pd catalysts aged in air at 750°C. After 10 hours of aging, EXAFS and XANES show that the Pt is fully reduced but almost 30% of the Pd is present as an oxide. HR-TEM images show no evidence for a surface oxide on the metallic Pt-Pd particles. Instead the PdO is present as a separate phase dispersed on the alumina support. Within the metallic particles, Pt and Pd are uniformly distributed, and we do not see evidence for core-shell structures. The improved catalytic performance is therefore likely associated with the co-existence of *metallic* Pt and Pd on the catalyst surface.

Introduction

Platinum (Pt) and palladium (Pd) constitute the active phase in diesel oxidation catalysts (DOCs) that are used by the automotive industry. [1-3] While the Pd-only catalyst shows poor performance in the NO oxidation reaction, the addition of Pd to Pt has no detrimental effect on the catalytic activity for NO oxidation. [6, 8, 9] Instead, Pd addition leads to improved durability of the catalyst. On the other hand, there is definite improvement in catalytic performance for hydrocarbon oxidation [1, 3, 10, 20, 31-33] and for CO oxidation [1, 3, 10] when Pd is added to Pt. For these reasons Pd is included in the formulation of commercial catalysts for diesel oxidation. [1-3] The mechanisms by which Pd improves the catalytic performance of Pt are not fully understood. To investigate the beneficial effect of added Pd, a detailed microstructural analysis was performed by Graham *et al*. [8] on Pt and Pt-Pd/Al_2O_3. They found that Pt particles which were around 6 nm in the as-prepared Pt/Al_2O_3 catalyst grew to about 11 nm after being aged under oxygen-rich hydrothermal conditions (5% O_2 and 10% H_2O in N_2) at 500ºC. However, after 750°C aging, which is the more commonly used aging temperature, they found that the Pt particle size (via X-ray diffraction (XRD)) was 18 nm while that of the Pt-Pd(50:50) catalyst was 15 nm. The improvement in dispersion measured by CO chemisorption was consistent with these particle sizes, with dispersion changing from 0.025 on the Pt-only catalyst to 0.030 on the bimetallic. This would amount to a 20% improvement in dispersion, caused by the presence of the Pd but would not explain the improved catalytic performance for oxidation of hydrocarbons. A key difference is that during hydrocarbon oxidation the catalyst is operated in a net oxidizing environment; hence, it is important to investigate the nature of the Pt-Pd catalyst closer to its true working conditions.

A recent study of vehicle-aged Pt-Pd catalysts was reported by Ward *et al*. [21] who used aberration-corrected scanning transmission electron microscopy (AC-STEM) to study the structure of fresh and road-aged Pt/SiO_2 and Pt-Pd/γ-Al_2O_3. They found that the majority of the aged bimetallic nanoparticles remained spherical and did not show any segregation but instead were randomly alloyed. Only about 30% became faceted core-shell particles with Pd segregation to the surface. Significant PdO formation was not observed; this was thought to be the result of PdO reduction to Pd metal in the CO/NO_x atmosphere. In comparison to the

Pt-only sample, the addition of Pd did not change the average particle size, but the authors did find a narrower particle size distribution on the bimetallic sample. This finding is similar to that reported by other groups. [1, 8] It is well known that platinum sinters and has poor durability under oxidizing conditions. [4-17] Adams and Graham [4] showed that lean aging has a severe impact on NO_x trap performance because Pt sinters under oxidizing conditions. [8] What is surprising is that Pt particles grew to sizes larger than 100 nm during aging at 900ºC, while the Pd containing catalysts did not show such large particles. A similar finding was reported by Kallinen *et al.*[1] who found Pt particles as large as 1 micron after aging at 800°C. These research groups suggested that a plausible role of Pd in these catalysts could be the formation of a surface oxide of Pd on the metal particles which would reduce the emission of volatile Pt oxides. The AC-TEM images of Ward *et al.* [21] and Ezekoye *et al.* [6] do not show any such surface oxide. However, a more sensitive technique to find small amounts of Pd oxide is extended X-ray absorption fine structure (EXAFS), since it can detect a crystalline oxide as well as a dispersed oxide. It is therefore necessary to study the catalyst in its oxidized state, while most of the studies described above only study the microstructure of the Pt-Pd catalysts in their reduced state. [6, 8, 9]

An EXAFS study of Pt-Pd catalysts was reported by Morlang *et al.* [10] They found that their Pt-Pd catalysts supported on silica-doped alumina were more stable and had higher catalytic activity than the pure Pt catalysts. Based on their EXAFS results, they concluded that Pd was present both as an oxide and in its metallic form on the aged bimetallic catalysts. However, they could not conclusively identify the location of the oxide phase. It is well known that a Pd-only catalyst is fully oxidized in the calcined and thermally aged state and can be fully transformed to its metallic state under reducing conditions. There is, however, limited understanding of the location of Pd oxides on the bimetallic catalyst. Morlang *et al.* [10] proposed two different models of where the PdO could be present in the thermally aged bimetallic catalyst. A PdO shell could surround the Pt-Pd core which would suppress Pt diffusion and stabilize the catalyst; however, their high resolution transmission electron microscopy (HR-TEM) images did not show a PdO phase on the surface of the metallic particles, and neither was such an oxide seen by Ezekoye *et al*. [6] or Ward *et al*. [21] Alternatively they proposed that PdO must be present on the surface of the bimetallic nanoparticles as nanocrystallites or on the support as isolated PdO crystals. However, they

did not have any definitive evidence for such a structure based on the limited resolution of the TEM available for their work. A more recent study of alumina-supported bimetallic Pd-Pt catalysts for methane combustion was reported by Persson *et al.* [20, 32] They determined that the PdO present was in close proximity with the alloy.

As can be seen from this review of the literature, characterization of these catalysts under oxidizing conditions is a significant challenge. Techniques such as XRD and TEM work best with reduced catalysts, since the metallic phase is more ordered and provides better contrast making it easier to characterize, while the oxide phase is often dispersed and disordered. These previous studies raise questions about the nature of the Pd oxide in these working catalysts which might play a crucial role in the enhanced catalytic activity as well as the durability. X-ray absorption spectroscopy (XAS) is the technique of choice to determine the nature of dispersed oxide species, and especially useful to determine the oxidation state of Pt and Pd. But since XAS provides information averaged over the entire sample, we need to complement it with a technique having a high spatial resolution, such as aberration corrected TEM. Furthermore, these Pt-Pd catalysts after aging have large particles which are beyond the ability of TEM or XAS to characterize. We need complementary methods such as scanning electron microscopy (SEM) and XRD to obtain information over the larger length scales. In this work, we used a combination of all of these techniques to develop a comprehensive picture of working Pt-Pd catalysts exposed to oxidizing conditions at 750°C in air. These are the conditions most commonly used for the aging of Pt-Pd diesel oxidation catalysts. [1, 3, 8-10] In this work we studied 0.8 wt. % monometallic Pt and Pd catalysts and a 1.3 wt. % Pt-Pd catalyst (40:60 atomic ratio) on two supports: γ-alumina and La-stabilized alumina, the latter being included because it is the support most commonly used for automotive catalysts. The results provide insights into the nature of the phases present when the catalysts are operated under oxidizing conditions.

Results and Discussion

Six catalysts were prepared: Pt/La-Al_2O_3, Pt/γ-Al_2O_3, Pd/La-Al_2O_3, Pd/γ-Al_2O_3, Pt-Pd/La-Al_2O_3, and Pt-Pd/γ-Al_2O_3. The catalysts were aged at 750°C in air for 10 hours. The catalysts in this state are referred to as aged or "A." A portion of each catalyst was then

reduced at 250°C for 1 hour. The catalysts in this state are referred to as aged plus reduced or "R."

From XRD, the crystal structure and size of small crystalline domains can be obtained, and the lattice constant helps to determine the composition of bimetallic samples. Figure 1 shows XRD patterns of 750°C air-aged La-Al_2O_3 supported Pt-Pd, Pt, and Pd catalysts and the support La-Al_2O_3. These patterns represent the raw data obtained from the diffractometer without any background subtraction. To allow comparison between the three

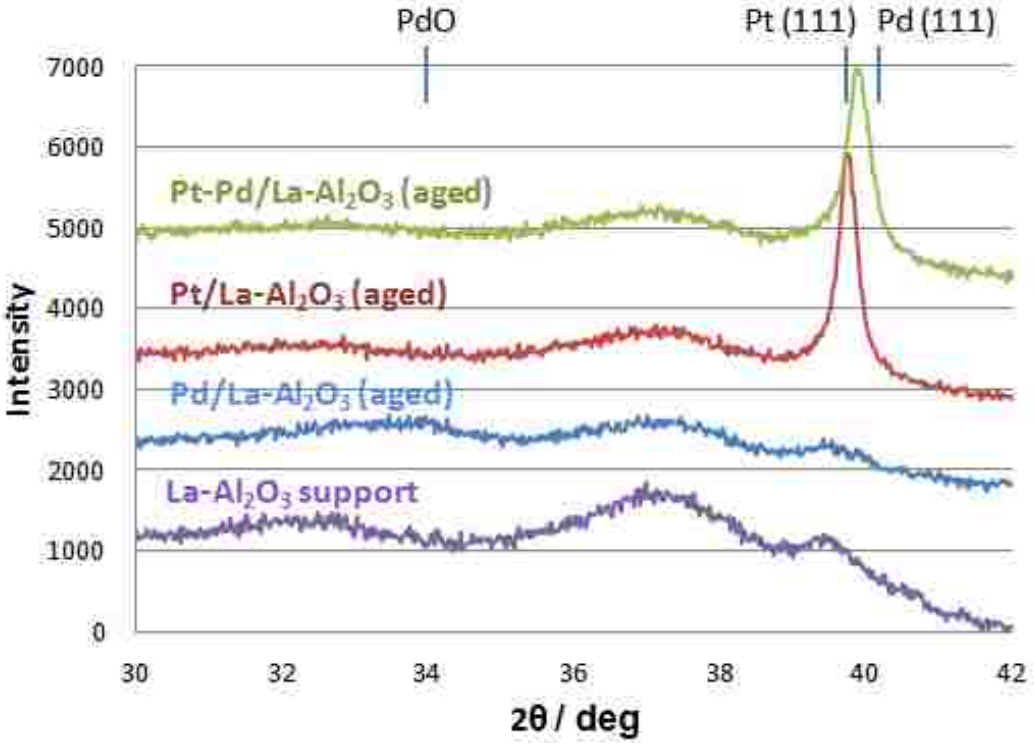

Figure 1. XRD patterns of La-Al_2O_3 support and 750°C air-aged Pt-Pd/La-Al_2O_3, Pt/La-Al_2O_3, and Pd/La-Al_2O_3. These patterns represent the raw data obtained from the diffractometer, without any background subtraction. To allow comparison between the three catalysts, the data for each catalyst was offset vertically.

catalysts, the data for each catalyst were offset vertically. The bimetallic and the Pt samples show a peak at the (111) position. The (111) reflection occurs at a 2θ of 39.7° for Pt and 39.9° for Pt-Pd. The bimetallic peak is shifted to the right because the lattice constant of Pt-Pd is smaller than that of Pt, according to Vegard's Law. It is noteworthy that these air aged samples show metallic Pt but no other oxide phases. The Pd-only catalyst shows a very broad and weak reflection corresponding to PdO and is slightly larger on the alumina

support. This suggests that Pd is very well dispersed on the La-alumina support, and even after 10 hours of aging the peaks are so broad that we cannot quantify them via XRD. SEM and EXAFS results, shown later, confirm this observation. The results for the alumina support are similar, and the XRD patterns for all of these samples are presented in figures 2-4. Table 1 gives the average diameter of the Pt and Pt-Pd crystallites in the aged and aged plus reduced states on both supports. The Pt particle size is considerably larger than that of Pd since Pt is known to sinter under oxidizing conditions. [8] It is also noteworthy that the Pt particle size is much greater on the La-modified Al_2O_3 support than γ-Al_2O_3, suggesting that the presence of La is not beneficial for the dispersion of Pt. Reducing the sample in H_2 does not change any of the observed crystallite sizes suggesting that the Pt was already fully reduced. We also do not see any metallic Pd peaks after reduction suggesting that any metal present in dispersed form is too small in size to be detected by XRD.

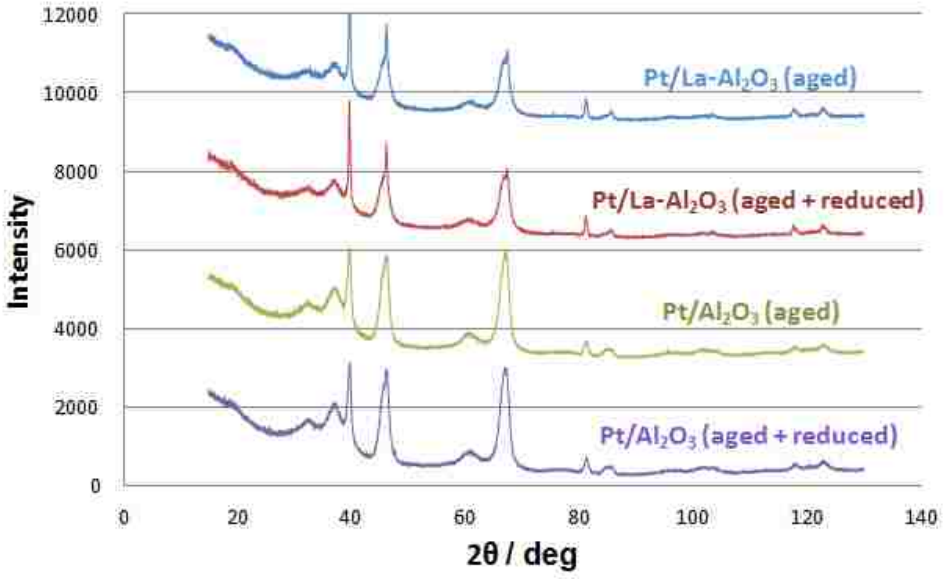

Figure 2. XRD patterns of aged and aged plus reduced Pt catalysts before background subtraction. To allow comparison between the catalysts, the data for each catalyst was vertically offset.

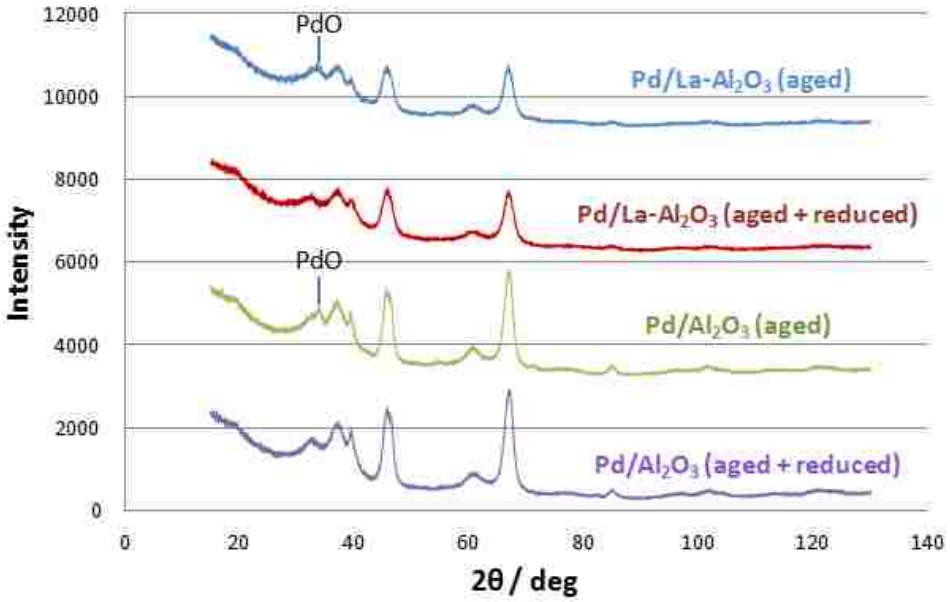

Figure 3. XRD patterns of aged and aged plus reduced Pd catalysts before background subtraction. To allow comparison between the catalysts, the data for each catalyst was vertically offset.

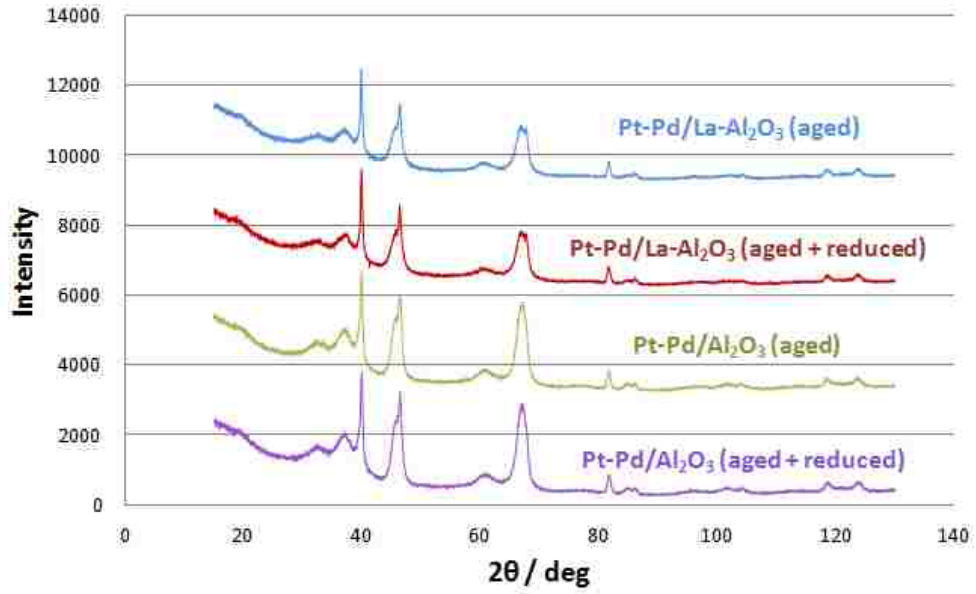

Figure 4. XRD patterns of aged and aged plus reduced Pt-Pd catalysts before background subtraction. To allow comparison between the catalysts, the data for each catalyst was vertically offset.

Table 1. Nanoparticle sizes determined by XRD.

	Pt/Al_2O_3-A	Pt/Al_2O_3-R	$Pt/La\text{-}Al_2O_3$-A	$Pt/La\text{-}Al_2O_3$-R
Size (nm)	18.4 ± 0.4	19.6 ± 0.5	34.5 ± 0.9	34 ± 1
	$Pt\text{-}Pd/Al_2O_3$-A	$Pt\text{-}Pd/Al_2O_3$-R	$Pt\text{-}Pd/La\text{-}Al_2O_3$-A	$Pt\text{-}Pd/La\text{-}Al_2O_3$-R
Size (nm)	25.3 ± 0.6	22.9 ± 0.5	24.9 ± 0.7	25.8 ± 0.6
Composition	32 at. % Pd, 68 at. % Pt	32 at. % Pd, 68 at. % Pt	32 at. % Pd, 68 at. % Pt	32 at. % Pd, 68 at. % Pt

The size of the bimetallic nanoparticles was similar on both supports at approximately 25 nm as shown in Table 1. The size of the bimetallic nanoparticles is larger than the size of the Pt nanoparticles on the γ-Al_2O_3 support suggesting that the addition of Pd did not help prevent sintering. The average size of the La-Al_2O_3 supported Pt particles, however, is much larger than that of the Pt-Pd/La-Al_2O_3 nanoparticles. The composition of the bimetallic nanoparticles was determined based on the lattice constant and its deviation from ideality in a Pt-Pd alloy. [34] In our analysis, the lattice constant used for Pd was 3.890Å. Using Rietveld refinement in GSAS, Pt was refined to be 3.923Å, and the bimetallic was refined to have a lattice constant of 3.909Å. The inferred composition of the bimetallic samples, based on this lattice constant, is 32 at. % Pd and 68 at. % Pt. The reason this composition is different from the overall composition of the catalyst is that XRD only takes into account the large metallic nanoparticles. A similar discrepancy was observed by Ezekoye *et al*. [6] who found that the metallic particles were Pt-rich. We show later that the composition of the large bimetallic particles by energy dispersive X-ray spectroscopy (EDS) analysis agrees with XRD because a dispersed Pd phase accounts for the balance of the Pd. The dispersed Pd species do not show up in XRD.

The local molecular structure of a specific element in a sample can be inferred through EXAFS. X-ray absorption near edge structure (XANES) provides information on coordination geometry and valence state. When aged in air the Pd-only samples are fully oxidized, while the bimetallic samples show that a portion of the Pd (20-30%) is present as an oxide (Figure 5 (a)). Table 2 summarizes the extent of oxidation in these samples.

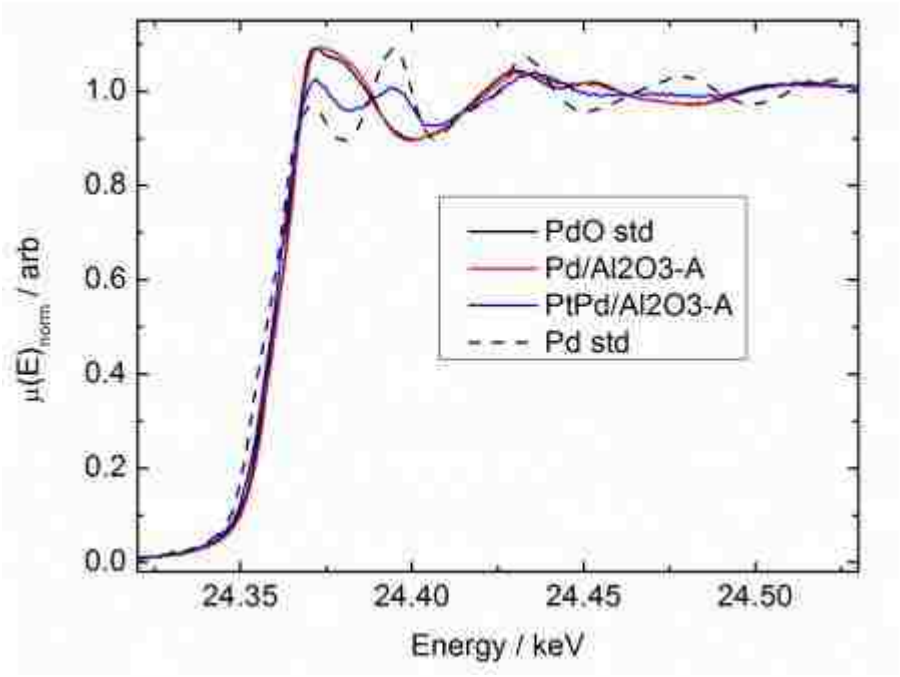

Figure 5(a). XANES at the Pd edge showing that the Pd-only catalysts are fully oxidized while the bimetallics show Pd to be partly oxidized, even after aging at 750°C in air for 10 hours.

XANES analysis was performed on catalysts on both supports, but we have chosen to show only the alumina-supported catalysts in some of the XANES figures for clarity, followed by plots with the remaining data. There was very little difference between the two supports. When these samples were reduced in H_2 at 250°C for 1 hour, the Pd was fully reduced (Figure 5 (b)). In contrast, the Pt catalysts aged in air were already fully reduced (Figure 6 (a)). Further reduction in H_2 did not change either the XANES (Figure 6 (b)) or XRD (Figure 7) results.

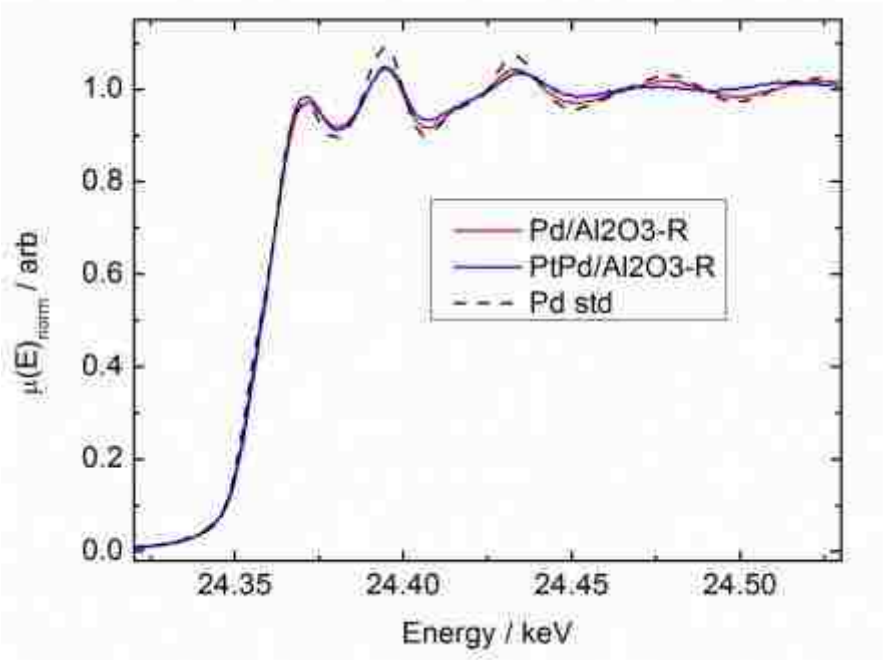

Figure 5(b). XANES at the Pd edge after reduction in H_2, showing that the Pd is almost fully reduced in all catalysts.

Table 2. Oxide Content of Catalysts Determined via XANES.

Percent Pd Oxide				Percent Pt Oxide		
	Aged	Aged + Reduced			Aged	Aged + Reduced
Pd/Al_2O_3	100%	0%		Pt/Al_2O_3	0%	0%
$Pd/La\text{-}Al_2O_3$	100%	0%		$Pt/La\text{-}Al_2O_3$	0%	0%
$Pt\text{-}Pd/Al_2O_3$	30%	0%		$Pt\text{-}Pd/Al_2O_3$	0%	0%
$Pt\text{-}Pd/La\text{-}Al_2O_3$	20%	0%		$Pt\text{-}Pd/La\text{-}Al_2O_3$	0%	0%

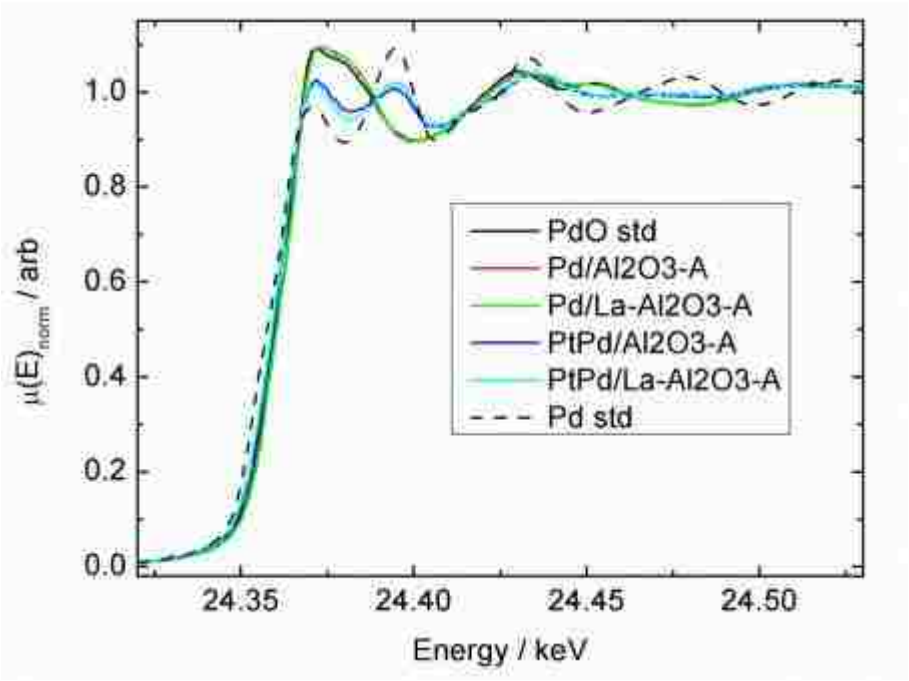

Figure 5(c). XANES at the Pd edge showing that the Pd-only catalysts are fully oxidized while the bimetallics show Pd to be partly oxidized, even after aging at 750°C in air for 10 hours. This plot shows both supports.

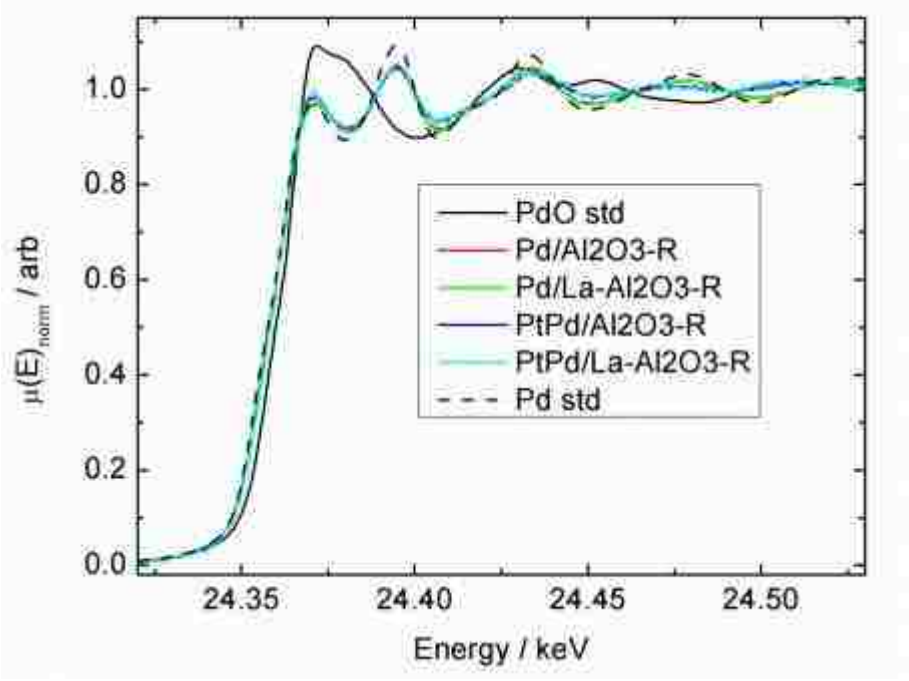

Figure 5(d). XANES at the Pd edge after reduction in H_2, showing that the Pd is almost fully reduced in all catalysts. This plot shows both supports.

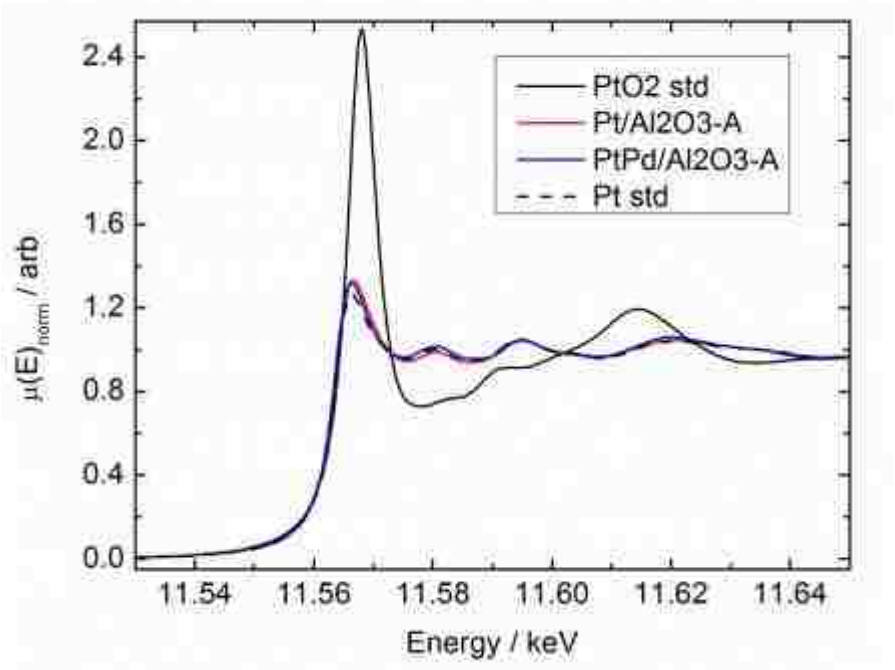

Figure 6(a). XANES at the Pt edge showing that Pt is almost fully reduced even after aging for 10 hours at 750°C in air.

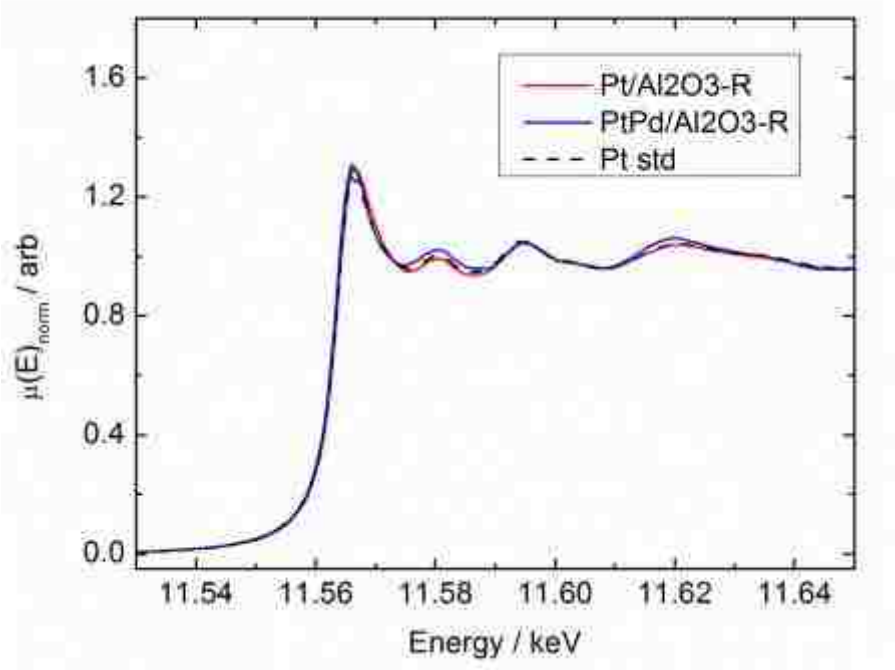

Figure 6(b). XANES at the Pt edge after H_2 reduction shows very little change compared to the aged sample, confirming that Pt stays metallic when treated in air at 750°C.

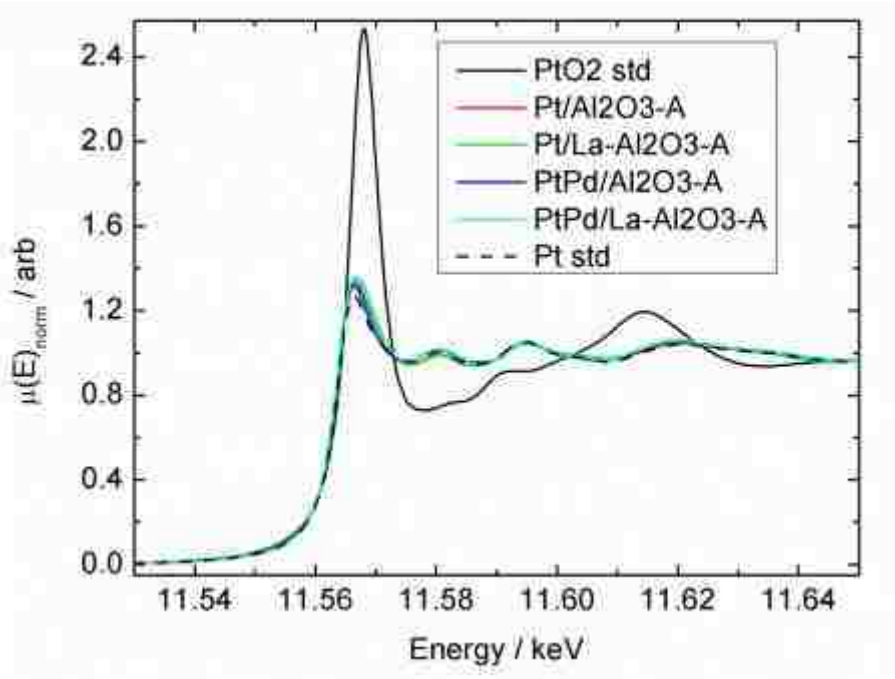

Figure 6(c). XANES at the Pt edge showing that Pt is almost fully reduced even after aging for 10 hours at 750°C in air. This plot shows both supports.

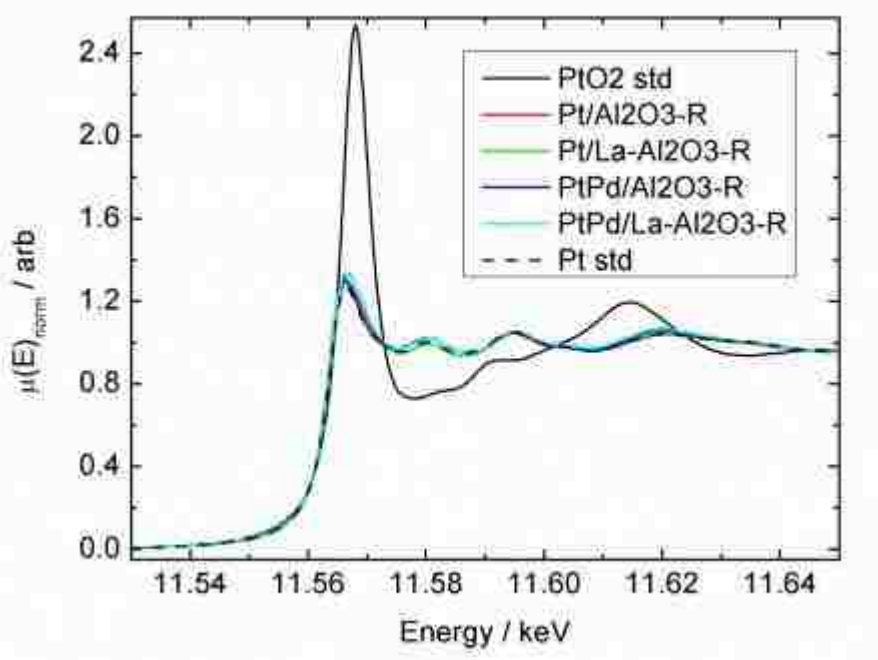

Figure 6(d). XANES at the Pt edge after H_2 reduction shows very little change compared to the aged samples, confirming that Pt stays metallic when treated in air at 750°C. This plot shows both supports.

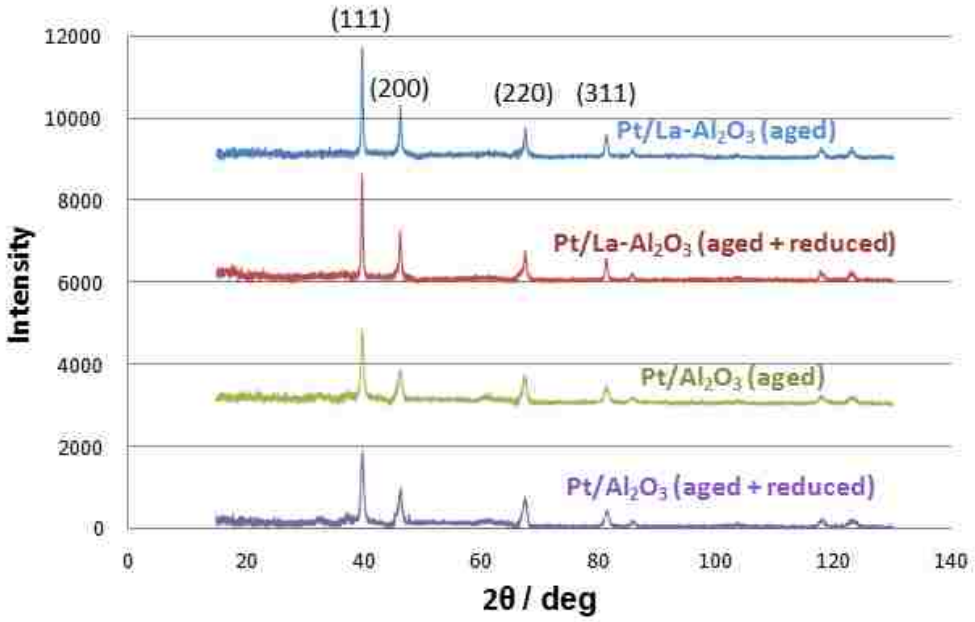

Figure 7. XRD patterns of aged and aged plus reduced Pt catalysts after background subtraction. To allow comparison between the catalysts, the data for each catalyst was vertically offset by 3000 counts.

Figures 8(a) and (b) show the EXAFS Pd K edge results for the aged samples and aged plus reduced samples, respectively. EXAFS analysis was performed on all catalysts supported on both alumina and La-alumina, but both supports showed similar spectra. We are showing the EXAFS data for only the La-alumina supported catalysts in 8(a), 8(b), 9(a), and 9(b) to make the figures easy to interpret. The remaining EXAFS data for all supports can be seen in Figures 8(c), 8(d), 9(c), and 9(d). The monometallic Pd samples are both completely oxidized in the aged catalyst. The second shell Pd-O-Pd shows reduced intensity at 3Å indicating very small nanoparticles of oxide. The bimetallic spectra show a coexistence of PdO and the Pt-Pd alloy in the aged sample. After reduction in H_2, the Pd-only samples become metallic on both supports. Coordination numbers are averaged over bulk and surface atoms, where a bulk coordination number is equal to 12. For large particles, the surface to volume ratio is negligible, and the average is 12. The coordination numbers of approximately 10, shown in Table 3, indicate small particles. This makes sense because XRD did not show any Pd peaks, and in low loading catalysts the peak broadening makes it difficult to detect a highly dispersed phase via XRD. Table 3 gives the first shell coordination numbers for the aged and aged plus reduced monometallic samples used in this

study. The error is 10% of the coordination number *N*. For the Pd samples, the coordination number Pd_Pd represents the average number of nearest Pd neighbors, and Pd_O represents the average number of nearest oxygen neighbors surrounding each Pd atom. Using a similar approach, coordination numbers are derived from the absorption at the Pt edge indicating the neighbors surrounding each Pt atom (Pt_Pt and Pt_O). It is clear from the coordination numbers in the table that the monometallic Pd samples have a higher dispersion than the Pt samples. The Pt coordination of 12 in the monometallic samples indicates large metallic particles, which is consistent with the large peaks seen via XRD and the absence of an XRD peak for the monometallic Pd sample.

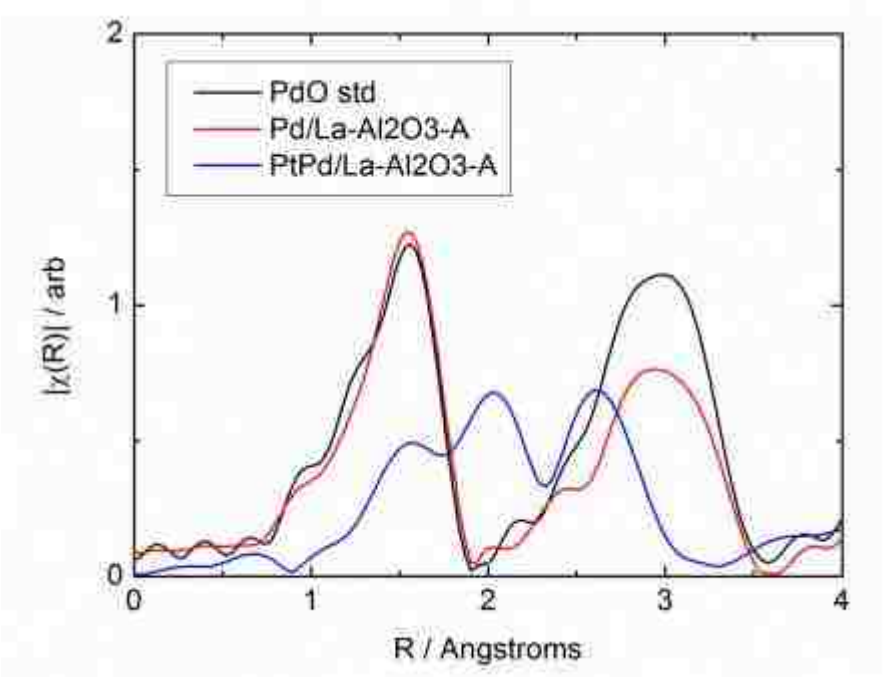

Figure 8(a). Fourier Transform EXAFS Pd K edge results for the aged samples. The monometallic samples show peaks corresponding to Pd-O and a second shell Pd-Pd. The lower amplitude for the second shell is consistent with small, dispersed, PdO on the surface of the catalyst. In contrast, the bimetallic sample shows peaks consistent with Pt neighbors as well as Pd neighbors for metallic Pd and only the first shell oxide, suggesting that the oxide is now a dispersed phase.

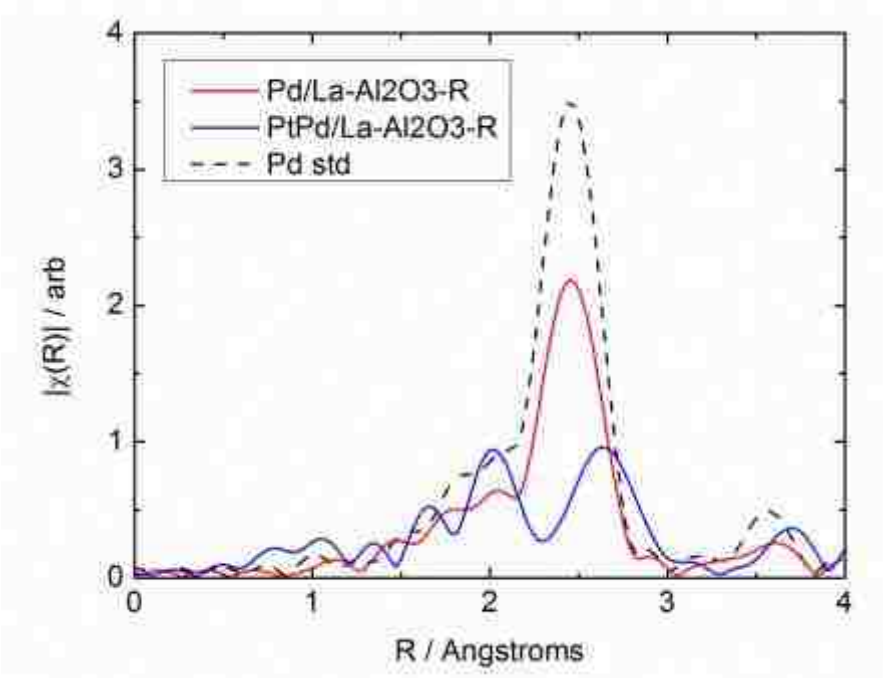

Figure 8(b). EXAFS Pd K edge results for the aged + reduced samples. The monometallic samples show a Pd-Pd peak with no higher shells, consistent with small metal particles (which cannot be seen via XRD). The bimetallics show co-existence of the alloy and some dispersed Pd on the catalyst, as confirmed also by STEM-EDS.

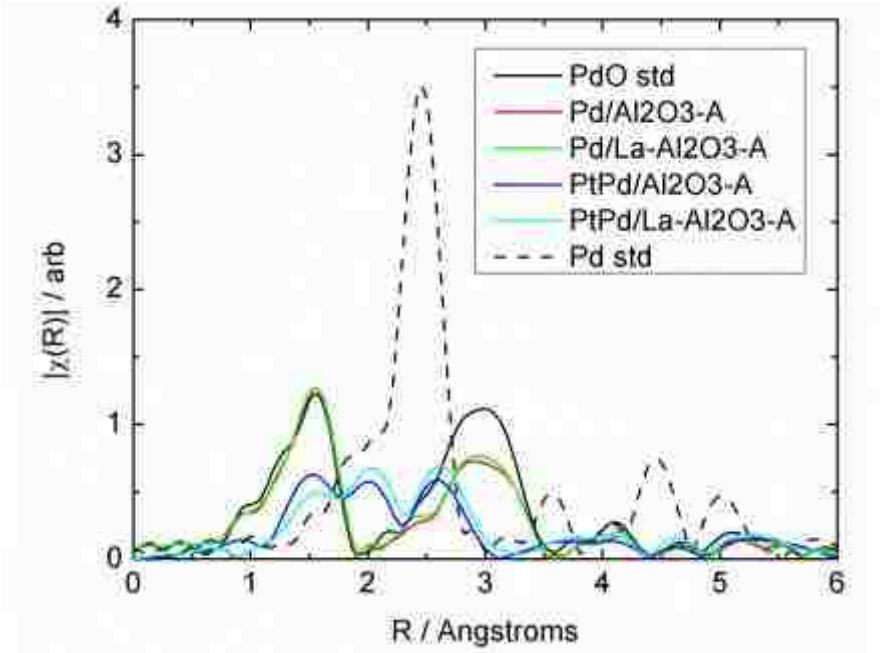

Figure 8(c). Fourier Transform EXAFS Pd K edge results for the aged samples. The monometallic samples show peaks corresponding to Pd-O and a second shell Pd-Pd. The lower amplitude for the second shell is consistent with small, dispersed, PdO on the surface of the catalyst. In contrast, the bimetallic samples show peaks consistent with Pt neighbors as well as Pd neighbors for metallic Pd and only the first shell oxide, suggesting that the oxide is now a dispersed phase. This plot shows both supports.

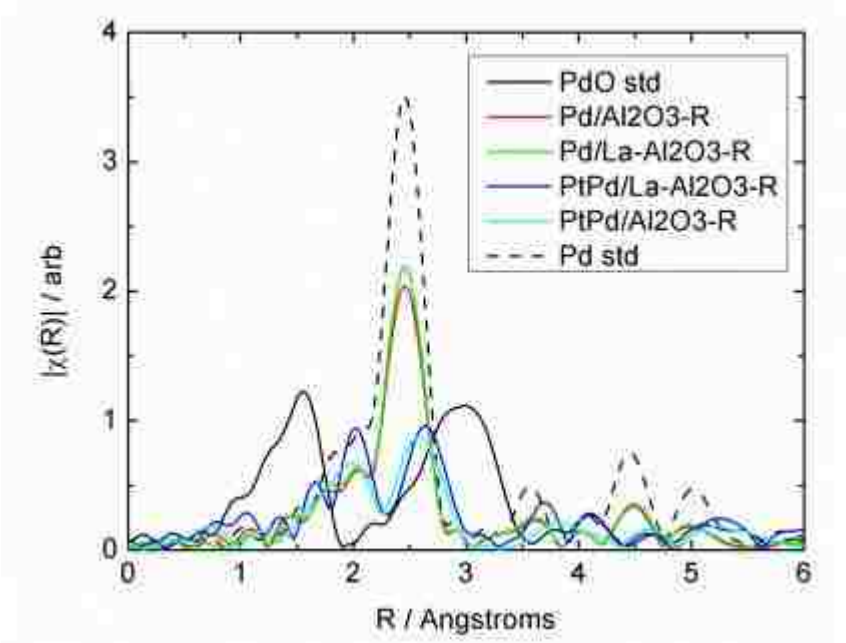

Figure 8(d). EXAFS Pd K edge results for the aged + reduced samples. The monometallic samples show a Pd-Pd peak with no higher shells, consistent with small metal particles (which cannot be seen via XRD). The bimetallics show co-existence of the alloy and some dispersed Pd on the catalyst, as confirmed also by STEM-EDS. This plot shows both supports.

Table 3. EXAFS and XANES Data for Monometallic Samples.

		XANES Fit						
Sample	Treatment	Pd(II) [Pt(II)]	Pd(0) [Pt(0)]	Scatter	N	R, Å	$\Delta\sigma^2$ (x 10^3)	Eo, eV
Pd Edge								
Pd/Al_2O_3	Aged	1.0	-	Pd-O	4.4	2.02	-0.8	0.7
				Pd-Pd	0.0	-	-	-
	Aged + Reduced	-	1.0	Pd-O	0.0	-	-	-
				Pd-Pd	9.4	2.74	1.0	-0.5
Pd Edge								
$Pd/La\text{-}Al_2O_3$	Aged	1.0	-	Pd-O	4.5	2.02	-0.6	0.6
				Pd-Pd	0.0	-	-	-
	Aged + Reduced	-	1.0	Pd-O	0.0	-	-	-
				Pd-Pd	10	2.74	1.0	-0.6
Pt Edge								
Pt/Al_2O_3	Aged	-	1.0	Pt-O	0.0	-	-	-
				Pt-Pt	11.7	2.76	0.7	-0.4
	Aged + Reduced	-	1.0	Pt-O	0.0	-	-	-
				Pt-Pt	11.6	2.76	0.2	-0.1
Pt Edge								
$Pt/La\text{-}Al_2O_3$	Aged	-	1.0	Pt-O	0.0	-	-	-
				Pt-Pt	12	2.76	0.6	-0.5
	Aged + Reduced	-	1.0	Pt-O	0.0	-	-	-
				Pt-Pt	11.2	2.76	-0.2	-0.3

The Fourier transforms on the Pd K edge of the bimetallic samples in Figure 8(b) are indicative of both Pd-Pd and Pd-Pt contributions. In the aged bimetallic catalysts, there is a metallic Pt-Pd phase as well as a PdO phase. After reduction there is no PdO left, and there are more Pd-Pd neighbors (coordination numbers provided in Table 4). The increase in Pd-Pd neighbors on the aged plus reduced catalysts likely indicates a separate phase of PdO that becomes metallic after the reduction treatment. Had this PdO phase been present on the surface of the bimetallic particles, one would have expected changes in the Pd-Pt coordination after reduction, but the change is minor.

Table 4. EXAFS and XANES Data for Bimetallic Samples.

		XANES Fit						
Sample	Treatment	Pd(II) [Pt(II)]	Pd(0) [Pt(0)]	Scatter	N	R, Å	$\Delta\sigma^2$ (x 10^3)	Eo, eV
Pd Edge								
Pt-Pd/Al_2O_3	Aged	0.30	0.70	Pd-O	1.7	2.05	0.0	0.5
				Pd-Pd	3.1	2.75	0.0	-2.4
				Pd-Pt	5.2	2.76	0.0	-1.3
	Aged + Reduced	-	1.0	Pd-Pd	4.8	2.75	0.0	-3.0
				Pd-Pt	6.0	2.76	0.0	-3.3
Pt Edge								
Pt-Pd/Al_2O_3	Aged	-	1.0	Pt-Pt	7.0	2.77	0.0	0.3
				Pt-Pd	4.5	2.76	0.0	6.8
	Aged + Reduced	-	1.0	Pt-Pt	7.0	2.77	0.0	0.5
				Pt-Pd	4.6	2.76	0.0	6.8
Pd Edge								
Pt-Pd/La-Al_2O_3	Aged	0.20	0.80	Pd-O	1.3	2.05	0.0	1.1
				Pd-Pd	3.5	2.75	0.0	-1.8
				Pd-Pt	6.8	2.76	0.0	-1.8
	Aged + Reduced	-	1.0	Pd-Pd	4.6	2.75	0.0	-1.1
				Pd-Pt	7.3	2.76	0.0	-0.9
Pt Edge								
Pt-Pd/La-Al_2O_3	Aged	-	1.0	Pt-Pt	7.3	2.77	0.0	0.3
				Pt-Pd	3.5	2.76	0.0	6.8
	Aged + Reduced	-	1.0	Pt-Pt	7.6	2.77	0.0	0.6
				Pt-Pd	4.0	2.76	0.0	6.3

Figures 9(a) and (b) show the EXAFS Pt L3 edge results. Figure 9(a) shows virtually no oxide on any aged catalysts from the Pt edge analysis. The aged bimetallic samples show Pt-Pd as well as Pt-Pt contributions due to the alloyed nanoparticles. The aged plus reduced Pt samples shown in Figure 9(b) are metallic on both the γ-Al_2O_3 and La-Al_2O_3 supports.

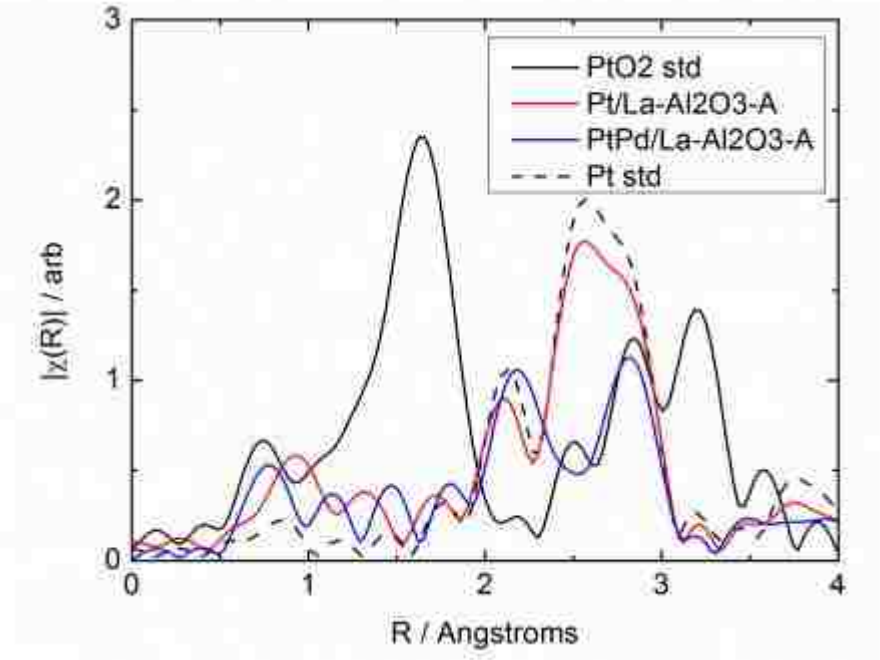

Figure 9(a). EXAFS Pt L3 edge results for the aged samples, showing very little difference between the aged sample and the reduced sample seen in figure (b).

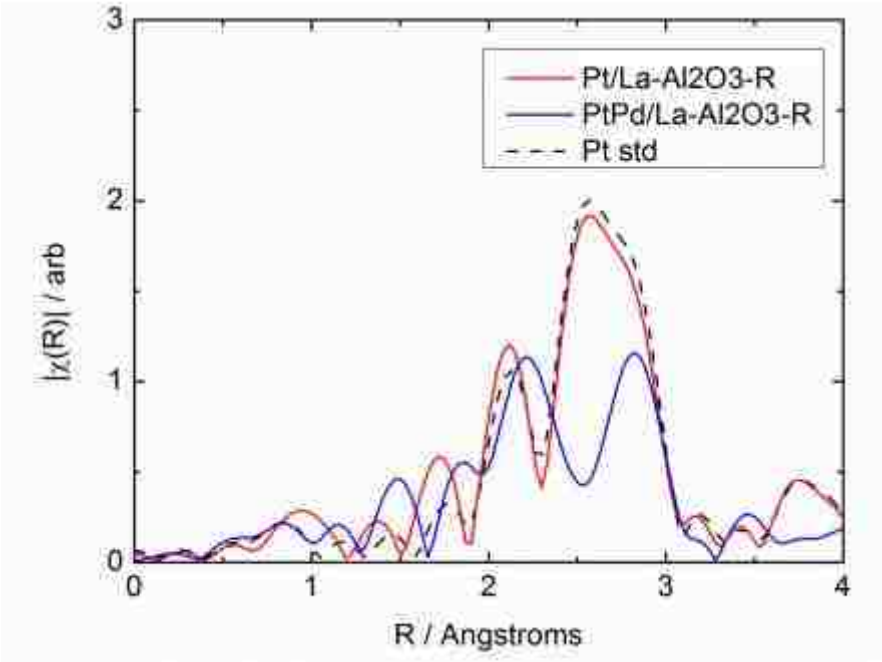

Figure 9(b). EXAFS Pt L3 edge results for the aged + reduced samples.

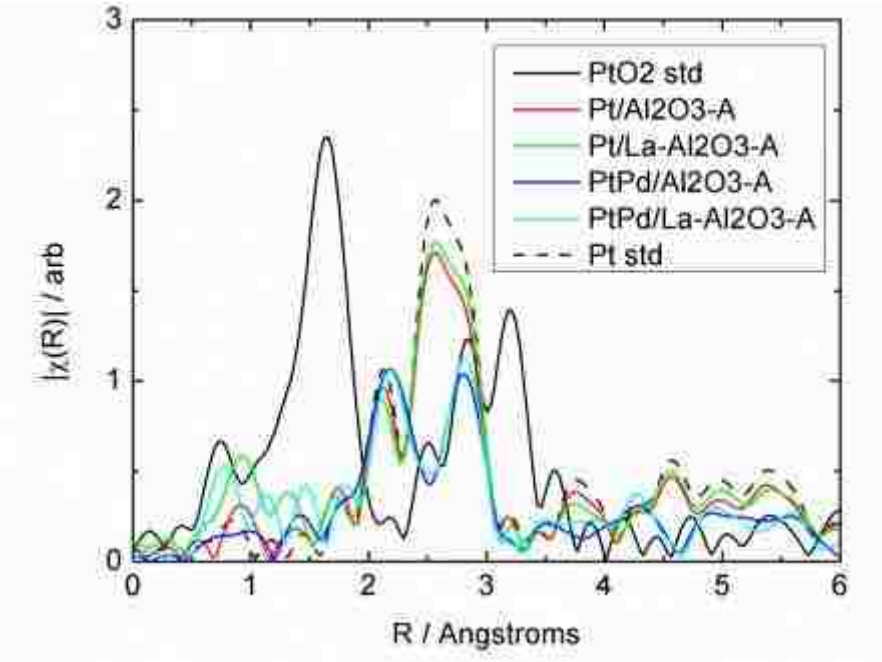

Figure 9(c). EXAFS Pt L3 edge results for the aged samples, showing very little difference between the aged samples and the reduced samples seen in figure (b). This plot shows both supports.

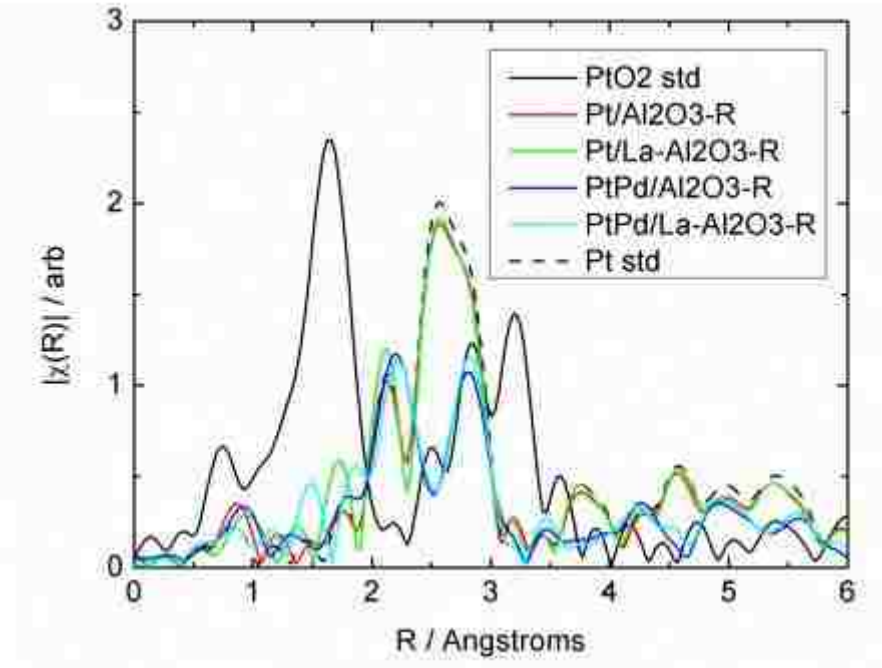

Figure 9(d). EXAFS Pt L3 edge results for the aged + reduced samples. This plot shows both supports.

The coordination numbers indicate large bulk-like particles, which are also consistent with the sizes determined from XRD. Again, the Fourier transforms of the bimetallic Pt-Pd aged plus reduced samples are indicative of Pt-Pt and Pt-Pd contributions. On the Pt edge there was no change caused by the reduction. The metallic particles remained the same. The reduction only turned the dispersed PdO phase into small metallic Pd nanoparticles on the bimetallic catalysts.

Table 4 provides the coordination numbers for the bimetallic samples used in this study. The table includes the average number of nearest neighbors surrounding each atom on the Pd edge (Pd_O, Pd_Pd, and Pd_Pt) and on the Pt edge (Pt_Pt and Pt_Pd). The total coordination number gives us an idea of the size of the particles. This number is around 12 for the reduced sample, consistent with the large particles we see via XRD and scanning transmission electron microscopy (STEM). The distribution of Pt and Pd within the nanoparticles in the reduced state can be inferred from the numbers of nearest neighbors. Pt has approximately 7 Pt nearest neighbors and 4 Pd nearest neighbors. And correspondingly, Pd has about 7 Pt nearest neighbors and 4 Pd neighbors. The uncertainty in coordination numbers is ~10%. The similarity of coordination numbers on the Pt and Pd edges suggest that the nanoparticles have a composition that is Pt-rich and uniform (i.e. not core shell). This agreement between the coordination numbers for the Pt and Pd edges is not seen in the oxidized state of the sample. First, we see a lower total coordination number of metal atoms for the Pd compared to the Pt edge. We can explain this in terms of the presence of Pd oxide. Since some of the Pd atoms have O neighbors, there is a lower total number of Pd and Pt atoms present as neighbors. There is very little change in the coordination seen on the Pt edge after the sample is reduced. If the Pd were present as an oxide on the surface of the bimetallic particle, we would have expected some change in the coordination seen on the Pt edge. In fact, the change is only seen on the Pd edge. This leads us to suggest that the Pd is present as a separate phase, which gets reduced in H_2 and then the number of metal neighboring atoms on average is increased for each Pd atom. The STEM/EDS results help us corroborate the model proposed here.

STEM images were taken on the aged plus reduced Pt, Pd, and Pt-Pd samples supported on La-stabilized alumina to help us determine particle size distributions. The

average particle size of Pd nanoparticles in the monometallic sample was 5.4 nm, which agrees with the low Pd-Pd coordination seen via EXAFS. This is also why there are very few large particles visible by SEM (Figure 10(b)). Most of the Pd is well dispersed and consistent with the stability of Pd to sintering when treated in oxidizing atmospheres. SEM backscattered electron images did not show many Pd particles on either support. However, on the monometallic Pt sample, the SEM image shown in Figure 10(c), shows many large particles, which would explain the larger average size of 34 nm found by XRD, and the EXAFS coordination near 12. Note that Figure 10(c) had a magnification 4 times lower than the other three images in Figure 10. The aged plus reduced Pt-Pd/La-Al_2O_3 had a bimodal distribution of particle sizes. Figures 11(a) and (b) show STEM images taken at different magnifications which illustrate the different particle sizes throughout the sample. Figure 11(c) is the particle size distribution for this sample. Due to the bimodal size distribution, we have divided the particles into two groups (the particles smaller than 1 nm and those larger than 1 nm). The number average, surface average, and volume average diameters for the group of nanoparticles less than 1 nm was 0.67 nm, 0.74 nm, and 0.77 nm, respectively. The number average, surface average, and volume average diameters for the group of particles greater than 1 nm was 16.4 nm, 24.4 nm, and 31.1 nm, respectively. The latter compares favorably with the XRD derived diameter of 25 nm (which must be multiplied by 4/3 to derive the equivalent diameter for a spherical particle). [35] Figure 10(d) is the SEM image of aged plus reduced Pt-Pd/La-Al_2O_3. The particle sizes shown in the image are similar to the particle sizes found by TEM and XRD. The overall composition of the bimetallic Pt-Pd sample was 38 at. % Pt and 62 at. % Pd, as determined by EDS. As shown below, the average composition of the larger metallic particles was Pt-rich, which was also seen from the EXAFS coordination numbers.

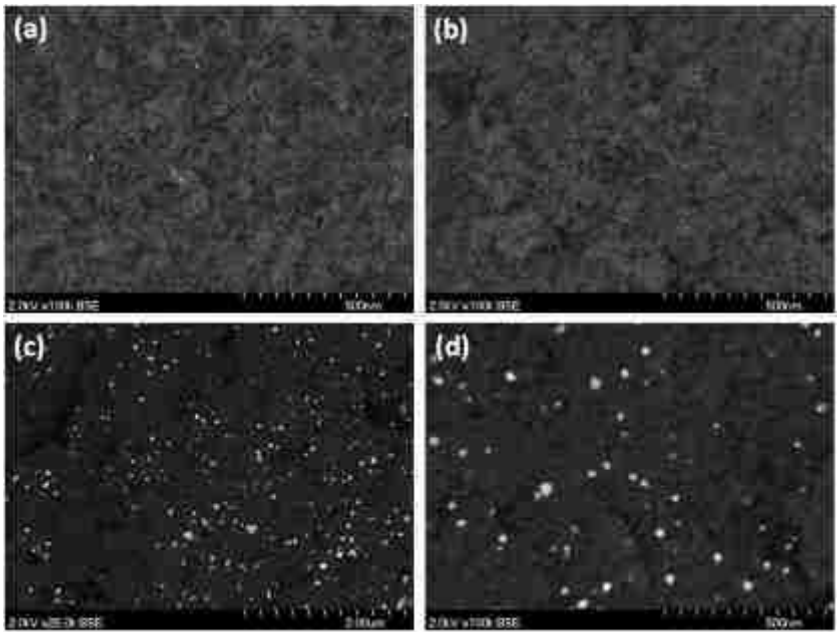

Figure 10. SEM back-scattered electron images of aged plus reduced (a) Pd/γ-Al_2O_3; (b) Pd/La-Al_2O_3; (c) Pt/La-Al_2O_3; and (d) Pt-Pd/La-Al_2O_3. (c) was taken at a magnification 4 times lower than the other images since the particles are much larger and consequently there are fewer particles present. The monometallic Pd samples show very few Pd particles because the majority are too small to see via SEM.

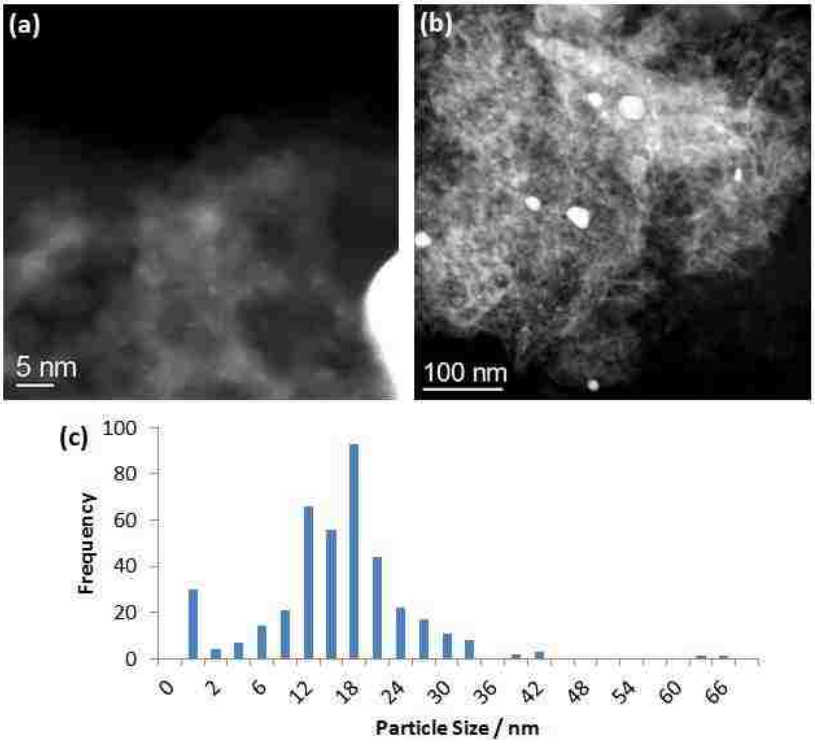

Figure 11. STEM image of (a) dispersed phase and (b) large particles in the aged plus reduced Pt-Pd/La-Al_2O_3 catalyst; (c) particle size distribution.

It was important to identify the PdO phase in the bimetallic catalyst to help us explain the EXAFS coordination numbers we found and the discrepancy between the overall EDS analysis and the analysis of the larger metallic particles. The Oxford INCA software was used to acquire EDS maps. A spectrum image was obtained which has a spectrum associated with each pixel in the image. Specific regions of the sample could then be chosen and a spectrum derived for all the pixels in the chosen regions. Figure 12 shows a typical image of the bimetallic reduced sample. It contains 6 nanoparticles greater than 20 nm in diameter. Each particle has a box around it to indicate that the composition was determined for each of those boxed regions. The mapping software assigns colors based on the abundance of a specific element. Pd is shown as red, and Pt is shown as green. A sum spectrum was obtained to determine the composition of the entire region imaged. Then the residual composition was derived by subtracting the spectra of the 6 particles from the sum spectrum. Using this method, we found that the residual area had a Pd composition of 72 at. % suggesting that the dispersed phase is Pd-rich. This explains the low Pd-Pd coordination obtained from EXAFS. If Pd was uniformly distributed throughout the sample in the large particles as well as the particles around 1 nm, then the compositions would have been similar to the overall average. Instead, we find that the larger particles are Pt-rich and the dispersed phase is Pd-rich.

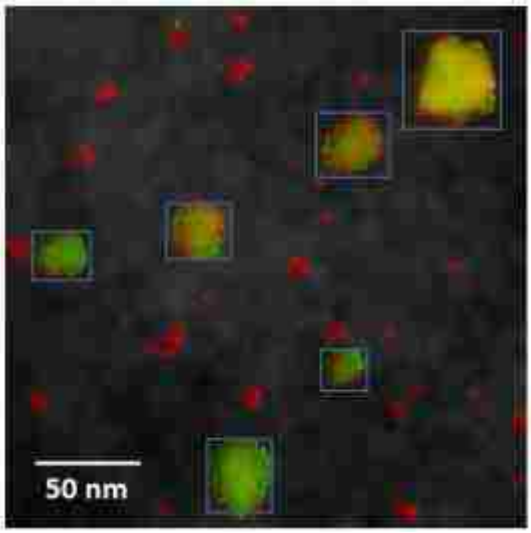

Figure 12. AC-STEM image of aged plus reduced Pt-Pd/La-Al_2O_3 with superimposed results from EDS mapping where Pt is shown in green and Pd in red. The boxes show the nanoparticles which contain Pt and Pd, and a dispersed phase which is brighter than the surrounding support. EDS mapping allowed us to derive the average composition of the particles within the boxes, as well as the dispersed phase, which contains primarily Pd.

To understand the structure of individual nanoparticles, spot EDS was performed on specific regions of a single particle. Figure 13 shows two of the particles that were analyzed. The boxes are the regions from which EDS spectra were obtained, and the corresponding atomic percentages of Pt and Pd are provided. For high resolution compositional mapping, we also used a JEOL JEM 2100F AC, where EDS mapping allowed us to obtain average compositions of the near surface region as well as the entire nanoparticles. There was no evidence for a core-shell structure in any of the particles that were analyzed. There seems to be a slight segregation of Pd to the surface of the nanoparticles. The large bimetallic nanoparticles, however, were always rich in Pt, which was consistent with the composition calculated from XRD.

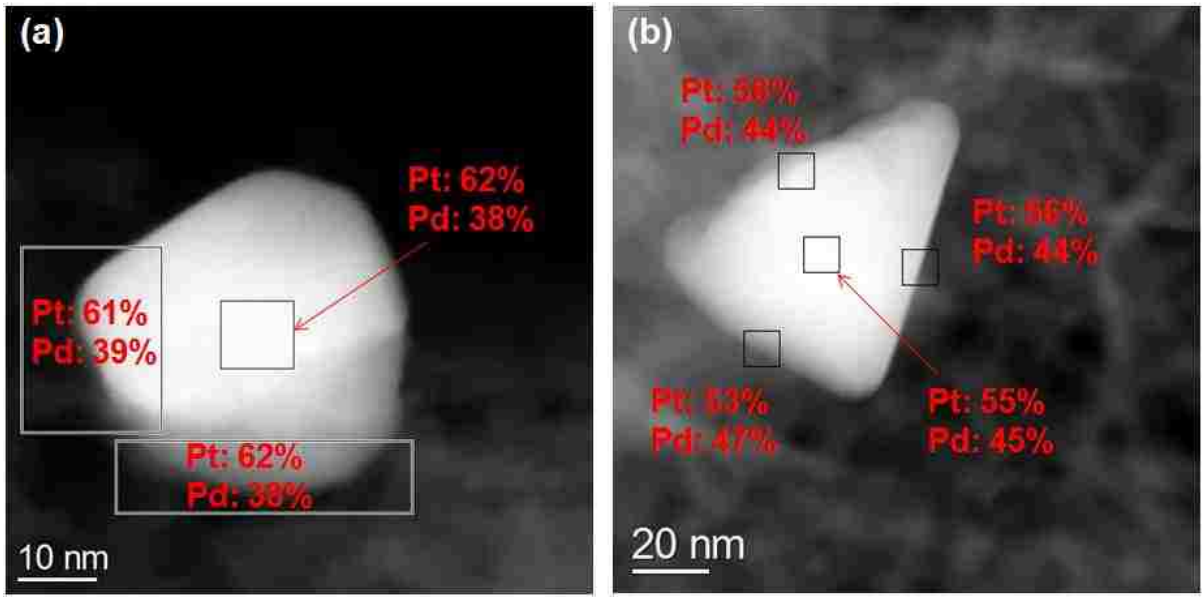

Figure 13. STEM images of two Pt-Pd particles in the aged plus reduced catalyst supported on La-Al_2O_3 which show the regions where EDS was performed and the corresponding atomic percentages of Pt and Pd.

These results show that the monometallic Pd catalysts were well dispersed in both the aged and aged plus reduced state. The sintering of Pd nanoparticles was not very pronounced during the treatment in air at 750°C. As shown by us previously, [36] the sintering of Pd becomes significantly enhanced when heated at 900°C, especially with 10% H_2O, since PdO decomposes to form metallic Pd which sinters much faster than PdO. In contrast, Pt sinters quite rapidly when aged at elevated temperatures under oxidizing conditions, and the sintering of Pt was more pronounced leading to larger particles on the La-Al_2O_3 support.

Similar rates of sintering were seen on the Pt-Pd catalysts. When compared to the Pt/γ-Al_2O_3, the Pd had only a minimal effect on the final particle size, but when compared to Pt/La-Al_2O_3 we can state that Pd slows the rate of sintering, yielding smaller particles in the final aged catalyst. The STEM/EDS results also show that the bimetallic sample shows a pronounced bimodal particle size distribution, with a highly dispersed Pd-rich phase having particles around 1 nm in diameter, and larger Pt-Pd particles which are Pt-rich. Figure 14 shows a schematic describing the microstructure of the catalysts after aging and the subsequent reduction. We have carefully probed the internal structure of the bimetallic nanoparticles and did not find any evidence for a core-shell structure neither did we see any pronounced segregation of Pd to the surface. Core-shell Pt-Pd structures can be prepared via colloidal routes, [37] but our aging in air may change the morphology and therefore, the core-shell structures cannot help explain enhanced performance of the automotive bimetallic catalysts. If the nanoparticles had been covered by a layer of Pd, they would have behaved very differently since the Pd could transform into PdO. Our catalyst aging was performed under isothermal conditions at 750°C in air, but it does not show any surface PdO on the bimetallic Pt-Pd particles, as shown in the HR-TEM image in Figure 15. However, we did our studies without the presence of water vapor, and without the other constituents of automotive exhaust. Hence, further work is needed to extend the study to more realistic exhaust treatment conditions.

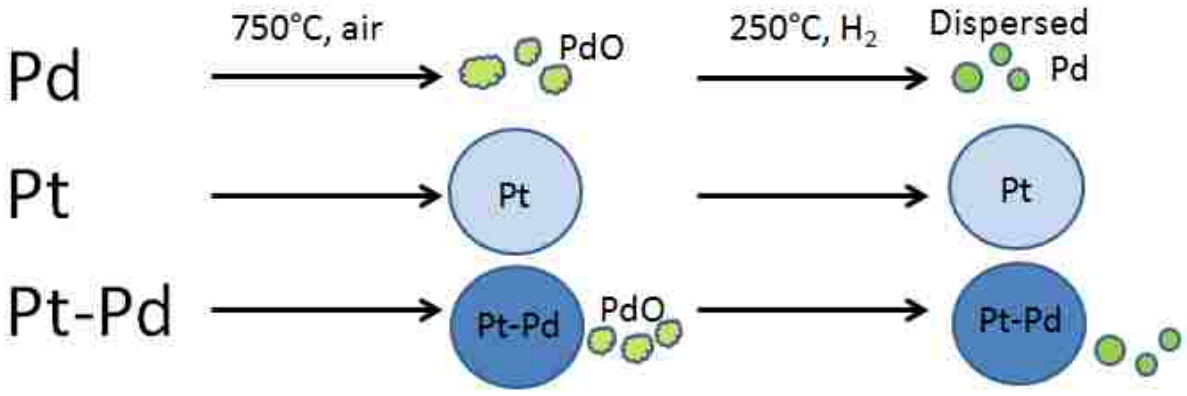

Figure 14. Schematic diagram showing the evolution of aged and aged plus reduced Pt, Pd, and bimetallic Pt-Pd particles. Aging in air causes Pd to form an oxide, while the particle size stays small. The reduced catalyst shows only small Pd particles. The Pt grows in size during aging, but stays metallic. The bimetallic also grows in size and both Pt and Pd stay metallic in the form of large particles (about 25 nm in diameter). There is also a dispersed Pd phase which can be seen via STEM-EDS and whose presence is confirmed by EXAFS and XANES.

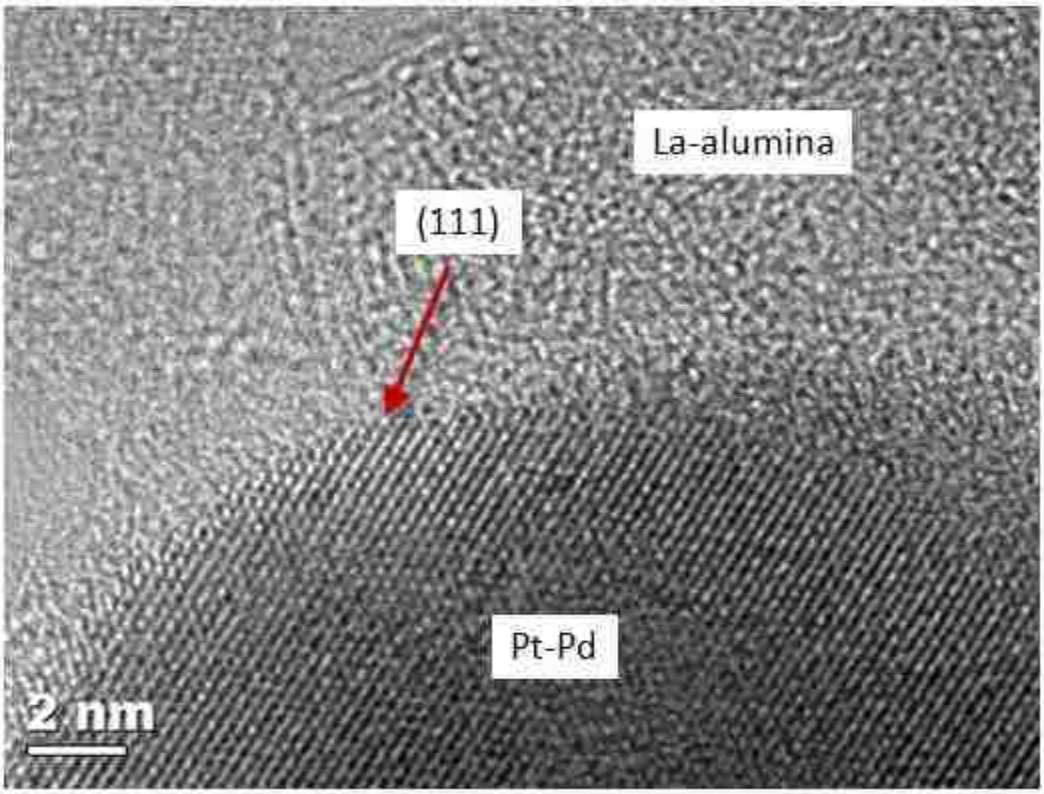

Figure 15. HR-TEM image of Pt-Pd/La-Al_2O_3 aged at 750°C for 10 hours in air clearly showing no PdO on the surface of the nanoparticle.

Summary/Conclusions

STEM/EDS, XRD, SEM, and XAS were used to explore the microstructure of bimetallic nanoparticles that were aged in air at 750°C for 10 hours. Our objectives were to study the influence of lanthana, which is used as a stabilizer for the alumina supports, and to study the improvement in catalyst durability due to the addition of Pd to Pt. We found that the La-Al_2O_3 had a detrimental influence on the sintering of the Pt-only catalysts; however, it was beneficial for the dispersion of PdO as seen in the slightly larger PdO XRD peak on alumina compared to La-alumina (Figure 3). This will be discussed further in future work. With regard to durability, we found that the Pt-Pd particle sizes were between those of the Pt on alumina and Pt on La-alumina. This would suggest that the improvement in particle size or dispersion due to the added Pd is not very significant. In fact, the literature shows that the addition of Pd only makes a significant difference for samples that have been aged at

temperatures at 800°C or above [1, 8, 9] because it prevents the formation of anomalously large particles. At these temperatures, the Pd containing catalysts had almost twice the dispersion of the Pt-only catalysts while after lower temperature aging, the difference was not as pronounced. The engine-aged bimetallic samples studied by Ward *et al*. [21] showed comparable mean particle sizes to Pt-only catalysts. We conclude that after aging at 750°C in air for 10 hours the improvement in durability was not significant.

Another major objective of this study was to determine how Pd improves the catalytic behavior of Pt in the bimetallic catalysts during operation under oxidizing conditions. By using XAS, we determined that only 20% to 30% of the Pd in the bimetallic catalysts was present in the form of an oxide. The oxide existed as a separate phase and not as a layer on the Pt-Pd bimetallic nanoparticles. This is a significant difference compared to the monometallic samples. The Pd-only catalyst would consist of 100% oxide after aging under these conditions. The co-existence of Pt and Pd in metallic nanoparticles must be the key attribute of these bimetallic catalysts. There was no evidence for a core-shell structure, and the extent of Pd segregation to the surface is minimal. Our results show that the surface does not get covered with an oxide, rather any PdO exists as a separate phase. While this is a highly dispersed PdO phase, we would expect a similar phase to be present also on the monometallic Pd catalyst. Therefore, the improvement in catalytic behavior seen in these catalysts is likely due to the catalytic sites on these bimetallic particles being more active for some of the reactions. In NO oxidation this may not be very important, but for hydrocarbon oxidation this may be a significant difference. [3]

Experimental Section

Catalyst Preparation

Dispal (boehmite) from Sasol was calcined at 650°C for 10 hr to make γ-alumina, and the BET surface area was determined to be 153 m^2 g^{-1}. The BET surface area was measured on a Micromeritics Gemini 2360 instrument under liquid nitrogen at 77K. The La-alumina contains 4 wt. % La_2O_3 from W. R. Grace (MI-386) and has a BET surface area of 176 m^2g^{-1}. The Pt/La-Al_2O_3 and Pt/γ-Al_2O_3 catalysts were prepared by incipient wetness using an

aqueous solution of chloroplatinic acid (8 wt. % H_2PtCl_6). The Pd/γ-Al_2O_3 and Pd/La-Al_2O_3 catalyst were prepared by incipient wetness using a Pd (II) nitrate solution (10 wt. % in 10 wt. % nitric acid). All monometallic samples had loadings of 0.8 wt. %. To synthesize the bimetallic samples, tetraamine Pd (II) nitrate (10 wt. % in water) was added to the 0.8 wt. % Pt catalysts by incipient wetness to make a 40:60 molar ratio of Pt to Pd. This led to a total metal loading of approximately 1.3 wt. %.

Catalyst Treatments

The six samples were first calcined in ambient air in a box furnace at 600°C for 4 hr. Then each sample was reduced in flowing 7% H_2/N_2 in a quartz tube furnace at 550°C for 2 hr. The samples were then aged in ambient air in a box furnace at 750°C for 10 hr. The catalysts in this state will be referred to as "aged" or "A." A portion of each catalyst was further reduced in 3.5% H_2/He at 250°C for 1 hr at the beamline for EXAFS experiments or reduced in 7% H_2/N_2 for 1 hr at 250°C in the laboratory for STEM analysis. These catalysts will be referred to as "aged + reduced" or "R." The BET surface area for the γ-Al_2O_3 support after these treatments was 139 $m^2\ g^{-1}$, and the surface area for the La-Al_2O_3 was 172 $m^2\ g^{-1}$.

X-ray Diffraction (XRD)

X-ray diffraction measurements were preformed on a Rigaku SmartLab diffractometer using Cu K_α radiation. The powders were lightly pressed into a cavity in a plastic sample holder. The samples were run using Bragg Brentano geometry using a D/tex position-sensitive detector and a Ni K_β filter. Data was acquired with a rate of 16°/min from 15° to 130°. A step size of 0.02 was used. All analysis was done using GSAS software.

Scanning Transmission Electron Microscopy (STEM) and Energy Dispersive X-ray Spectroscopy (EDS)

A JEOL 2010F 200kV FASTEM FEG (field emission gun) TEM/STEM was used to acquire STEM images. It has a GATAN GIF 2000 Energy Filter, JEOL bright and dark field STEM detectors, GATAN bright and dark field STEM detectors, and an Oxford Instruments ISIS/INCA EDS system with an Oxford Pentafet Ultrathin Window Detector (UTW). Gatan Digital Micrograph was used for all image processing, and INCA was used for the analysis of

all EDS data. Pt and Pd L lines were used in the EDS analysis. This microscope has a point-to-point resolution of 0.194 nm and a minimum spot size in STEM mode of 0.14 nm. However, for compositional analysis by EDS, we used a probe size of 1.0 nm to obtain adequate counting statistics. For high resolution compositional mapping, we also used a JEOL JEM 2100F AC (aberration-corrected STEM). The nominal point resolution and ultimate probe size for this instrument was similar to that of the JEOL 2010F, but the aberration corrector provides a much higher probe current for EDS analysis. The microscope is configured for both traditional TEM as well as STEM. Images for this work were taken using a high angle annular dark field (HAADF) detector. The electron source on this microscope is a field emission gun, and the microscope is equipped with a STEM mode spherical aberration corrector (Cs).

High resolution TEM (HR-TEM) images were taken using the FEI Titan 80-300 environmental transmission electron microscope (E-TEM) at the Center for Functional Nanomaterials at Brookhaven National Laboratory. This microscope is equipped with an objective-lens aberration corrector and has a spatial resolution of 0.08 nm in HR phase contrast mode.

Scanning Electron Microscopy (SEM)

The scanning electron microscope (SEM) used for this work was a Hitachi S-5200. This SEM is capable of a resolution of 1.7 nm at 1 kV and 0.5 nm at 30 kV. It was operated at 2kV to image the samples in backscattered mode as well as in the secondary electron mode. The catalyst sample was prepared by pressing the powder onto double-sided carbon tape which was attached to the sample holder.

X-ray Absorption Spectroscopy (XAS)

Pd K-edge and Pt L3-edge X-ray absorption measurements were conducted at room temperature on the insertion device beamline 10-ID-B at the Advanced Photon Source (APS) at Argonne National Laboratory using transmission mode. The amount of catalyst loaded into the sample holder was selected to obtain an edge step of 0.3 to 1.0 for the given experiment. Each aged catalyst was ground to a fine, uniform consistency and compressed into a stainless steel sample holder (die) with 6 cylindrical openings for up to 6 samples. The

die was inserted into a quartz tube sample cell which had an inner diameter of 3/4" and X-ray transparent end caps made of Kapton. The cell allowed for flow of gases, and it was mounted on a movable sample stage which allowed for sample alignment in the beam path. After XAS was completed on the aged samples, the sample cell was taken off line to perform additional sample treatments. A flow of 50 cm^3 min^{-1} of He was first delivered to the cell for 5 minutes to purge O_2. Then a reducing environment of 3.5% H_2/He was provided for 1 hour at 250°C, followed by a purge of He for 5 minutes at temperature. This was done to prevent formation of Pd hydrides during the cool-down. Then, the cell was removed from the furnace where it cooled to room temperature under flowing He. Once it reached room temperature, the sample cell was disconnected from the gas feed and sealed with He inside. X-ray absorption measurements were then performed on the aged plus reduced samples.

Linear combination fitting (LCF) of the data to both metallic and oxide standards was performed to determine the oxidation state of each metal in the near-edge portion of the spectra (XANES). Analysis of the extended portion of the spectra (EXAFS) provided bond distances and coordination of each metal, which indicated the extent of Pt-Pd alloying and particle sizes (nanoparticles versus bulk material). ATOMS [26] and FEFF6 [27] were the software packages used to generate *ab initio* photoelectron scattering models of structures containing Pt, Pd, and O. Face centered cubic (FCC) Pt and Pd paths were created using data from Kittel. [28] Data from Waser *et al.* [29] was used to generate a PdO structure (P42/mmc; antifluorite derivative) with an origin shift of (0,1/2,0) to comply with the positions listed in the International Tables for Crystallography [30] with Pd in site 2c and O in site 2f. To account for alloying of Pd and Pt, substitution of Pd sites with Pt (and vice versa) was used. Then a least squares fitting algorithm was used to fit the models to the experimental EXAFS spectra. This allowed the determination of bond distance as well as coordination number for Pt and Pd absorbers.

Acknowledgements

We acknowledge financial support from the following grants: NSF GOALI CBET-1067803, NSF IGERT DGE-0504276, and NSF PIRE OISE-0730277. Portions of this work were performed at beamline 10-ID-B (MRCAT) of the Advanced Photon Source at Argonne

National Laboratory. MRCAT operations are supported by the Department of Energy and the MRCAT member institutions. Use of the Advanced Photon Source was supported by the U.S. Department of Energy, Office of Science, Office of Basic Energy Sciences, under Contract No. DE-AC02-06CH11357. JTM is supported as part of the Institute for Atom-Efficient Chemical Transformations (IACT), an Energy Frontier Research Center funded by the U.S. Department of Energy, Office of Science, Office of Basic Energy Sciences. Some of this work was performed using the JEOL JEM 2100F AC at General Motors Global R&D, and some work was performed using the FEI Titan 80-300 environmental transmission electron microscope (E-TEM) at the Center for Functional Nanomaterials at Brookhaven National Laboratory. We also acknowledge NSF support for acquisition of the XRD via the Major Research Instrumentation grant CBET 0960256. We thank Hien Pham for assistance in obtaining the SEM images.

Chapter 4

Adatom Emission From Nanoparticles: Implications for Ostwald Ripening

This chapter is based on an extended abstract published in Microscopy and Microanalysis, and the complete chapter will be submitted for publication shortly. The abstract published in Microscopy and Microanalysis is shown in the Appendix. The following chapter is based on a manuscript being prepared for submission with the following co-authors:

Goeke, R.S., Challa, S.R., Thüne, P.C., Niemantsverdriet, J.W. (Hans), Fernando, N., Kiefer, B., Kim, C.H., Datye, A.K.

This work was performed using the following funding sources: NSF GOALI CBET-1067803, NSF IGERT DGE-0504276, and NSF PIRE OISE-0730277. The authors would like to thank Sandia National Laboratories for the use of the 10kV Temescal electron beam evaporator. Sandia National Laboratories is a multi-program laboratory managed and operated by Sandia Corporation, a wholly owned subsidiary of Lockheed Martin Corporation, for the U.S. Department of Energy's National Nuclear Security Administration under contract DE-AC04-94AL85000. Thank you also to Andrew de la Riva for his expertise on the JEOL 2010F TEM.

Low-temperature aftertreatment catalysts have become increasingly important in recent years due to a tighter regulatory environment and the demand for clean energy. Specifically, Pt and Pd are the precious metals used in diesel oxidation catalysts (DOCs) for hydrocarbon (HC), carbon monoxide (CO), and nitrogen oxide (NO) oxidation in diesel engine exhaust. High fuel efficiency engines provide lower exhaust temperatures, hence the need for achieving low light-off temperatures. The challenge is that the catalysts must be active at these low temperatures. Typically, CO and HC oxidation need to begin at temperatures below 200°C while minimizing Pt loading. A major problem with catalysts is that they lose their activity during use. Pd is added to Pt to improve the performance of these catalysts but the underlying mechanisms are not well understood. Previous reports in the literature indicate that Pt sinters and has poor durability under oxidizing conditions. [4, 8] The restructuring of Pt foils under oxidizing conditions can be quite dramatic and it has been

suggested that vapor phase transport of Pt might play an important role. [14] However, to study the role of vapor phase processes in supported catalysts is difficult because atoms that are emitted can be adsorbed in other parts of the catalyst. In contrast, on a model catalyst, atoms that are emitted will be lost to the vapor phase; hence, we can study the importance of vapor phase processes. Model catalysts used for TEM studies involve metal nanoparticles on oxide thin films mounted on metal grids. These samples are not suitable for heating in elevated temperatures in air. In this study we have used a novel form of model catalyst based on silicon MEMS technology that allows heating in air at elevated temperatures. Using this approach we can now study the role of vapor phase processes during catalyst sintering.

Two mechanisms of catalyst sintering are known. One is particle migration and coalescence, where particles migrate along the surface of the support and coalesce to form larger particles, and the second is Ostwald ripening. During Ostwald ripening particles emit atoms (or mobile species such as PtO_x) which migrate from smaller particles to form larger particles. The mobile species could travel along the surface of the support or through the vapor phase. In previous studies, it was shown that the sintering of platinum on an alumina support is primarily due to Ostwald ripening. [12, 13] An in-situ transmission electron microscope (TEM) was used to explore the mechanism. The samples were aged at 650°C in 10 mbar of air. The Pt particles remained immobile, and the nanoparticles with a larger initial diameter tended to grow while those with a smaller initial diameter tended to shrink. The authors did not observe any loss of Pt, except when their samples were exposed to intense electron beam doses. The in-situ studies are very useful and have provided data at low operating pressures (10 mbar). In this work we demonstrate that model catalysts can also be used at atmospheric pressure in air to gain insight into the processes of catalyst sintering.

The specific questions addressed in this work concern the nature of the mobile species responsible for Ostwald ripening and the relative importance of vapor phase or surface diffusion. Figure 16 is a schematic showing the phenomena that could be responsible for Ostwald ripening of a Pt catalyst in air. Mobile species emitted from the metal particles can travel through the vapor phase or over the surface of the support. It is known that a volatile oxide of Pt is formed in the presence of oxygen, and the stoichiometry of this oxide was determined to be PtO_2. [24] Previous work on model catalysts did not report any loss of

Pt, but these previous model catalyst studies were done at low pressures (10 mbar). [12] Experiments at atmospheric pressure under realistic operating conditions will help in developing a better understanding of the atomic scale processes that occur during aging of Pt catalysts and to understand the role of Pd.

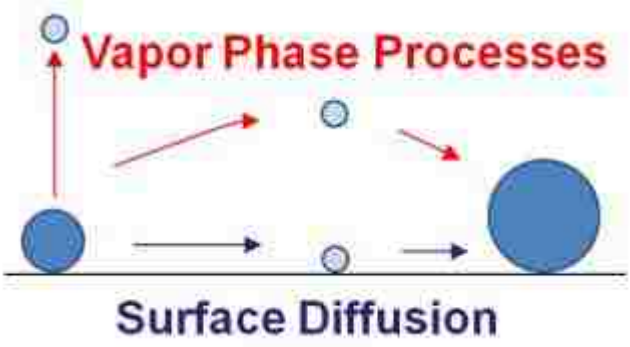

Figure 16. Schematic showing phenomena that could be responsible for Ostwald ripening of a Pt catalyst in air. The vapor phase process is shown in red, and the surface diffusion process is shown in blue. In addition to interparticle transport, it is also possible to emit atoms into the vapor phase, which can be detected by the change in mass of these model catalyst samples.

In this work we use model TEM grids developed at Eindhoven University of Technology. [25] A schematic cross sectional view of a single TEM grid is shown below in Figure 17. These TEM grids have a silicon nitride membrane window which is electron transparent, and the top and bottom 3 nm are oxidized to SiO_2 by heating in air. The grids can be treated like normal TEM grids, but they can also be heated to high temperatures in air, something which is not possible on metal grids conventionally used for TEM studies. Electron beam evaporation was used to deposit Pt, Pd, and Pt-Pd of approximately 5Å in thickness on the silica surface. The average composition of the bimetallic samples after electron beam evaporation was 38 at. % Pt and 62 at. % Pd, as determined by EDS.

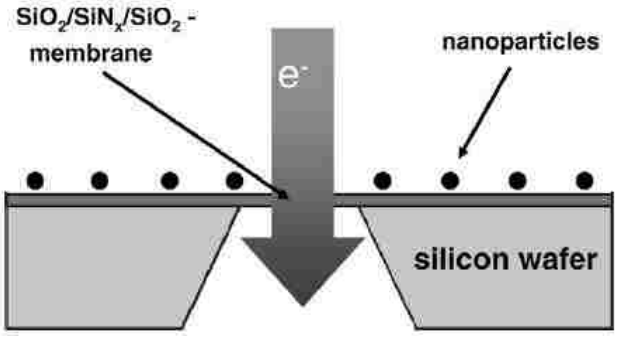

Figure 17. Side view of a SiO_2 TEM grid. [25]

The samples were reduced in flowing 7% H_2/N_2 at 750°C for 10 minutes and then imaged via TEM. This is considered the initial state of each sample. One set of samples was aged in flowing air at 650°C and 750°C for a short interval (two minutes) so that the initial stages of the sintering process could be studied. For these short-term aging experiments we used a SabreTube^{TM} thermal processing system which allows rapid heating (10 seconds to reach 750°C) and cooling of the specimen. A second set of samples was aged in flowing air in a tube furnace at 750°C and 800°C for 1.5 hours. Particle size distributions (PSDs) were determined using high-angle annular dark field scanning transmission electron microscopy (HAADF-STEM). High resolution transmission electron microscopy (HR-TEM) was used for lattice fringe analysis to determine the phase of the nanoparticles. This was confirmed by electron diffraction. Energy dispersive X-ray spectroscopy (EDS) was used to obtain compositions before and after aging and to determine the net emission of atoms. To find the percent loss of metal, two EDS methods were used to show consistency. One method compares the ratio of Pt to Si before and after aging, and the second method uses the absolute counts of Pt before and after aging to calculate the percent loss. Since 5Å (500 pm) of metal were deposited on each grid, one can multiply the percent loss determined from EDS by the 500 pm to quantify the number of pm lost. Due to limitations of our system, quantifying percent loss required a change of at least 5%.

Figure 18 shows the effect of aging conditions on the sintering of Pt and its emission in air. The characteristics of these samples (including the average diameter, the number of particles per square micron, and the ratio of the projected area/total area, assuming circular projections for all nanoparticles) are shown in Table 5. After aging at 750°C for 1.5 hr, 185 pm of Pt were lost. The size of the particles had grown substantially, with the maximum size being 97 nm. The sintering was not as dramatic for the shorter aging time of 2 min at 650°C and 750°C, and EDS showed negligible loss of Pt due to the limitations of our system. Extrapolating from 185 pm loss for 1.5 hr, we estimated the loss at 750°C for 2 min to be about 4 pm. Emission to the vapor phase is very low under those conditions, so the rate of surface diffusion must be faster than emission based on the increased average size of the particles shown in the figure. Another example of this is shown in Figure 31 in Chapter 5. This Pt sample was aged at 650°C for 15 s in 21% O_2/Ar to simulate air. The same region of the sample was imaged before and after aging. Some of the Pt nanoparticles are highlighted

in the before and after images to show that some of the particles have grown while others have shrunk. Some of the particles shrunk until they completely disappeared. One of the particles that disappeared was initially 2.5 nm or 2,500 pm. As shown in Figure 18, evaporation at this temperature for such a short time would cause the loss of only a couple pm of Pt at most, but we see that entire particles have disappeared. This must mean that surface diffusion leading to sintering is much faster than emission.

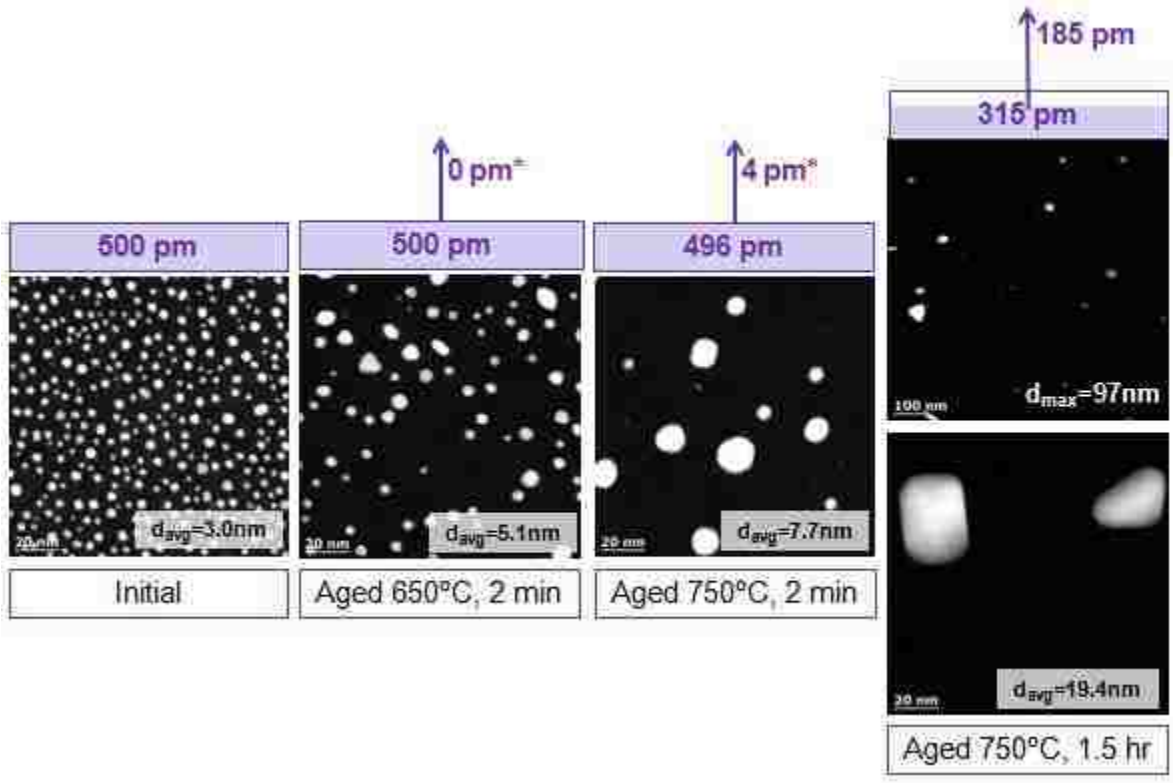

Figure 18. Effect of aging conditions on Pt sintering and emission in air. Calculated emission of Pt is shown. (* means estimated from extrapolation.)

We determined that Pt vapor phase emission becomes significant at 800°C. Pt/SiO_2 was aged at 800°C for 1.5 hr and lost 323 pm of Pt. Next, we changed the net emission by covering a sample during aging and redirecting some of the emission to the support to study the role of vapor phase transport. This Pt/SiO_2 sample was aged at 800°C for 1.5 hr. This sample lost 277 pm of Pt. Since the total emission of Pt on the uncovered sample aged at 800°C for 1.5 hr was 323 pm, this would mean that 46 pm were redirected to the support (323 pm – 277 pm = 46 pm). After the aging treatment, this sample showed a bimodal

particle size distribution. There were large, faceted particles and numerous small (less than 2 nm) particles. These small particles must have come from condensation because particles of this size would have ripened and disappeared at a very early stage. [38] We reduced the emission to a greater extent on the next Pt/SiO_2 sample. The Pt loss was 202 pm, meaning that 121 pm were redirected or essentially recycled back to the support. The vapor phase transport of these samples led to significant sintering and a very different particle size distribution. Figure 19 shows a typical Pt/SiO_2 sample in its initial state as well as the samples aged at 800°C for 1.5 hr with different extents of redirected emission. These results suggest that by covering a Pt/SiO_2 sample and aging it in air at 800°C for 1.5 hr, one can obtain similar results to the Pt/SiO_2 sample aged at 750°C for 1.5 hr. (See Table 5.) Initially there are over 21,000 particles/μm^2. After aging at 750°C for 1.5 hr and after aging at 800°C for 1.5 hr while covered, the number of large particles/μm^2 drops to around 30.

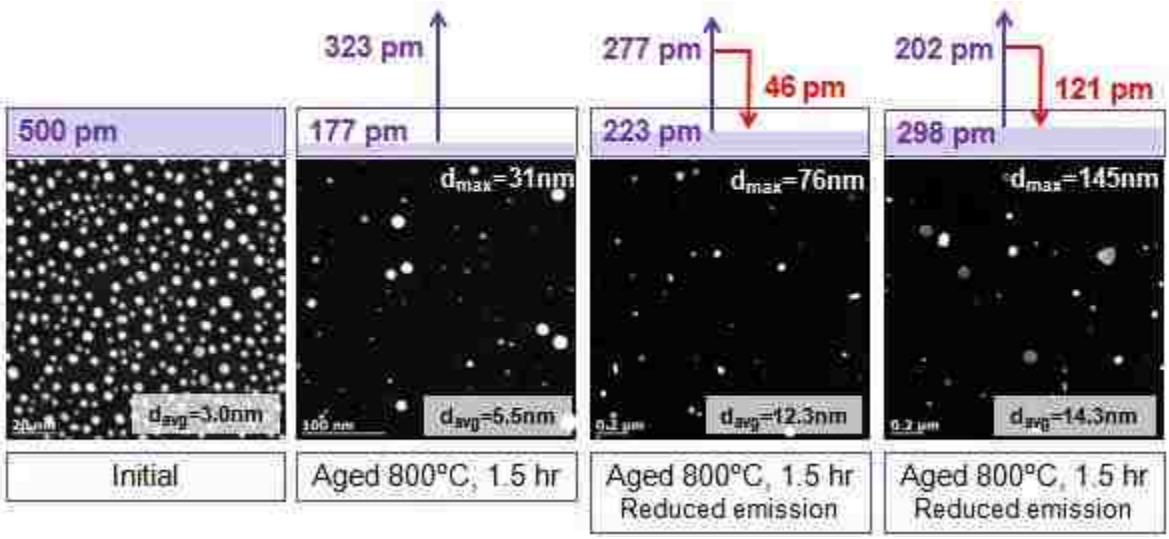

Figure 19. Pt/SiO_2 samples aged at 800°C for 1.5 hr showing the loss of Pt as well as the amount of Pt redirected back to the surface of the support from being covered. This allowed us to study the role of vapor phase transport.

Table 5. Characteristics of Pt/SiO_2 samples aged under different conditions. Some of the Pt samples had a bimodal distribution of particles after the aging treatment so in the table it is split into large particles (those greater than 2 nm) and small particles (those less than 2 nm).

	Mean Diameter (nm)	Particles/μm^2	Projected Area/ Total Area
Pt/SiO_2 initial	3.0	21,700±400	0.17
Pt/SiO_2 Aged 650°C, 2min	5.1	4,300±400	0.10
Pt/SiO_2 Aged 750°C, 2min	7.7	920±60	0.06
Pt/SiO_2 Aged 750°C, 1.5hr	19.4 (large particles*)	31±2	0.017
	1.0 (small particles*)	90±40	$8.0x10^{-4}$
Pt/SiO_2 Aged 800°C, 1.5hr	5.5 (large particles)	570±80	0.019
	1.0 (small particles)	700±200	$8.0x10^{-4}$
Pt/SiO_2 Aged 800°C, 1.5 hr (reduced emission 277pm loss)	12.3 (large particles)	36±2	0.01
	1.0 (small particles)	586±89	$1.9x10^{-3}$
Pt/SiO_2 Aged 800°C, 1.5 hr (reduced emission 202pm loss)	14.3 (large particles)	30±6	0.014
	1.0 (small particles)	800±200	$7.0x10^{-4}$

Some of the nanoparticles in the sample aged at 750°C for 1.5 hr and the covered samples aged at 800°C for 1.5 hr had different contrast in the HAADF-STEM images even though they were of similar size. This could be because some of the particles were a different species (i.e. a platinum silicide) or because some of the particles were round while others were flat. Electron diffraction showed that there was no species present other than Pt. (See Figure 20.) The difference in contrast of the particles will have to be explored further in future work.

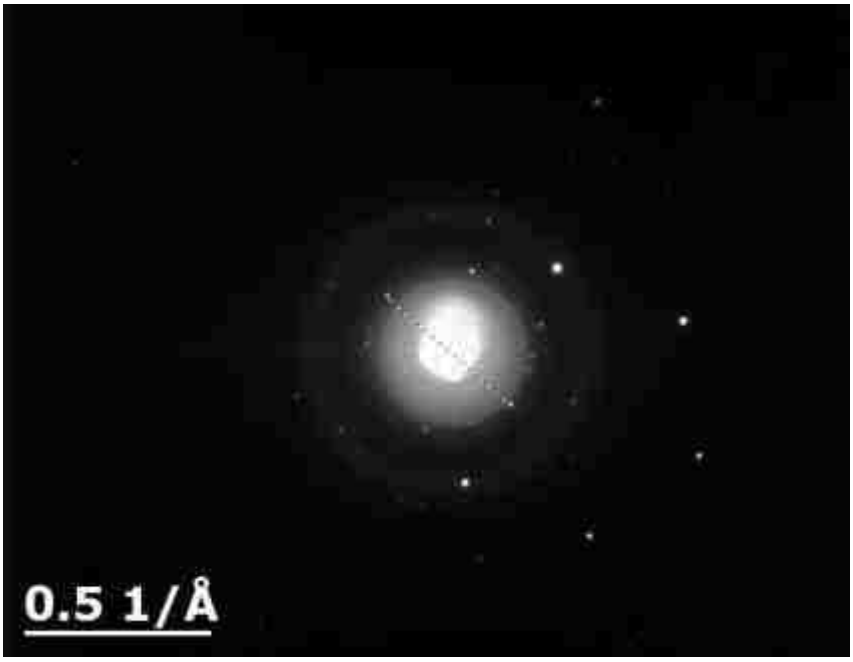

Figure 20. Electron diffraction pattern showing a covered Pt/SiO_2 sample after aging at 800°C for 1.5 hr. The dotted line gives a d_{111} of 2.27Å, the interplanar spacing of Pt.

The pure Pd samples do not show any emission and very little sintering when aged at 650°C for 2 min and 800°C for 1.5 hr, as shown by Figure 21. The increase of the mean diameter for Pd is due in part to the sample becoming oxidized and the corresponding change in shape. Pd becoming oxidized leads to a 68% increase in volume. After accounting for the increase, the mean size after aging at 650°C for 2 min is 3.6 nm. All the particles have not been completely transformed into PdO so accounting for the 68% increase in volume is likely underestimating the mean diameter after aging. The decrease in the number of particles before and after aging, as shown in Table 6, represents the small degree of sintering that occurs. There is little difference in the number of particles/μm^2 after aging at 650°C for 2 min and after aging at 800°C for 1.5 hr. This suggests that the sintering that occurred, happened while the Pd was still metallic. Pd had not yet become fully oxidized after aging at 650°C for 2 min (Figure 22), but after aging at 800°C for 1.5 hr, the lattice fringe analysis provided in Figure 23 shows that the particles had become fully oxidized.

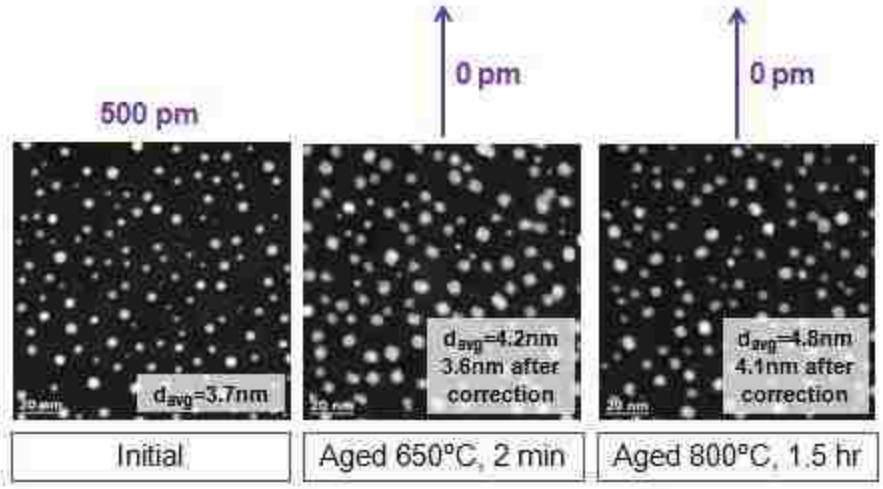

Figure 21. Effect of aging conditions on Pd sintering and emission in air. There is very little sintering and negligible emission under these conditions.

Table 6. Characteristics of Pd/SiO_2 in its initial state and after aging.

	Mean Diameter (nm)	Particles/μm²	Projected Area/Total Area
Pd/SiO_2 initial	3.7	8,700±500	0.10
Pd/SiO_2 Aged 650°C, 2min	4.2 3.6 after correction	7,800±900	0.12
Pd/SiO_2 Aged 800°C, 1.5hr	4.8 4.1 after correction	7,900±400	0.15

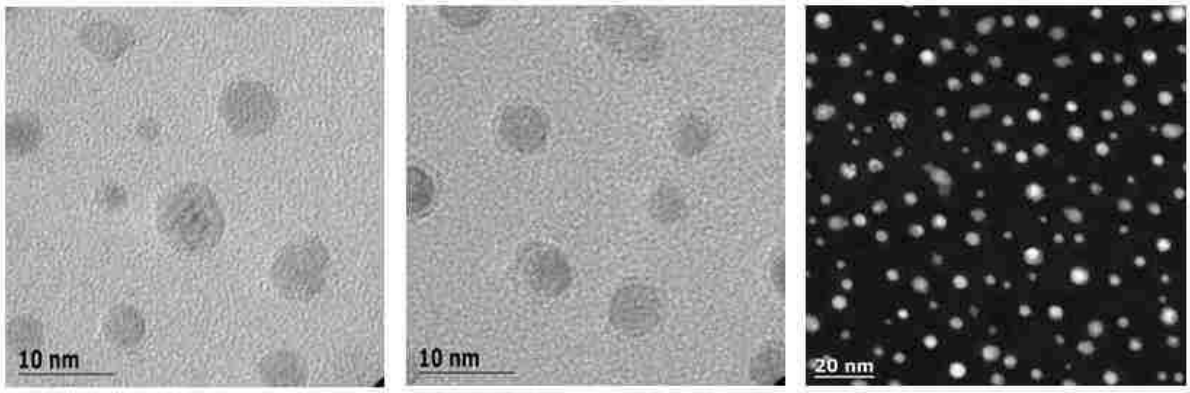

Figure 22. HR-TEM and HAADF-STEM images showing that the Pd sample after being aged at 650°C for 2 min is not fully oxidized.

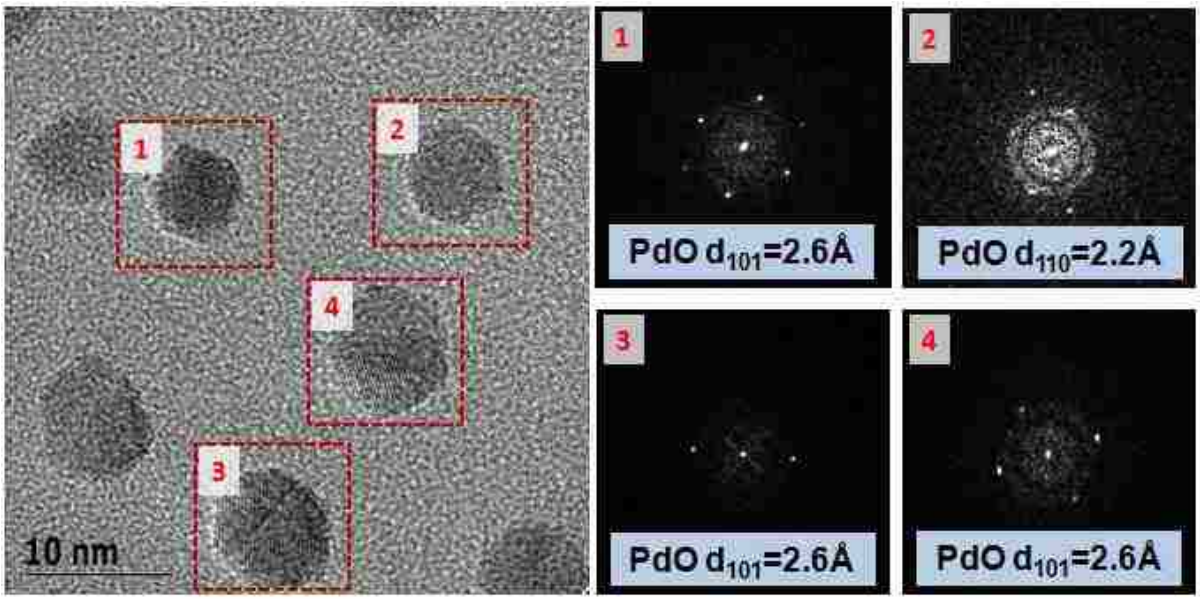

Figure 23. HR-TEM image of Pd/SiO_2 after aging at 800°C for 1.5 hr. The Pd sample has become oxidized. At a temperature of 800°C the PdO has not begun to decompose to metallic Pd. The lattice spacing of the particles shown is consistent with that of PdO.

Under elevated aging temperatures for 1.5 hr, Pt sinters and its emission to the vapor phase is dramatic. Under the same conditions, Pd sinters very little and does not show any emission, or loss. The next step was to determine what happens when Pt and Pd are alloyed. We found that Pd significantly decreases the vapor phase emission of Pt, and it slows down the rate of sintering in most cases. Figure 24 shows the aging progression and the corresponding loss of metal and increase in mean diameter for the bimetallic samples. 51 pm of metal were lost from the bimetallic sample when aged at 800°C for 1.5 hr. Of those 51 pm, 44 pm were Pt. Initially the composition of the samples was 38% Pt and 62% Pd, but after aging at 800°C for 1.5 hr the composition was 32% Pt and 68% Pd. The Pt sample aged under the same conditions lost 323 pm. By extrapolating we found that there would only be about 1 pm lost when the bimetallic sample was aged at 750°C for 2 min. Table 7 shows the characteristics of the bimetallic samples in their initial state as well as after the different aging treatments. In future work, we will explore what happens to $Pt\text{-}Pd/SiO_2$ when aged at 750°C for 1.5 hr to compare to the pure Pt sample. A mechanistic study was done for $Pt\text{-}Pd/SiO_2$ just like it was done for Pt/SiO_2, and it is described in Chapter 5. Figure 32 shows the results and the highlighted particles to show we had imaged the same area of the sample before and after aging. The sample was aged at 650°C for 15 s. Under these conditions there

is negligible emission to the vapor phase, but the nanoparticles sintered through Ostwald ripening. Particles with a small initial diameter tended to shrink while those with a larger initial diameter tended to grow. Since the particles before aging were already bimetallic, the fact that some particles shrank until they disappeared shows that both Pt and Pd must be mobile. If only Pt were mobile, Pt atoms would transfer through the vapor phase or along the surface of the support, leaving a Pd cluster behind. This Pd cluster would become oxidized during aging. This is not what we see, however. The particles remain bimetallic and some disappear during the ripening process, suggesting that both metals are mobile.

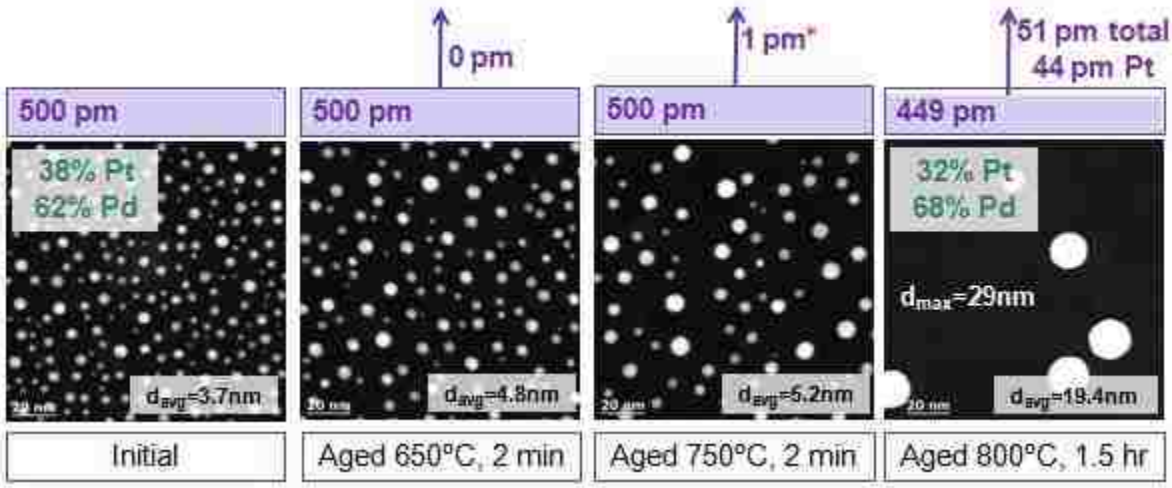

Figure 24. Effect of aging conditions on Pt-Pd sintering and emission in air. (* means estimated from extrapolation.)

Table 7. Characteristics of of Pt-Pd/SiO_2 in its initial state and after aging.

	Mean Diameter (nm)	Particles/μm²	Projected Area/Total Area
Pt-Pd/SiO_2 initial	3.7	13,600±300	0.16
Pt-Pd/SiO_2 Aged 650°C, 2min	4.8	7,000±1,000	0.13
Pt-Pd/SiO_2 Aged 750°C, 2min	5.2	4,530±80	0.11
Pt-Pd/SiO_2 Aged 800°C, 1.5hr	12.4	290±80	0.04

To compare the differences between the three types of samples (Pt/SiO_2, Pd/SiO_2, and $Pt\text{-}Pd/SiO_2$), Figure 25 shows the HAADF-STEM images of the samples before and after aging at 650°C in air for 2 min. The average diameters are provided. Pt has the most dramatic sintering, followed by Pt-Pd. The Pd sample becomes oxidized but shows no signs of sintering under these conditions. The corrected mean diameter of Pd is provided in Table 6.

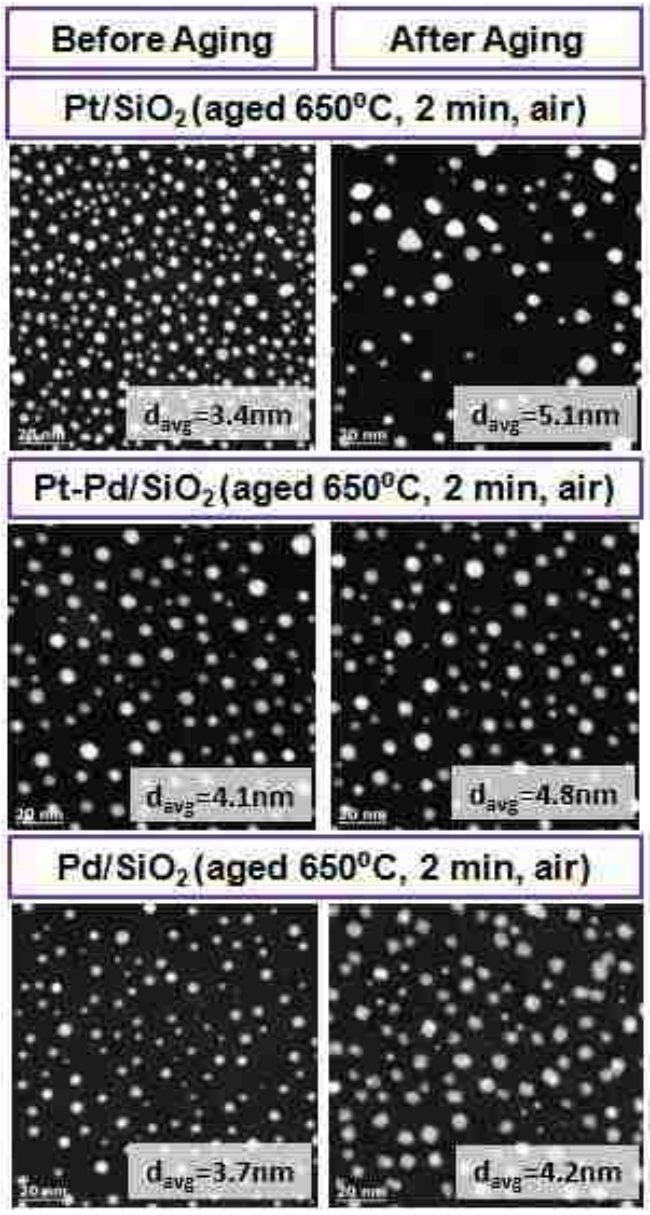

Figure 25. HAADF-STEM images of Pt/SiO_2, $Pt\text{-}Pd/SiO_2$, and Pd/SiO_2 before and after aging at 650°C in air for 2 min. The number average diameters are provided. Pt has the most dramatic sintering, followed by Pt-Pd. The Pd sample becomes oxidized but shows no signs of sintering under these conditions.

The results of Pt/SiO_2 and $Pt\text{-}Pd/SiO_2$ aged at 750°C for 2 min are shown in Figure 26. Pt nanoparticles sintered much faster at 750°C for 2 min than they did at 650°C. Again it appears that addition of Pd decreased the rate of sintering. Within the limits of experimental error (as shown earlier), we did not see any mass loss by EDS at 750°C when heated for 2 minutes.

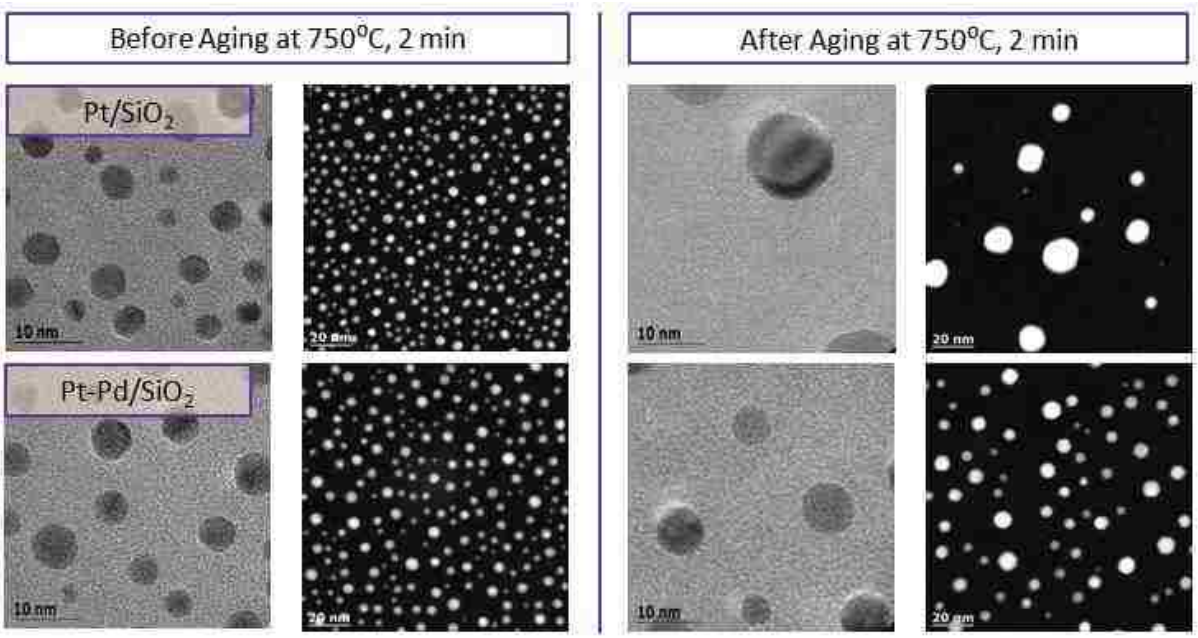

Figure 26. HAADF-STEM images of Pt/SiO_2 and $Pt\text{-}Pd/SiO_2$ before and after aging at 750°C in air for 2 min. Again, Pt sinters faster than Pt-Pd showing that the addition of Pd slows the ripening process under these conditions.

Figure 27 shows the HAADF-STEM images of the Pt, Pt-Pd, and Pd sample at 800°C for 1.5 hours in air. The maximum particle sizes for Pt and Pt-Pd were similar, but the largest Pd nanoparticle was only 8 nm. It is surprising that during aging at 800°C for 1.5 hr the Pt-Pd sample sintered more than the Pt sample. We repeated this measurement with a second sample to confirm the results and found this behavior to be fully reproducible. We can rationalize the behavior from the fact that the Pt sample experienced a 64.5% molar loss (323 pm of Pt) while the total molar loss on the bimetallic sample was only 10.2% (51 pm). Hence, the addition of Pd has decreased vapor phase emission much more significantly in this set of experiments.

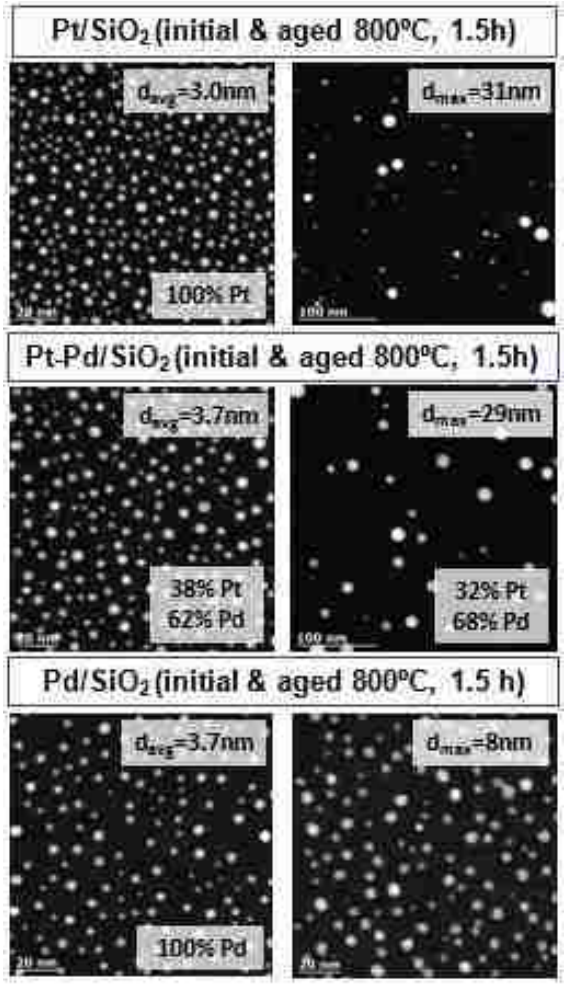

Figure 27. HAADF-STEM images of Pt, Pt-Pd, and Pd/SiO_2 before and after aging at 800°C for 1.5 hr. The mean diameters are provided for the catalysts in the initial state. The maximum particle size is provided for each sample after aging.

Why does Pd slow the emission of Pt? One possibility would be if there was a PdO shell surrounding the bimetallic nanoparticles; however, as shown in Figure 28, TEM shows that the surface of the bimetallic nanoparticles is metallic and not covered by a PdO shell. We confirmed this previously for supported Pt-Pd nanoparticles via HR-TEM and by EXAFS. [39] Some of the Pt-Pd particles phase segregate to form a PdO phase that is conjoined to the metallic Pt-Pd particle. But such particles are rare and we therefore do not think that such bi-phasic particles play a significant role in explaining the reduced emission of Pt. The morphology changes that the monometallic and bimetallic samples go through after oxidative aging are shown in Figure 29.

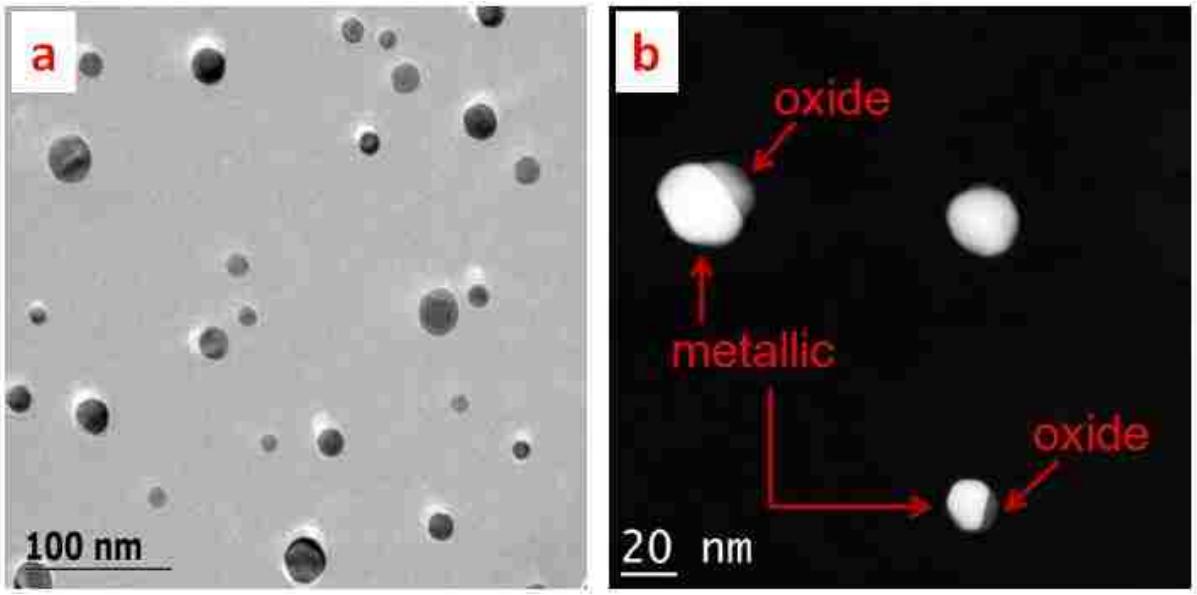

Figure 28. (a) TEM image of Pt-Pd/SiO_2 after aging at 800°C for 1.5 hr, showing the morphology of the nanoparticles. (b)HAADF-STEM image of Pt-Pd/SiO_2 after aging at 800°C for 1.5 hr, showing an oxide phase on a portion of two of the particles.

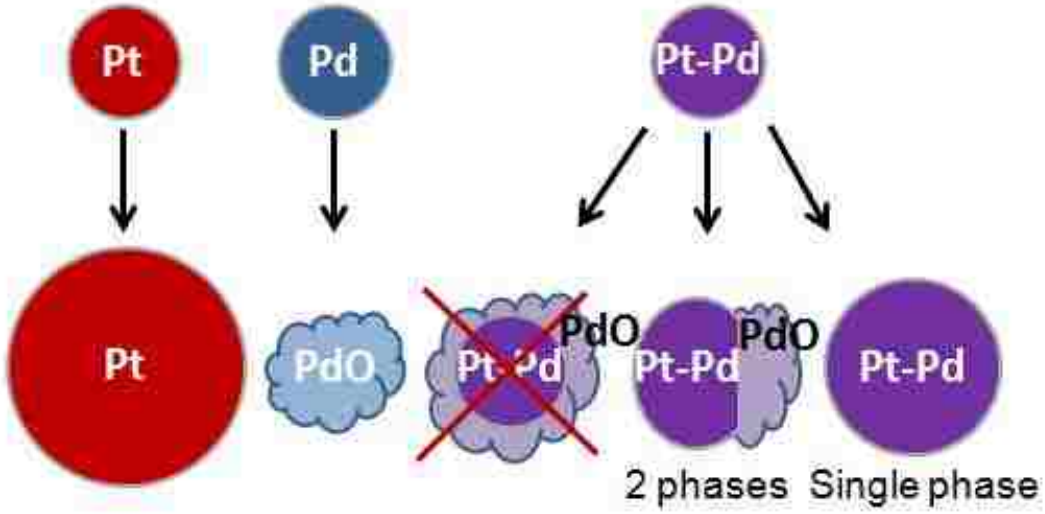

Figure 29. Schematic of morphology of particles after aging under oxidizing conditions.

Adding Pd clearly reduces the emission of Pt. Pd does not, however, slow the emission of Pt due to a PdO shell that blocks the emission. Instead, based on

thermodynamics, Pd slows the emission of Pt because of a dilution effect. It has been shown that Pt and Pd are miscible and exhibit only a small degree of non-ideality. For a 50% Pt – 50% Pd sample, one could expect almost a 50% decrease in vapor pressure. [34] The amount that Pd decreases emission of Pt in these experiments is consistent with this dilution effect.

In the case of Pt/SiO_2, the mobile species is PtO_2. PtO_2 can either migrate through the vapor phase or along the surface of the support. In the case of Pd/SiO_2, upon aging under oxidizing conditions, Pd becomes PdO and does not emit species to the vapor phase or the support. But what are the mobile species in bimetallic samples? An intriguing feature pertains to the composition of the nanoparticles after aging. Because we have shown that Pd forms an oxide that is not volatile and there is negligible loss of Pd during oxidative aging at 800°C, one would expect that after aging, the bimetallic particles would show phase segregation since Pt forms a mobile species but Pd does not. However, to our surprise we found that after aging at 800°C, the composition of individual nanoparticles was very similar to the initial composition of the sample before aging. The compositions were determined using spot EDS in STEM mode, and the compositions of several nanoparticles are shown in Figure 30. Therefore, despite the significant growth in particle size seen in the sample heated at 800°C, the compositions of the nanoparticles in the aged catalyst were nearly identical to those in the initial catalyst. These results suggest that both Pt and Pd species are mobile under oxidative conditions, leading to the observed sintering of the Pt-Pd catalyst, while the Pd only catalyst hardly sinters. We conclude then that Pt enhances the sintering of Pd in these bimetallic catalysts.

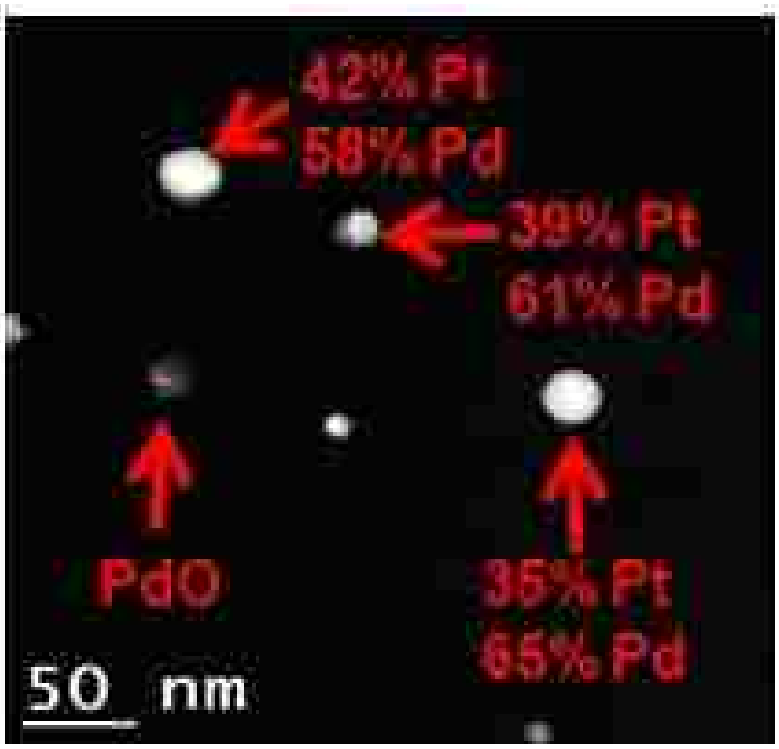

Figure 30. HAADF-STEM image of Pt-Pd/SiO_2 after aging at 800°C for 1.5 hr, showing the compositions of individual nanoparticles.

We can now summarize our key observations. (1) A volatile oxide of Pt forms upon heating in air, leading to emission of PtO_2 and loss of Pt on the surface of the catalyst. (2) Adding Pd slows down the emission of Pt, but not due to the formation of a shell of PdO, rather due simply to the dilution of Pt by Pd in the bimetallic. (3) Pd sinters very slowly in air, since the oxide PdO is quite non-volatile. (4) When Pd is present in metallic form in the bimetallic Pt-Pd nanoparticles, it sinters much more readily than the PdO in aged pure Pd catalysts. (5) Both Pt and Pd are mobile and once emitted their rates of surface diffusion must be similar since larger bimetallic nanoparticles retain the same composition as the initial particles, despite a significant growth in particle size. (6) The particle size distributions under conditions of vapor phase transport are very different, since we see bimodal size distributions with large faceted particles co-existing with very small particles (< 2nm) distributed over the support.

This work shows that emission of atoms from nanoparticles is the rate limiting step in Ostwald ripening, at least on the model catalysts where the nanoparticles are in close proximity. In the case of monometallic Pd, PdO forms very quickly and then we see negligible emission of atoms (or molecules) with the result that Pd catalysts are quite stable after heating in air. However, when Pd is present in the Pt-Pd alloy, then Pd atoms can be emitted as PdO, and they diffuse over the surface (just as PtO_2 does) and can form large Pt-Pd particles. This inference is consistent with detachment energies calculated using DFT by one of our collaborators (Boris Kiefer). The detachment energy for PdO to detach from a (111) bimetallic surface is 1.3 eV. It is 0.8 eV for PtO_2 to detach from that surface and then condense on the support. As oxygen reacts with Pt, we start to emit Pt in the form of PtO_2 and it can transport through the vapor phase (emission energies described below) and along the surface of the support. This leaves behind under-coordinated Pd since it has now lost its neighbors. Hence, this Pd is now easier to emit as an oxide and condense on the support. From DFT calculations, the detachment energy for PdO after one neighboring Pt atom has been emitted as PtO_2 (leaving Pd under-coordinated), is 1.0 eV. This is very similar to the 0.8 eV that is required for emission of PtO_2. This shows that it is almost equally facile for PdO and PtO_2 to get emitted from a bimetallic Pt-Pd nanoparticle, condense on the support, and sinter through surface diffusion. Therefore, Pt helps Pd emission. This is how Pt increases the sintering rate of Pd. The fact that the composition of the large particles is similar to that of the initial smaller particles suggests that both Pt and Pd are being emitted in proportion to their abundance in the initial catalyst and that their rates of surface diffusion are similar. Based on the DFT calculations for the detachment energies described above, this is very plausible.

Pt can exist as an oxide on the surface of the support as well as in the vapor phase. Under conditions of vapor phase transport, we see a bimodal particle size distribution. We infer that the small Pt particles (< 2 nm) are formed by condensation of the volatile Pt oxide when the sample is cooled. Vapor phase processes only become significant at elevated temperatures, which is expected since the activation energy for vapor phase emission is the heat of sublimation, while the emission of metal oxide species on the support involves a much lower barrier.

To gain insight into the energetics of atom emission to the vapor phase, our collaborator from New Mexico State University, Boris Kiefer, augmented our experiments with DFT calculations to explore atom emission energies (Table 8) from the monometallic phases (for computational details see Computational Method section below). The computations show that particle emissions without preadsorbed oxygen are endothermic as expected but more favorable as compared to the case with preadsorbed oxygen and the emission of reduced atoms (Table 8). These findings suggest that the surfaces remain metallic and that emitted Pd and Pt occur as oxidized species at least in the absence of oxidized nanoparticles consistent with our experiments. The calculations show that the emission of gas phase PdO is unlikely, but the emission of PtO_2 is very likely.

Table 8. Emission energies (eV) for the emission of PdO dimers and PtO_2 trimers from extended monometallic (hkl) surfaces. Emission energies were computed as

- No preadsorbed oxygen: $TM_{N-1}(hkl)+TMO_{2x}(g)-(TM_N+x\ O_2(g))$.
- Preadsorbed oxygen: $TM_{N-1}(hkl)+TMO_{2x}(g)-2x\ O/TM_N$.
- Reduced metallic species: $TM_{N-1}(hkl)+TM(g)-TM_N$.

where hkl is the Miller index of the extended surface, TM=Pt, Pd, N=64 for the (111) surface and N=72 for the (100) and (110) surfaces, and x=0.5 and x=1 for PdO and PtO_2, respectively. Molecules in the gas phase are labeled (g). Accordingly, positive emission energies correspond to endothermic processes. As expected all emission processes are activated.

	No pre-adsorbed oxygen		Pre-adsorbed oxygen		Reduced metal	
Emission energies (eV)	PdO	PtO_2	PdO	PtO_2	Pd	Pt
(111)	4.1	1.7	5.5	4.4	4.6	6.6
(100)	3.7	0.9	5.2	4.1	4.3	5.9
(110)	3.4	0.5	4.8	3.5	3.9	5.5

This work has studied the phenomena occurring when Pt, Pd, and Pt-Pd catalysts were aged in air at temperatures of up to 800°C. Pt sinters rapidly in air due to the formation of volatile PtO_2; however, Pd shows very little sintering due to the low vapor pressure of PdO at these temperatures. Addition of Pd slows the rate of Pt sintering, but Pd sinters much faster in the bimetallic catalyst; therefore, we come to the surprising conclusion that Pt enhances the rate of Pd sintering. The emission of volatile Pt oxides could be detected in our model catalyst samples since they are exposed to a flowing gas stream. Such metal emission would not be detectable in powder catalysts, as the majority of emitted atoms would be readsorbed in neighboring support particles. [40] We suggest that the mechanism by which

Pd enhances the thermal durability of Pt is via the decreased emission of metal atoms. The similar compositions of Pt-Pd after sintering suggest that both Pt and Pd are mobile. We speculate that the mobile species are the oxides of Pt and Pd, and DFT calculations support this hypothesis. We come to the striking conclusion that emission of a mobile species of Pd is possible from the Pt-Pd bimetallic but not from bulk PdO. This PdO species on the surface of the support is mobile leading to the observed sintering of the bimetallic nanoparticles. The surface of the Pt-Pd nanoparticles remains metallic, and we do not see the formation of a surface PdO; hence, the lower emission of Pt from bimetallic nanoparticles is caused by the dilution of Pt by Pd. The rate limiting step must therefore be the emission of atoms from the nanoparticles. This study provides the first direct evidence for the role of atom emission in Ostwald ripening. The Pt-Pd bimetallics remain metallic under oxidizing conditions, and we suggest that it is the presence of metallic Pd that accounts for the enhanced reactivity of these bimetallic catalysts. [39]

Computational Method

We augmented our experiments with first-principle calculations that are based on density-functional-theory [41] as implemented in the periodic structure software package VASP. [42-44] Electronic exchange and correlations were treated at the GGA level within the parameterization of Perdew and Wang. [45] The interactions between electrons and nuclei were described within the PAW formalism. [46, 47] The electronic configurations (core radii in atomic units, 1 a_B=0.529 Å, in parenthesis) were $5s^2 4p^6 3d^8$ (2.300 a_B), $5d^9 6s^1$ (2.500 a_B), $2s^2 2p^4$ (1.900 a_B), for Pd, Pt, and O, respectively. The Fermi-level was slightly broadened Gaussian broadening (σ=0.1 eV). All calculations were performed using a cutoff energy of E_{cut}=500 eV which was found to be sufficient to obtain converged results. The equilibrium fcc-Pd and fcc-Pt structures were computed in the conventional unit cell with the same energy cutoff and 16x16x16 k-point grid. The optimized fcc-lattice parameters are 3.956 Å and 3.985 Å for Pd and Pt, respectively. These lattice parameters compare favorably with experiments, Pd: 3.8907 Å and Pt: 3.9239 Å. [48] The extended (111) surface structures were derived from the computed bulk equilibrium lattice parameters. All slabs consisted of 4 layers and consisted of a total of 64 atoms for the (111) surface and 72 atoms for the (100) and (110) surfaces. Similar to previous work, the shape of the simulation cell and the atoms

in the lower two layers remained fixed at their equilibrium values while the top two layers were allowed to relax. [49, 50] The modeled slab and its periodic images perpendicular to the surface were separated by a 14 Å vacuum layer and residual artificial interactions were reduced by introducing a compensating dipole layer. [51, 52] Properties of the slabs were computed using a Γ-centered 3x3x1 k-point mesh. The energies of isolated PdO dimers, PtO_2 trimers, and O_2 were computed in an orthorhombic simulation cell of dimensions 10 Å x 11 Å x12 Å using a single k-point (Γ-point).

Experimental Methods

The high purity metals (99.999%) of both platinum and palladium used to fabricate these samples were purchased from Materion Corporation. The metals were deposited directly onto the 2 mm x 2 mm SiO_2 TEM grid surface using a 10kV Temescal electron beam evaporator. This high vacuum cryo-pumped system was pumped to a base pressure of $1x10^{-7}$ Torr prior to deposition. The film thickness was controlled by a quartz crystal microbalance (QCM), while the deposition rate was controlled to 0.03 Å/s. This system as configured is capable of controlling the film thickness to 0.1 Å. These noble metals are non-wetting on oxide surfaces so a continuous film is not formed during deposition at these very low loadings. All films were deposited to a value equivalent to 5 Å.

The TEM grids have a 200 μm x 200 μm silicon nitride membrane window with a thickness of 15 nm. [25] The top and bottom 3 nm have been formed into a surface oxide layer through calcination in air at 750°C for 24 hours.

The samples were reduced for 10 minutes in flowing 7% H_2/N_2 (140 sccm) in a SabreTube™ furnace created by Absolute Nano. The furnace allows for a 100°C/s heating rate over a 1 cm wide substrate. Temperatures up to 1000°C are possible with the SabreTube™. The short two-minute aging treatments were performed in the SabreTube in flowing air at 140 sccm. The 1.5 hour aging treatments were done in a quartz tube furnace in flowing air at 100 sccm due to limitations on that flow meter. The quartz tubes have an inner diameter of 2 cm. The ramp rate of the furnace was 20°C/min, and the temperature was held for 1.5 hours and then decreased to room temperature in the flowing air.

Transmission electron microscopy (TEM) as well as scanning transmission electron microscopy (STEM) images were taken both after reduction and after aging under oxidizing conditions. A JEOL 2010F 200kV FASTEM FEG (field emission gun) TEM/STEM was used to acquire all STEM images. This microscope has a point-to-point resolution of 0.194 nm and a minimum spot size in STEM mode of 0.14 nm. It has a GATAN GIF 2000 Energy Filter, JEOL bright and dark field STEM detectors, GATAN bright and dark field STEM detectors, and an Oxford Instruments ISIS/INCA energy dispersive x-ray spectroscopy (EDS) system with an Oxford Pentafet Ultrathin Window (UTW) Detector. EDS was used to obtain compositions as well as gather information on loss of metal.

Gatan Digital Micrograph was used for all image processing, and INCA was used for the analysis of all EDS data. Diameters of nanoparticles were determined by manual measurement within the Digital Micrograph software. To determine the loss of metal on each sample, either the ratios of the metal to silicon or the absolute counts of the metal were compared before and after aging in air at the specific temperature, as discussed previously in Chapter 2. This was done on an atomic percentage basis using the L lines of Pt and Pd.

Chapter 5

Detailed Mechanistic Study of Pt-Pd Nanoparticles During Aging Under Oxidizing Conditions

Approach

In automotive catalysts, the growth of nanoparticles can only be studied post-mortem, or after aging. We, therefore, developed a novel approach using model catalysts where it is possible to perform direct measurements of the emission of atoms from nanoparticles. The model catalysts we use allow heat treatment at elevated temperatures under realistic conditions and the opportunity to observe the same nanoparticle before and after treatment. Throughout this work, two different methods have been used. One is a statistical approach used to study thousands of nanoparticles and observe the overall phenomena (as discussed in Chapter 4). The second method involves a microscopic approach which can be used to track the behavior of individual nanoparticles.

Just like the previous model catalysts that were discussed, these were synthesized through electron beam evaporation. 5Å of Pt, 5Å of Pd, and a 5Å combination of Pt and Pd leading to a composition of 38% Pt and 62% Pd have been deposited onto SiO_2 TEM grids. These silicon-based TEM grids allow for high temperature aging. The samples were reduced in 6% H_2/Ar at 750°C. Aging was performed at 650°C in 21% O_2/Ar to simulate air. All reduction and aging treatments for the samples discussed in this chapter were performed in the SabreTube^{TM} furnace.

Our first objective was to use our new technique to prove that both Pt and Pt-Pd sinter through Ostwald ripening rather than coalescence. Previously Simonsen *et al.* [12] had studied Pt on a thin film of alumina using an environmental, or *in-situ*, TEM. They found that the nanoparticles with a smaller initial diameter tended to shrink, until some of them completely disappeared, while the particles with larger diameters tended to grow, indicative of Ostwald ripening. To our knowledge no such studies had been performed on bimetallic Pt-Pd catalysts. We used an *ex-situ* approach where we imaged the sample before aging, removed the sample from the microscope, did an aging experiment, put the sample back into

the microscope, and then could go back to the same area of the TEM grid where the original images were taken. We preferred this *ex-situ* approach so that the vapor phase processes could be studied as well as surface diffusion. *In-situ* TEM experiments are only possible at very low pressures where the vapor phase processes do not occur. It was possible to image the same area of the grid because of the type of TEM grids being used. There is only one electron transparent region on the grid in the shape of a square with dimensions of 200μm on each side. We noted the orientation of the grid when it was put in the TEM sample holder before the sample had been aged. Then, assuming it was placed in the sample holder in the same orientation after aging, we could go to the same corner of the electron transparent membrane and search for the exact particles which were imaged before aging. Because of the sintering that occurred during the aging treatments, the nanoparticles looked different than when they were first imaged. Particles had changed sizes and not all of the nanoparticles were present after aging, so it required a consistent technique to be able to find the same region of the sample. By using the SabreTube^{TM} it was possible to accurately age the samples for very short time intervals before the particles had changed so dramatically that it would not be possible to find the same particles after aging. This gave us the ability to study atom transfer processes between particles. Taking images after each aging experiment allowed us to obtain "snapshots" of the sintering progression at different times during the initial stages of the process.

Results

The experiment performed on Pt/SiO_2 and $Pt\text{-}Pd/SiO_2$ to investigate the sintering mechanism was aging at 650°C for 15 seconds in flowing 21% O_2/Ar. Figure 31 shows the TEM images of a Pt/SiO_2 model catalyst sample before and after aging at 650°C for 15 s. Individual particles and groups of particles are highlighted to make it easier to see the changes that have occurred. The average diameter of particles initially is 3.3 nm and the average after aging is 4.2 nm. Some of the particles have grown in size while others have decreased, indicative of Ostwald ripening. Some of the particles have completely disappeared. We confirmed that Pt/SiO_2 sinters through Ostwald ripening.

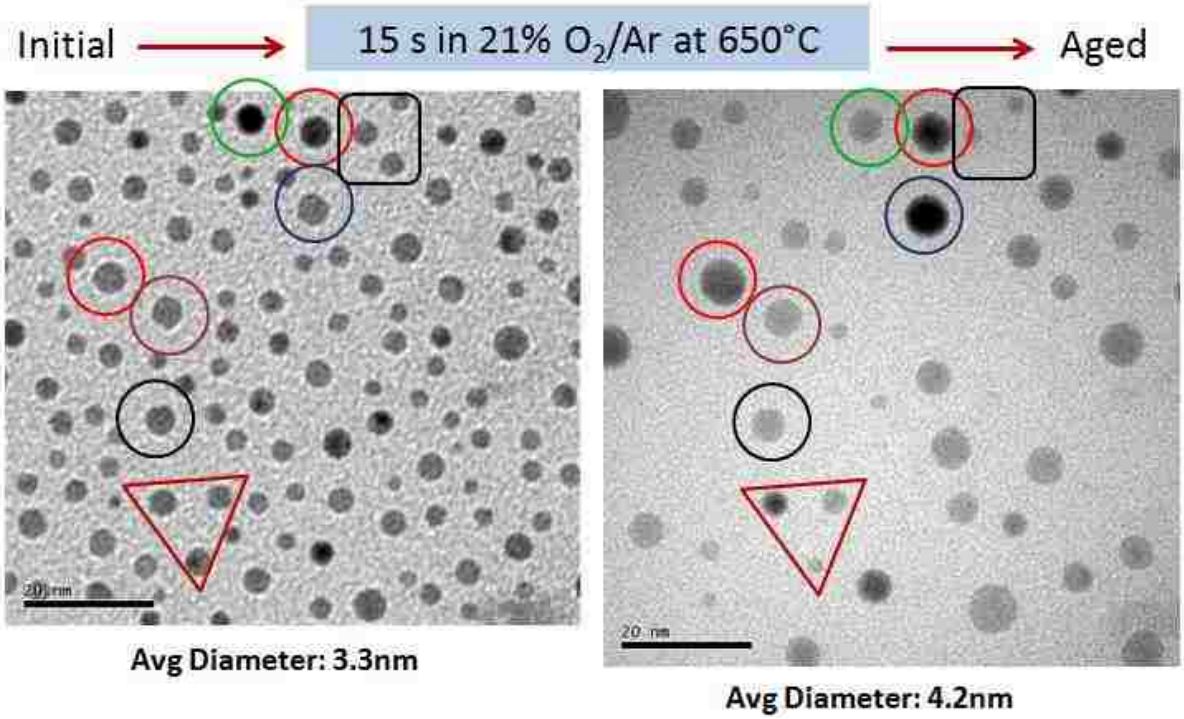

Figure 31. TEM images of Pt/SiO_2 before and after aging at 650°C for 15 s in 21% O_2/Ar. The same area of the sample is imaged in both pictures and individual particles or groups of particles have been highlighted so that the changes taking place can be more readily seen.

Figure 32 shows TEM images of the same area of a $Pt\text{-}Pd/SiO_2$ model catalyst before and after aging at 650°C for 15 s in 21% O_2/Ar. Again, some of the individual particles and groups of particles have been highlighted to make it easier to see the changes that are occurring. The average diameter of the particles before aging is 3.5 nm, and the average after aging is 3.9 nm. The particles are immobile, and just like on the Pt sample, sintering follows the Ostwald ripening mechanism. Some particles have grown while others have shrunk. Some of the nanoparticles completely disappeared. These results show that the bimetallic Pt-Pd nanoparticles sinter through Ostwald ripening on a flat SiO_2 support.

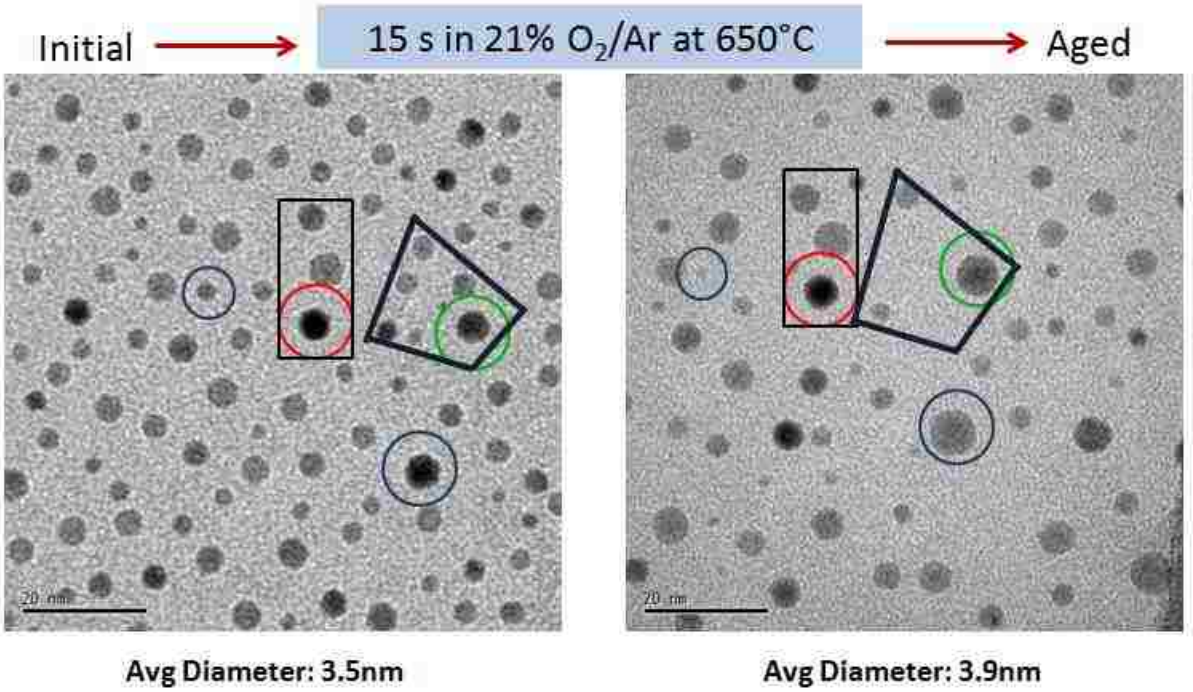

Figure 32. TEM images of a Pt-Pd/SiO_2 sample before and after aging at 650°C for 15 s in 21% O_2/Ar. Individual particles and groups of particles are highlighted to make it easier to see the changes taking place.

A set of samples was also aged in 30 second increments for up to a total of 2 minutes at 650°C. The total time-on-stream, therefore, was 30s, 60s, 90s, and 120s. These mechanistic studies were done at Eindhoven University of Technology (TU/e) in The Netherlands. Pt/SiO_2, Pt-Pd/SiO_2, and Pd/SiO_2 were all aged at the same time. After reduction and then between each aging step the three samples were imaged at the TEM. The aging series is shown for Pt, Pt-Pd, and Pd in Figures 33, 34, and 35, respectively. Within each figure, a plot showing the ratio of the final diameter to the initial diameter is provided for 30s, 60s, 90s, and 120s. The average diameter is shown for each sample during each step of the process. The Pt sample showed the most significant ripening under oxidizing conditions. The average diameter more than tripled over the two-minute aging period. It increased from 3.6 nm to 12 nm. The Pt-Pd model catalyst showed less significant ripening, with the mean size increasing from 3.7 nm to 9.9 nm. The Pd/SiO_2 sample showed the least amount of ripening. The average size of Pd nanoparticles increased from 5.1 nm to 9.7 nm. The increase in the size of Pd nanoparticles is generally due to the sample becoming oxidized. The nanoparticles in the TEM images of the Pd sample after 30s and 60s of aging

appear polycrystalline due to oxidation. Something unusual happened during the third 30-second aging interval, however. The image showing the time-on-stream of 90s has very round, metallic particles. The nanoparticles still have this appearance during the final aging sequence for a total time-on-stream of 120s. There are two possible explanations for this phenomenon. (1) Either the samples were subjected to a reducing atmosphere rather than an oxidizing atmosphere (containing H_2 instead of O_2) or (2) since the three samples were aged in the SabreTube^{TM} at the same time, it is possible that the volatile Pt species that was emitted then deposited on the Pd sample, causing round, metallic particles similar to those we see on the bimetallic Pt-Pd sample. This aging sequence should be repeated in future work to validate the results.

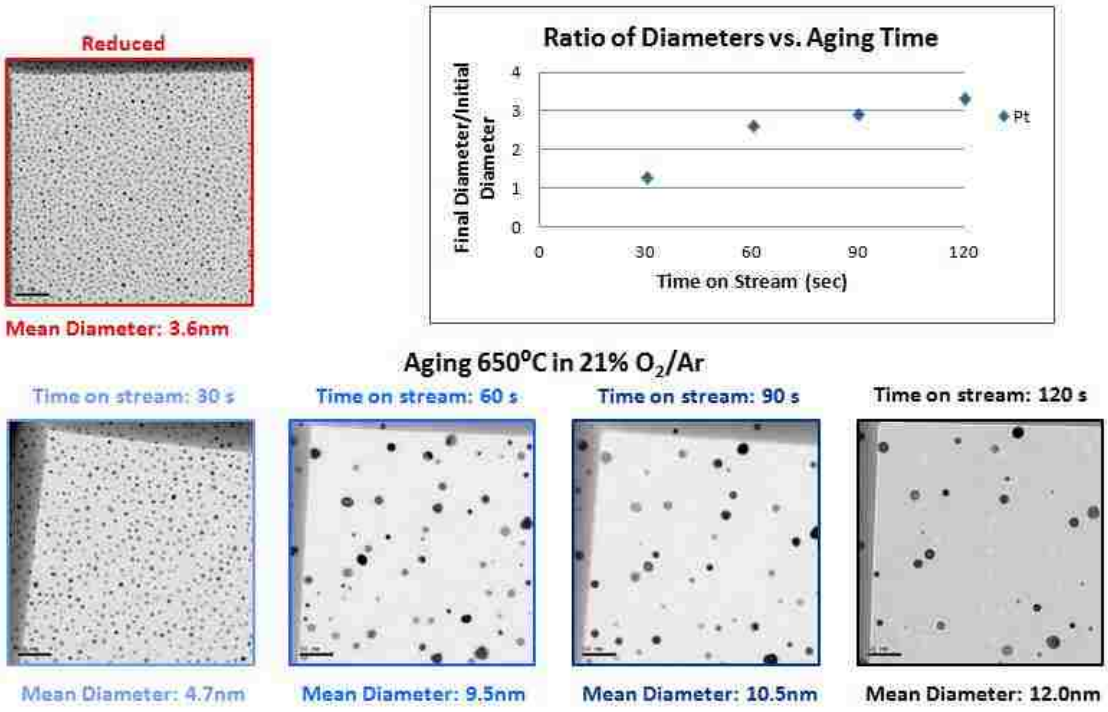

Figure 33. Aging sequence of Pt/SiO_2 showing the sample in its reduced state as well as after a total time-on-stream of 30s, 60s, 90s, and 120s at 650°C in 21% O_2/Ar to simulate air. The average diameters are provided during each step of the aging process. The mean size of Pt more than tripled over the two-minute aging treatment.

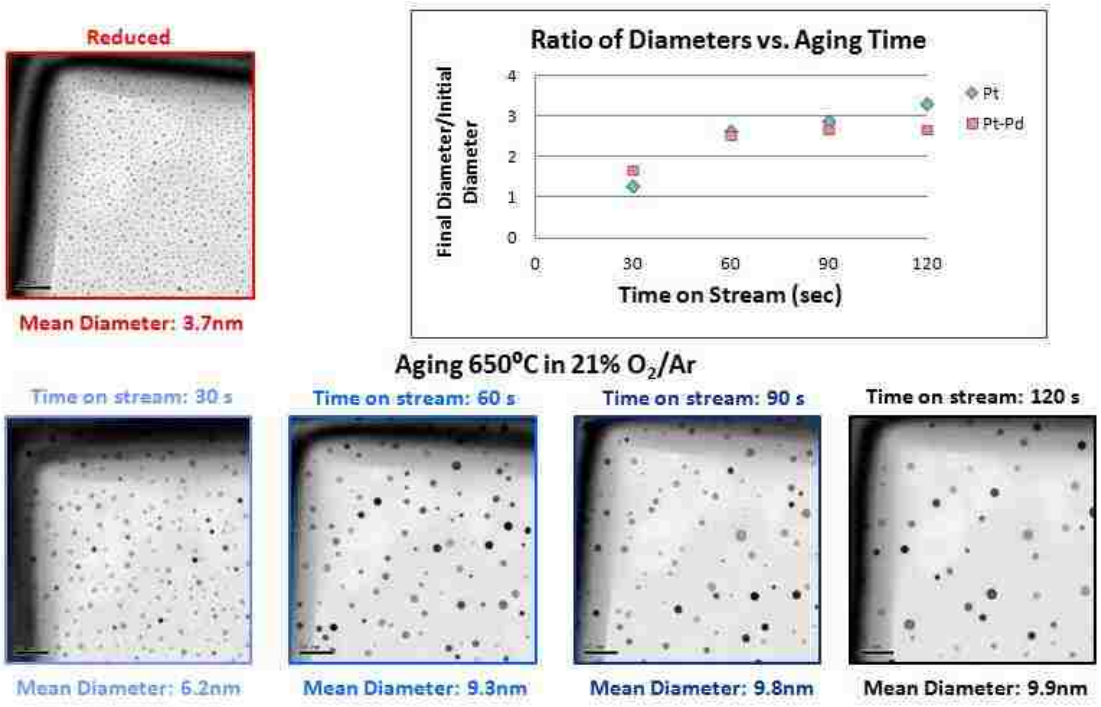

Figure 34. Aging sequence of Pt-Pd/SiO_2 showing the sample in its reduced state as well as after a total time-on-stream of 30s, 60s, 90s, and 120s at 650°C in 21% O_2/Ar to simulate air. The average diameters are provided during each step of the aging process. The mean diameter more than doubled.

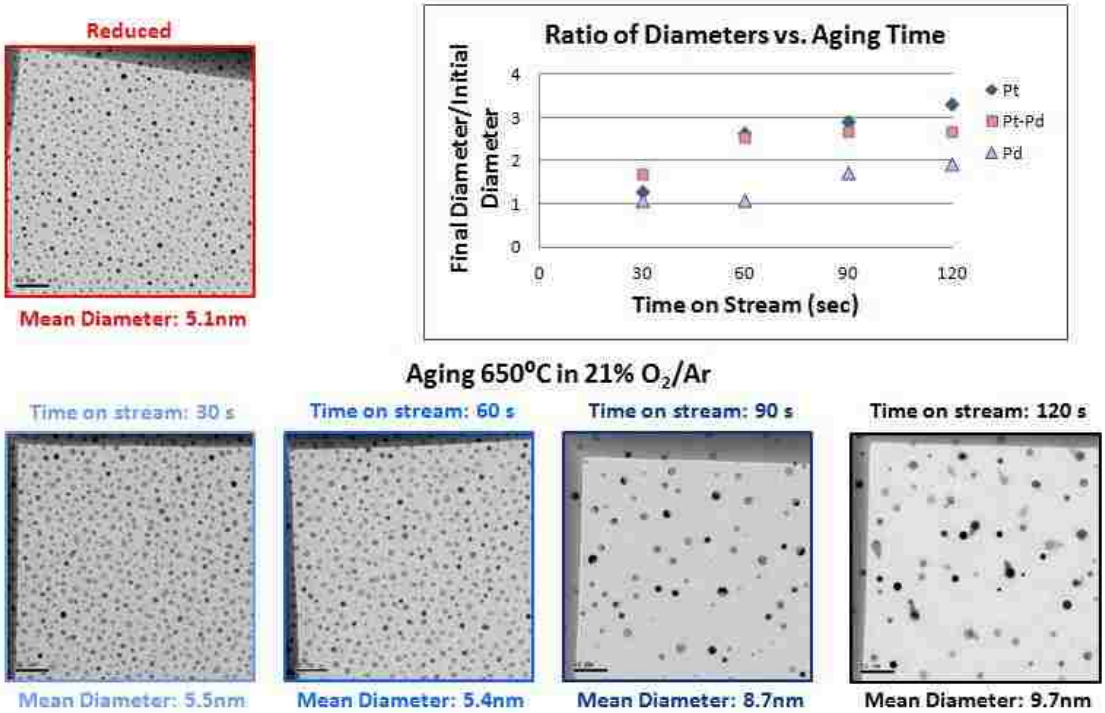

Figure 35. Aging sequence of Pd/SiO_2 showing the sample in its reduced state as well as after a total time-on-stream of 30s, 60s, 90s, and 120s at 650°C in 21% O_2/Ar to simulate air. The average diameters are provided during each step of the aging process.

The Pt and bimetallic Pt-Pd samples sintered more during the 2 minutes of aging at TU/e at 650°C than they did during the same aging treatment at UNM (discussed in Chapter 4). One difference is that the pressure is lower in Albuquerque than it is in Eindhoven. There is approximately a 20% higher O_2 pressure in Eindhoven (160 Torr versus 132 Torr in Albuquerque). The higher oxygen partial pressure would lead to higher rates of sintering due to the volatile PtO_2 species. Another possible explanation is that since the thermocouple on the SabreTube™ at TU/e was located in a different place than on our SabreTube™ in Albuquerque, the temperature of the samples at TU/e may have actually been higher than those at UNM. This would also lead to higher rates of ripening. A third contributor to this difference in sintering rate could very well be the fact that the samples were heated to 650°C four different times at TU/e while at UNM the two minutes of aging was done all at once. Every time the samples are resistively heated in the SabreTube™, there is a chance for experimental error. For example, as the temperature is ramped up to 650°C there is a chance for temperature overshoot. The errors are propagated through the 4 different aging treatments for these samples, and every time a new experiment is done there could be additional error which would cause higher rates of sintering. Since the samples had to be ramped up multiple times, there are a few extra seconds during each ramp where the sample may start sintering before it reaches 650°C.

Conclusions

These studies have shown that both Pt and Pt-Pd nanoparticles sinter through Ostwald ripening on thin film SiO_2 supports. During the detailed mechanistic studies of the three samples (Pt/SiO_2, $Pt\text{-}Pd/SiO_2$, and Pd/SiO_2) aged to a total time-on-stream of 120s, we see that Pt nanoparticles sinter the most, followed by Pt-Pd. The addition of Pd slows the rate of Ostwald ripening, and, conversely, Pt speeds up Pd sintering since Pd by itself hardly sinters. Pt-Pd when alloyed remains metallic even when aged under oxidizing conditions. In future work, the role of the support will be studied. A detailed mathematical model will be used to predict the rates of sintering and the rates of emission.

Chapter 6

Is Palladium a Textural or Chemical Promoter for Pt Diesel Oxidation Catalysts?

This chapter is based on work performed at General Motors Global R&D with the following co-authors:

Kim, C.H., Balogh, M.P., Oh, S., Johnson, J.T., Li, W., Wiebenga, M., Gaudet, J.R., Datye, A.K.

Abstract

A tighter regulatory environment combined with an increasing demand for clean energy has made low-temperature aftertreatment catalysts more attractive than ever. Specifically, diesel oxidation catalysts (DOC) which are used for hydrocarbon, carbon monoxide, and nitrogen oxide oxidation are being investigated. Platinum and palladium are the precious metals currently used in DOCs for the treatment of diesel engine exhaust. Previous studies have shown that self-assembled bimetallic Pt-Pd/Al_2O_3 catalysts are more active than their monometallic counterparts, but the reasons for this improved activity are not yet understood. The present work has examined the catalytic activity and kinetics of various monometallic as well as bimetallic catalysts aged under different conditions. NO oxidation in the presence of NO, O_2, and NO_2 was the probe reaction used to distinguish between the differing activities of Pt/Al_2O_3 and Pt-Pd/Al_2O_3. Characterization techniques such as transmission electron microscopy (TEM), energy dispersive X-ray spectroscopy (EDS), and inductively coupled plasma (ICP) spectroscopy have also been used to investigate the effect of palladium on platinum.

Significance

The challenges associated with diesel oxidation catalysts, such as the need to achieve low temperature light-off and the need for catalysts to be active at low temperatures, are what drove this research. It is important to investigate which catalytic properties make the diesel

oxidation catalysts most active. By understanding the synergistic effect of Pd with Pt, the synergy can be improved and there is a better chance of eventually replacing the expensive platinum group metals with something else.

The future work will involve understanding the improvement in hydrocarbon light-off temperature over bimetallic catalysts by using the knowledge gained from these NO oxidation probe reaction studies.

Introduction

Low-temperature aftertreatment catalysts have become very attractive in recent years due to the need to reduce greenhouse gas emissions to address global climate change concerns. Platinum (Pt) and palladium (Pd) are the precious metals currently used in diesel oxidation catalysts (DOCs) for hydrocarbon (HC), carbon monoxide (CO), and nitrogen oxide (NO) oxidation. Engines with a high fuel efficiency provide lower exhaust temperatures, so there is a need to achieve low light-off temperatures. The challenge is that the catalysts must be active at these low temperatures. CO and HC oxidation need to begin at temperatures below 200°C while minimizing Pt loading. Pd is added to Pt to improve the stability of these catalysts. What remains to be investigated is what catalytic property makes the diesel oxidation catalysts most active. What exactly is the role of Pd? Previous reports in the literature discuss the improved durability of bimetallic Pt-Pd catalysts over monometallic Pt catalysts. [5, 6, 8, 9] It is unclear in these reports, however, whether Pd acts as a textural or chemical promoter.

Previous work done by members of the Catalysts and Aftertreatment Systems in the Chemical and Materials Systems Lab at General Motors Global R&D has shown that self-assembly of Pt and Pd occurs after the monometallic catalysts are physically mixed and then aged in oxidizing conditions at elevated temperatures. Figure 36 (a) shows the physically mixed Pt/Al_2O_3 and Pd/Al_2O_3 and (b) shows the bimetallic sample after aging at 750°C for 72 hours. The Pd has segregated to the surface, and the particles are roughly 20 nm in size whereas in the as-prepared sample in (a) the average size was about 5 nm.

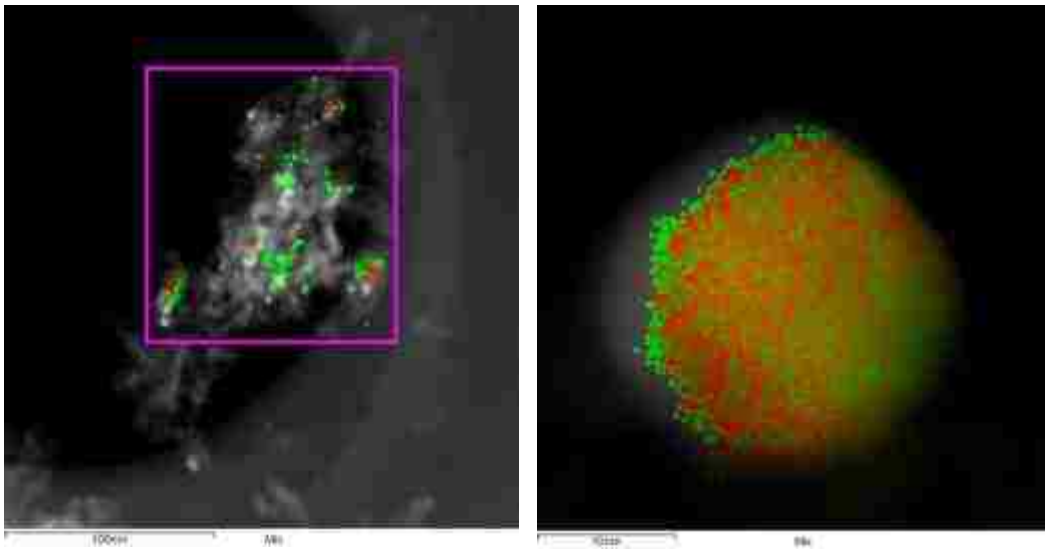

Figure 36. The physically mixed Pt/Al_2O_3 and Pd/Al_2O_3 in (a) the as prepared state and (b) after aging at 750°C for 72 hours (Pt red, Pd green).

The addition of Pd to Pt catalysts, in some cases, makes the catalysts more active. Figure 37 (a) and (b) show an improvement in light-off temperature of propylene for a physically-mixed bimetallic Pt-Pd sample after aging at 750°C. The bimetallic $Pt\text{-}Pd/Al_2O_3$ gives a significantly lower C_3H_6 light-off temperature than either of the monometallic catalysts when aged at 750°C.

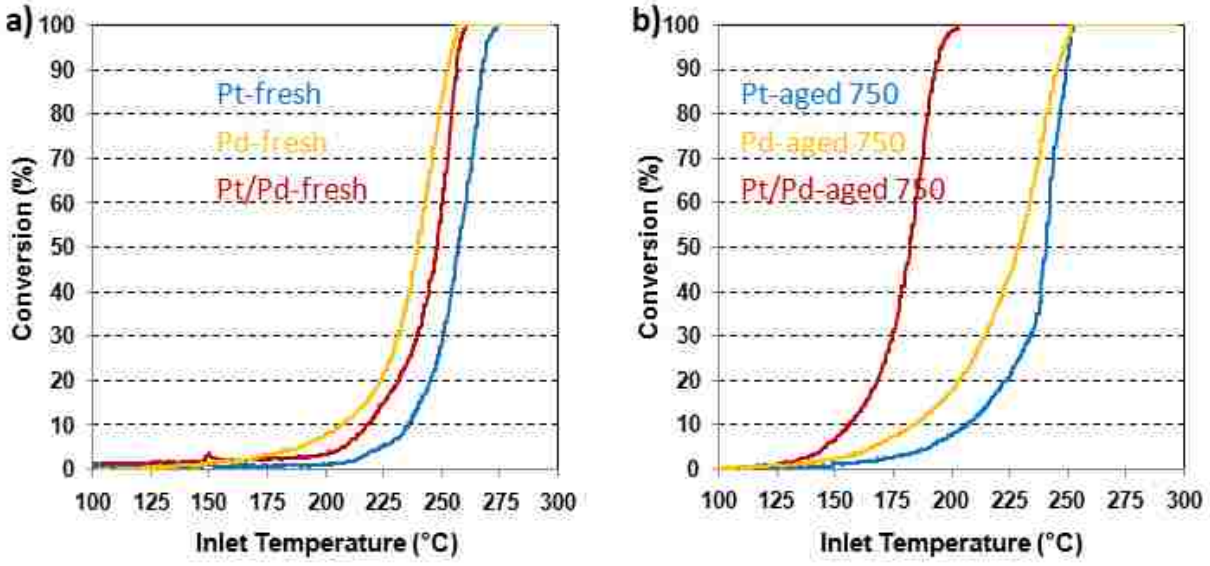

Figure 37. Propylene light-off temperature for Pt, Pd, and Pt-Pd catalysts in (a) fresh state and (b) after aging at 750°C. [Courtesy of General Motors Global R&D]

A Pt/Al_2O_3, Pd/Al_2O_3, and a bimetallic $Pt\text{-}Pd/Al_2O_3$ catalyst were compared in these experiments. In their fresh state, the three catalysts were fairly comparable; however, after aging, the alumina-supported bimetallic sample had a much improved light-off temperature than either of the monometallic samples. Before aging, the light-off temperature for the physically-mixed Pt-Pd catalyst was 248°C, but after aging, it had decreased to only 182°C. There is a need to understand why the catalytic reactivity is better on the bimetallic sample. Once the synergistic effect is understood, the synergy can be improved and possibly the expensive Pt group metals (PGMs) can eventually be replaced.

The previous observations showed improved hydrocarbon light-off performance. To determine the synergistic effect of Pt-Pd alloys, the active sites of monometallic Pt, Pd, and the alloy must be understood for oxidation reactions. Which sites become more active on the Pt-Pd alloy? NO oxidation is known to be active only over Pt catalysts, so this is the probe reaction chosen to investigate the change in catalytic properties of Pt. The Catalysts and Aftertreatment Systems group has done some experiments comparing the active sites of a Pt/Al_2O_3 and a bimetallic $Pt\text{-}Pd/Al_2O_3$ catalyst in their ability to convert NO to NO_2. Figure 38 (a) and (b) show the measurement protocol at 300°C for the catalysts initially in their fresh state.

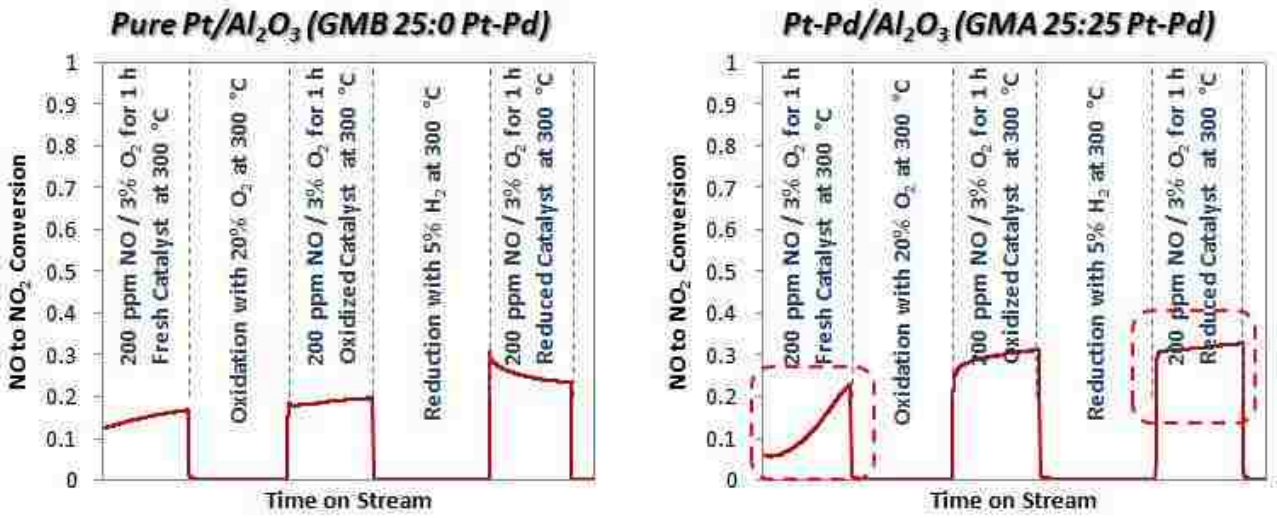

Figure 38 (a) and (b). Identification of active sites of Pt on (a) pure Pt/Al_2O_3 and (b) bimetallic $Pt\text{-}Pd/Al_2O_3$ catalysts. [Courtesy of General Motors Global R&D]

The two catalysts underwent the same treatments. First, they were exposed to 200 ppm of NO and 3% O_2 for 1 hour at 300°C. At this point, the bimetallic sample had reached

a higher conversion of NO to NO_2 than the pure Pt sample. Then, the reactor was purged with N_2 for 10 min. The next step was oxidation in 20% O_2 at 300°C for 1 hour followed by a N_2 purge for 10 min. Next, the oxidized catalysts were exposed to 200 ppm of NO and 3% O_2 for 1 hour at 300°C. The bimetallic catalyst had a 50% higher conversion than the pure Pt catalyst. There was a reduction in 5% H_2 at 300°C for 1 hour. The last step was NO oxidation on the reduced catalysts for 1 hour in 200 ppm of NO and 3% O_2 at 300°C. Again the conversion of the bimetallic sample was higher than that of the monometallic Pt sample. After the reduction step, the pure Pt appears to have become reoxidized which caused the reduced conversion. Pd may have kept Pt in the reduced state in the bimetallic sample which could explain how the conversion remained elevated during the final NO oxidation.

Extensive work has been performed investigating NO oxidation over Pt/Al_2O_3 catalysts, as documented in [53] and [11]; however, the effect of Pd on the catalytic activity of Pt in bimetallic alumina-supported catalysts is not known and is the focus of this work. The synergistic effect of Pt-Pd alloys needs to be investigated. It needs to be determined whether the Pt-Pd alloy follows a different mechanism than Pt or if there is some type of surface chemistry difference in the alloy. The following work investigates the difference in activation energy between monometallic Pt/Al_2O_3 and bimetallic $Pt\text{-}Pd/Al_2O_3$, which suggests that there is a difference in the surface chemistry of the two catalysts. The effect of NO_2 inhibition has also been studied.

Experimental

Catalyst Preparation

Monometallic Pt/Al_2O_3 and Pd/Al_2O_3 catalysts were synthesized using the incipient wetness technique. Chloroplatinic acid and palladium nitrate were the precursors used. They were introduced to a lanthanum-stabilized alumina support from Rhodia Catalysts (MI-386SP) after being diluted with water. These slurries were dried overnight in a fume hood. The next day they were crushed into fine powders using a mortar and pestle and dried at 135°C for 3 to 4 hours. Once the powders were dried, they were calcined at 500°C for 1 hr in ambient air.

The monometallic Pt/Al_2O_3 sample was milled with water and reagent grade acetic acid from JT Baker. The bimetallic sample was prepared by physically mixing the two monometallic catalysts and milling them with water and the reagent grade acetic acid. The monometallic and bimetallic samples were dried at 90°C to 100°C. According to inductively coupled plasma atomic emission spectroscopy (ICP-AES) the bimetallic sample contains 0.61 wt% Pd and 0.62 wt% Pt while the pure Pt sample contains 0.56 wt% Pt.

Catalyst Characterization

Inductively Coupled Plasma (ICP) Spectroscopy

Inductively Coupled Plasma (ICP) spectroscopy was the technique used to obtain elemental analysis of the monometallic and bimetallic catalyst samples. A Varian Vista Pro system which utilizes a radial view of the plasma was used. Pt and Pd concentrations were measured in the monometallic and bimetallic samples. The samples were not completely dissolved because Al_2O_3 is very intractable to dissolution by aqua regia. Instead, Pt and Pd were leached from the substrate and the resulting solution was analyzed by ICP-AES. 99.999% pure materials were used for the calibration solutions. The detection limit was 5 ppm. Pt and Pd weight percentages were found by averaging three atomic emission lines.

Transmission Electron Microscopy (TEM)

The transmission electron microscope (TEM) used for these studies is a JEOL JEM 2100F AC (aberration-corrected, specifically probe corrected). The microscope is configured for both traditional TEM as well as scanning TEM (STEM). Images for this work were taken using a high angle annular dark field (HAADF) detector. The electron source on this microscope is a field emission gun (FEG), and the microscope is equipped with a STEM mode spherical aberration corrector (Cs). The 2100F has a TEM point resolution of 2.3Å and a lattice resolution of 1Å. In STEM mode, a resolution of 1.4Å is possible. The microscope also has an energy dispersive X-ray spectrometer (EDS) which provided the compositions of the bimetallic nanoparticles in this work.

Results and Discussion

The present work has examined the catalytic activity of various monometallic and bimetallic catalysts aged under different conditions that are representative of the environments catalysts undergo in vehicles. The authors examined two Pt/Al_2O_3 samples, one which was initially fresh and then aged at 300°C for 4 hours in baseline conditions (288 ppm NO, 175 ppm NO_2, 10% O_2, balance N_2) and one which was aged at 750°C for 2 hours in air and 10% H_2O. Two alloy samples were also investigated. One $Pt\text{-}Pd/Al_2O_3$ sample was initially fresh and then aged at 300°C for 4 hours in baseline conditions (288 ppm NO, 175 ppm NO_2, 10% O_2, balance N_2) and one was aged at 750°C for 2 hours in air and 10% H_2O. Throughout the paper the samples which were initially in the fresh state and then aged at 300°C will be referred to as Pt/Al_2O_3 or Pt-Pd/Al$_2$O3 aged 300°C, and the samples aged at 750°C will be referred to as Pt/Al_2O_3 or $Pt\text{-}Pd/Al_2O_3$ aged 750°C. Both of the 750°C aged samples had pretreatments at 500°C for 2 hours in 20% O_2/N_2 before conducting any experiments.

First, the apparent activation energies over the Pt and Pt-Pd catalysts were investigated. Arrhenius experiments provided conversion information and activation energy. The amount of catalyst, overall inlet flowrate, and temperature were adjusted to maintain the conversion below 15% to minimize mass diffusion limitations. From these experiments, the intrinsic rate was calculated. The forward rate plotted versus 1,000 divided by temperature is plotted in Figure 39, where $\beta = \frac{[NO_2]}{K[NO][O_2]^{1/2}}$. The Pt/Al_2O_3 aged 750°C sample was the most active and had an activation energy of 80 ± 12 kJ/mol. The bimetallic catalyst aged at 750°C had an activation energy of 86 ± 14 kJ/mol and the bimetallic sample aged at 300°C had an activation energy of 85 ± 17 kJ/mol. These energies were very similar, but the Pt catalyst aged at 300°C had the lowest activity and the highest activation energy of 95 ± 50 kJ/mol.

Pt was found to be far more active when aged at 750°C than at 300°C, which was also shown by the difference in activation energy. This is due to larger, faceted, metallic Pt particles on the sample aged under oxidizing conditions at 750°C, as shown in the following

section of this report. Pt/Al_2O_3 was found to be more active than $Pt\text{-}Pd/Al_2O_3$ when aged at 750°C, but the bimetallic catalyst aged at 300°C was more active than the pure Pt sample aged at 300°C. Pd only enhanced activity on the sample aged at 300°C.

The plot in Figure 39 has not yet had the rate normalized per site of Pt. STEM imaging provided information about the dispersion on each catalyst.

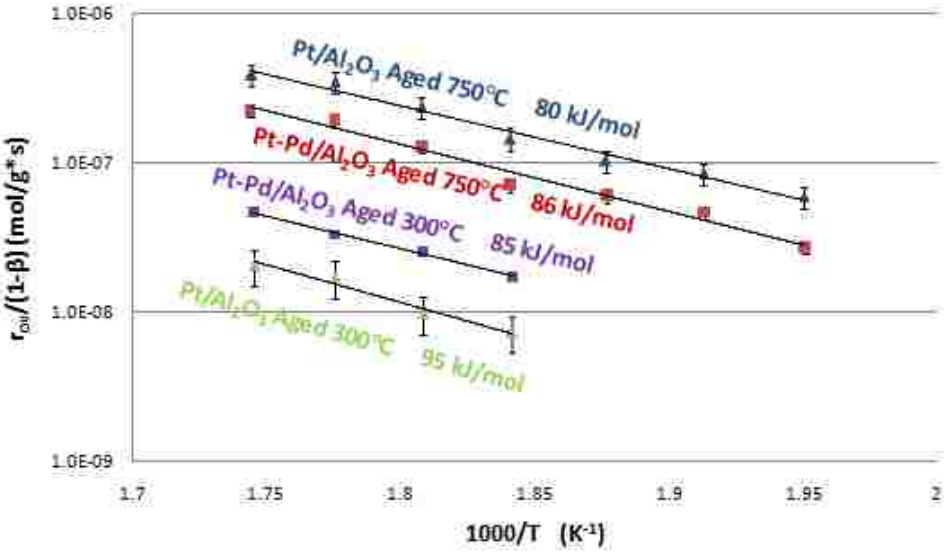

Figure 39. Arrhenius Plot for NO Oxidation Over Pt/Al_2O_3 and $Pt\text{-}Pd/Al_2O_3$ Aged at 300°C and 750°C.

STEM Results

Scanning transmission electron microscopy (STEM) was used in combination with energy dispersive X-ray spectroscopy (EDS) to determine some of the characteristics of the catalysts. The Pt nanoparticles were very difficult to find on the Pt/Al_2O_3 aged 300°C sample. This is most likely because Pt is atomically dispersed on the support. This highly dispersed Pt is not active for NO oxidation, however, because larger, faceted, metallic Pt nanoparticles are needed. Eventually, larger metallic particles would form on this sample, but at 300°C in baseline conditions for 4 hours, not many had formed. On the pure Pt sample aged at 750°C, the average size of Pt nanoparticles was 14.4 nm. Figure 40 compares some of the high-angle annular dark field HAADF-STEM images for both of the platinum catalysts. Figure 40 (a) and (b) shows two rare instances where we found large particles. There were very few particles found on the support, which is why we believe most of the Pt

was atomically dispersed on the support as an oxide.

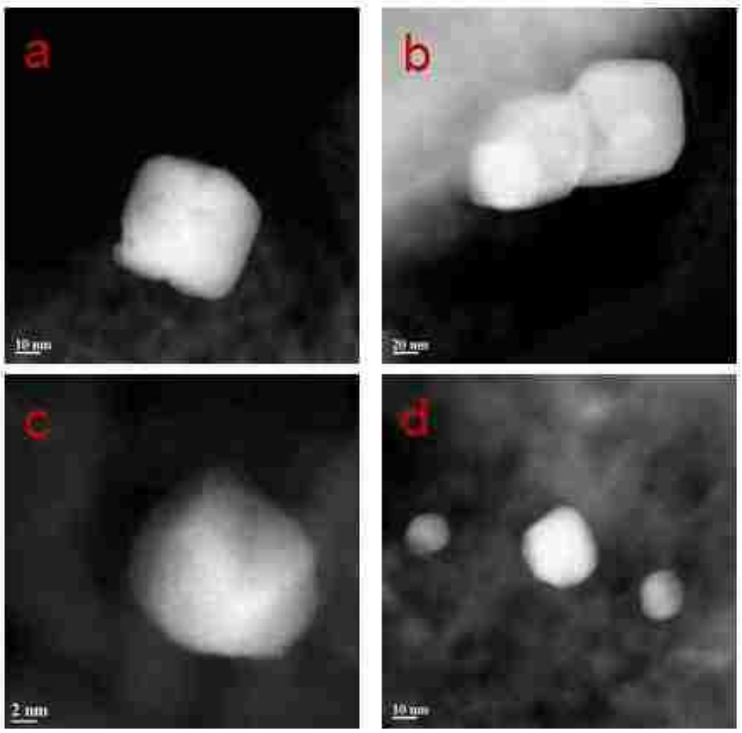

Figure 40. HAADF-STEM images of (a, b) Pt/Al_2O_3 aged at 300°C and (c, d) Pt/Al_2O_3 aged at 750°C.

Pt-Pd/Al_2O_3 aged at 300°C had many small nanoparticles so the average size was lower than on the other samples. This catalyst most likely also has a highly dispersed phase because it was difficult to find metallic nanoparticles. It was discovered that a small amount of Pd was already alloyed with Pt in the larger nanoparticles, as shown in Figure 41. The synergistic effect was only beginning at 300°C. A highly dispersed palladium oxide phase could account for the rest of the mass of Pd on this catalyst. The Pt-Pd/Al_2O_3 aged 750°C catalyst had alloyed metallic nanoparticles with an oxide phase covering a portion of the particle. This can be seen in Figure 42. The average size of nanoparticles on the Pt-Pd/Al_2O_3 aged 750°C sample was 24.8 nm. Figure 43 compares the particle size distributions for the Pt sample aged at 750°C and the Pt-Pd sample aged at 750°C.

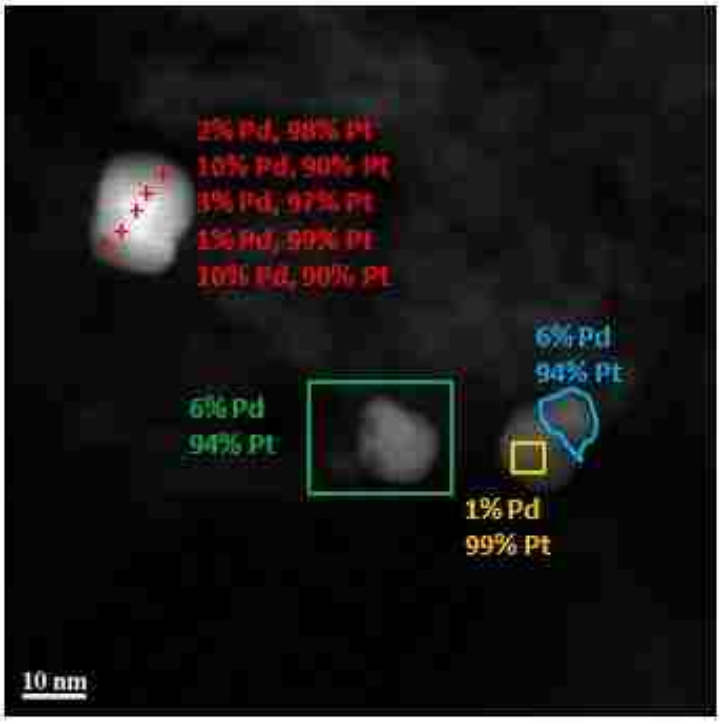

Figure 41. HAADF-STEM image of Pt-Pd/Al_2O_3 aged at 300°C with compositions determined from EDS.

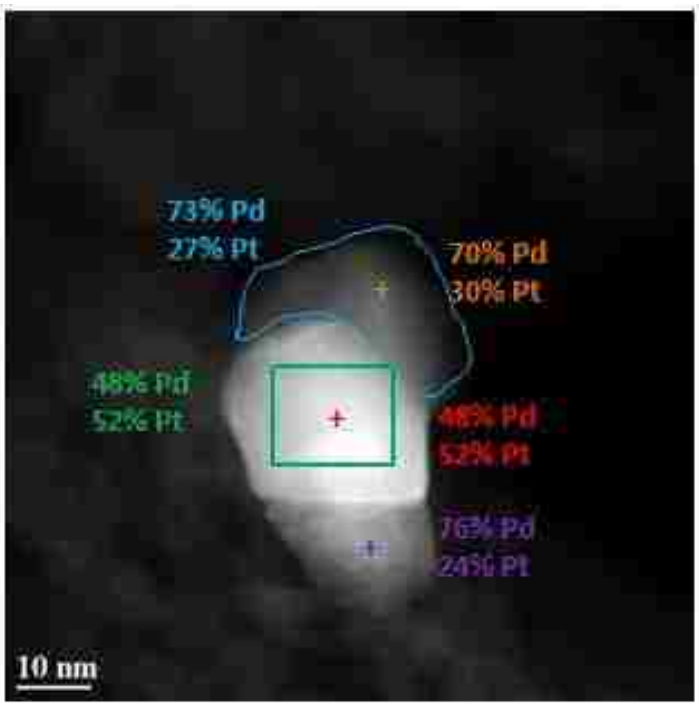

Figure 42. HAADF-STEM image of Pt-Pd/Al_2O_3 aged at 750°C with compositions determined from EDS. These nanoparticles contained a Pd-rich oxide region.

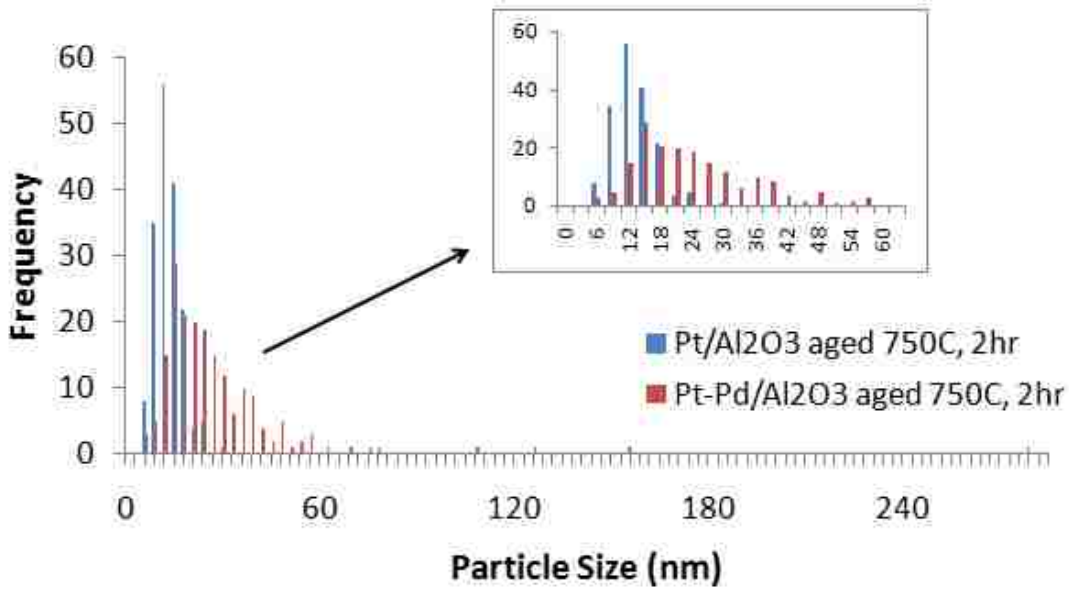

Figure 43. Particle size distributions for alumina-supported Pt and Pt-Pd catalysts aged at 750°C, as determined from STEM analysis. Inset is the portion of the distribution from 0 to 60 nm.

Figure 43 is different from previous results in the literature. [5, 6, 8, 9] Previous reports show that the addition of Pd stabilizes the catalysts by reducing the amount of particle sintering. The difference could be due to different preparation methods or different aging environments. For example, the previous work was not performed on physically mixed bimetallic catalysts.

The dispersions for all catalysts except the Pt/Al_2O_3 aged 300°C could be calculated from the average particle size found using EDS. For the pure Pt sample aged at 300°C, CO chemisorption was used because the average particle size could not be determined due to the highly dispersed species not visible on the TEM. CO chemisorption was also performed on the other three catalysts for comparison purposes. As shown in Table 9 below, the dispersion from CO chemisorption on Pt/Al_2O_3 aged 750°C matched very well with the dispersion calculated from the average particle size from STEM, so it was determined that CO chemisorption would be the best way to determine dispersion for the Pt/Al_2O_3 aged 300°C catalyst. From dispersion, turnover frequency was calculated. Since CO chemisorption takes into account both the Pt sites and the Pd sites, this was corrected for by multiplying the dispersion by the actual weight loading of Pt on each sample. Figure 44 shows the turnover frequency plotted versus 1000 divided by temperature. The rate has been corrected per site

of Pt since Pt is known to be the active species for NO oxidation. After normalizing with the dispersion, the catalysts aged at 750°C show comparable activity per site. There is a significant difference, however, between the samples aged at 300°C. The addition of Pd has improved the activity of the catalyst when aged at 300°C. This is likely due to the physical mixture of Pt and Pd catalysts already becoming alloyed and forming metallic, faceted particles.

Table 9. Dispersions Calculated from Average Nanoparticle (NP) Size and CO Chemisorption.

Catalyst	Average Particle Size (nm)	Dispersion from Average NP Size	Dispersion from CO Chemisorption
Pt/Al_2O_3 aged 300°C	--	--	38%
Pt/Al_2O_3 aged 750°C	14.4	10%	12%
$Pt\text{-}Pd/Al_2O_3$ aged 300°C	7.5	18%	22%
$Pt\text{-}Pd/Al_2O_3$ aged 750°C	24.8	6%	16%

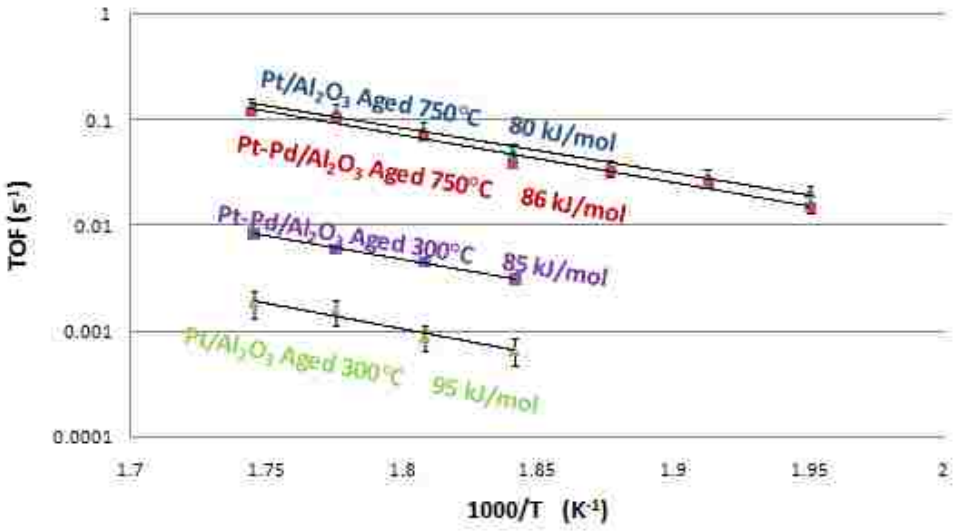

Figure 44. Turnover frequency for Pt/Al_2O_3 and $Pt\text{-}Pd/Al_2O_3$ aged 750°C and Pt/Al_2O_3 and $Pt\text{-}Pd/Al_2O_3$ aged 300°C.

Kinetics experiments were needed to determine the reaction orders for the catalysts. In the kinetics experiments, concentrations were varied one-at-a-time for NO while keeping NO_2 and O_2 constant, then for NO_2 while keeping NO and O_2 constant, and finally for O_2

while keeping NO and NO_2 constant. The NO concentration was varied around the baseline condition for the Arrhenius experiments (288 ppm) from 163 ppm to 360 ppm. The NO_2 concentration was varied around the baseline of 175 ppm from 153 ppm to 233 ppm. The O_2 concentration was varied around the baseline of 10% from 5% to 25%. The plot of the natural log of the forward rate versus the natural log of the concentration for Pt/Al_2O_3 aged 300°C is shown in Figure 45 for NO and NO_2 in (a) and for O_2 in (b). Table 10 provides the NO, O_2, and NO_2 reaction orders for the catalysts. The orders were very similar for NO and also for O_2 across the four catalysts, but the NO_2 orders varied more significantly. Figure 46 shows the plot of the natural log of the forward rate versus the natural log of NO_2 concentration for the different samples. Pt/Al_2O_3 aged 300°C has the lowest reaction order for NO_2 which implies that NO_2 inhibition is the most significant on this catalyst. The effect of NO_2 inhibition appears to be less severe with the addition of Pd.

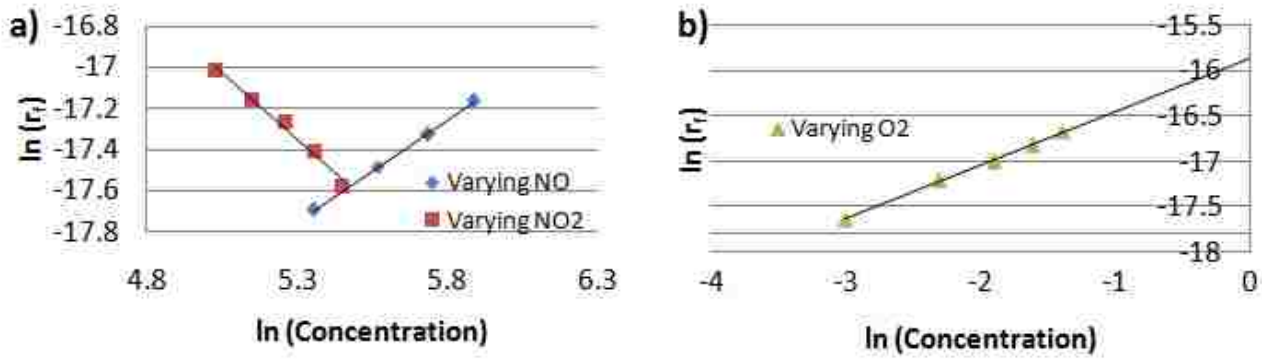

Figure 45. Plot of ln(rate) vs. ln(concentration) for varying (a) NO and NO_2 and (b) O_2 on Pt/Al_2O_3 aged 300°C.

Table 10. Reaction Orders.

Catalyst	NO order	O_2 Order	NO_2 Order
Pt/Al_2O_3 aged 300°C	0.99±0.08	0.59±0.04	-1.31±0.30
Pt/Al_2O_3 aged 750°C	0.80±0.12	0.63±0.10	-0.74±0.03
$Pt\text{-}Pd/Al_2O_3$ aged 300°C	0.98±0.10	0.58±0.04	-1.02±0.13
$Pt\text{-}Pd/Al_2O_3$ aged 750°C	0.70±0.14	0.55±0.04	-0.81±0.19

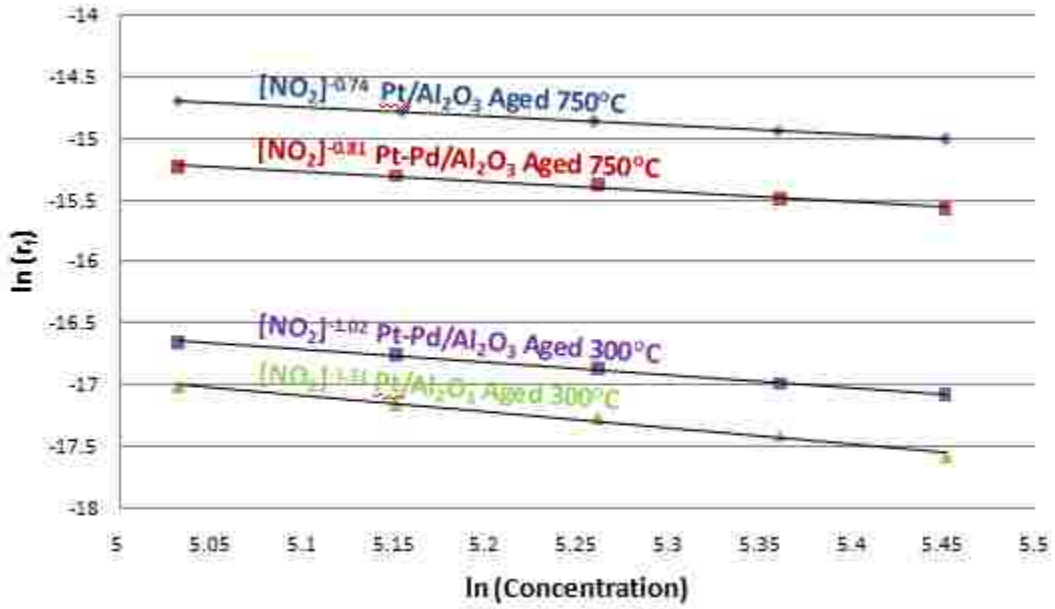

Figure 46. Comparison of NO_2 reaction orders.

Summary

From the current study, it was found that Pt/Al_2O_3 is far more active when aged at 750°C than at 300°C, as shown by the difference in activation energy. Upon aging at 300°C, much of the Pt is likely atomically dispersed on the support in the oxidized phase rather than in the form of metallic nanoparticles. Once aged at 750°C, the catalyst is far more active due to the larger metallic, faceted nanoparticles. It was also determined that $Pt\text{-}Pd/Al_2O_3$ is more active than Pt/Al_2O_3 when aged at 300°C because we start to see the onset of the formation of large, faceted metallic particles.

Pt/Al_2O_3 aged 300°C has the lowest NO_2 reaction order which implies that NO_2 inhibition is significant. This was confirmed by the Arrhenius plot and its corresponding activation energy. The addition of Pd to Pt changes both the apparent activation energy and the NO_2 reaction order due to the formation of larger, faceted metallic particles. We do not see a shell of PdO which covers the particles; hence, there is no negative effect of Pd on NO oxidation. The effect of NO_2 inhibition appears to be less severe with the addition of Pd.

Finally, the addition of Pd did not seem to improve the stability of the catalyst, but instead Pd seems to act as an inert. The STEM images and corresponding particle size

distributions suggest that Pd is not a textural promoter. When the bimetallic sample is aged at 750°C, the mean particle size of Pt-Pd/Al_2O_3 is larger than that of the Pt/Al_2O_3 aged 750°C.

Acknowledgements

We would like to graciously acknowledge the NSF GOALI CBET-106780. We would also like to thank Nick Irish for providing the ICP-AES analysis.

Chapter 7

Summary, Conclusions, and Future Work

This work began because of the desire to gain a fundamental insight into how Pd modifies the catalytic behavior of Pt. Previous work proved that Pd does indeed enhance the properties of Pt, but the mechanisms of how this occurs were not well understood. The work took part in three main phases. First, the microstructure of conventional powder monometallic Pt and Pd and bimetallic Pt-Pd catalysts was explored in the catalysts' working state. After 10 hours of aging at 750°C, EXAFS and XANES showed that in the bimetallics Pt is fully reduced but almost 30% of the Pd is present as an oxide. HR-TEM images show no evidence for a surface oxide on the metallic Pt-Pd particles, but instead PdO is present as a separate phase dispersed on the alumina support. Within the metallic particles, Pt and Pd are uniformly distributed, and we do not see evidence for core-shell structures. We propose that the improved catalytic performance is likely associated with the co-existence of metallic Pt and Pd on the catalyst surface. We also conclude that after aging at 750°C in air for 10 hours the improvement in durability from the addition of Pd was not significant.

Phase two involved the exploration of model Pt, Pd, and Pt-Pd catalysts to study the processes of Ostwald ripening. A statistical approach as well as a microscopic approach were used. By using flat model catalysts, it was possible to study the emission process as well as surface diffusion and the relative rates at different temperatures for different lengths of time. We confirmed that Pt and Pt-Pd sinter through Ostwald ripening when aged on a flat SiO_2 surface. This work has studied the phenomena occurring when Pt, Pd, and Pt-Pd catalysts were aged in air at temperatures of up to 800°C. Pt sinters rapidly in air due to the volatile species; however, Pd shows very little sintering due to the low vapor pressure of PdO at these temperatures. Addition of Pd in the alloys slows the rate of Pt sintering, but the Pd species sinters much faster in the bimetallic catalyst; therefore, we come to the surprising conclusion that Pt enhances the rate of sintering of Pd. DFT calculations supported this conclusion. We suggest that the mechanism by which Pd enhances the thermal durability of Pt is via the decreased emission of metal atoms. The similar compositions of Pt-Pd after sintering suggest that both Pt and Pd are mobile. The mobile species are likely the oxides of

Pt and Pd. We come to the striking conclusion that emission of a mobile species of Pd is possible from the bimetallic catalysts but not from bulk PdO. In surface diffusion, the role of Pd is not significant and we do not see a big improvement in stability. Surface diffusion is much faster than vapor phase processes at lower temperatures. At high temperatures, vapor phase transport becomes very important. Pd slows down the vapor phase processes and makes a big improvement in the catalysts. Vapor phase processes become dominant at high temperatures and lead to the formation of anomalously large particles, but Pd prevents these large particles. The surface of the Pt-Pd nanoparticles remains metallic just as it did in the powder catalyst studies, and we do not see the formation of a surface PdO. Therefore, the lower emission of Pt from bimetallic nanoparticles is caused by the dilution of Pt by Pd. The rate limiting step must be the emission of atoms from the nanoparticles.

In the third phase of this work we investigated the effect of Pd on the catalytic activity of Pt in the physically mixed and aged bimetallic alumina-supported catalysts. We studied the difference in activation energy between monometallic Pt/Al_2O_3 and bimetallic $Pt-Pd/Al_2O_3$. It was determined that when aged at 300°C, $Pt-Pd/Al_2O_3$ is more active than Pt/Al_2O_3 due to the onset of the formation of large, faceted metallic particles. Both catalysts were far more active when aged at 750°C than at 300°C, as shown by the difference in activation energy. This is due to the particles becoming larger, metallic, and faceted. Pt/Al_2O_3 aged at 300°C has the most negative NO_2 reaction order which implies that NO_2 inhibition is significant. The effect of NO_2 inhibition appears to be less severe with the addition of Pd, likely due to the metallic Pt formation in the alloyed particles. Finally, the addition of Pd did not lead to a greatly improved stability of the catalyst. The STEM images and corresponding particle size distributions suggest that Pd is not a textural promoter. Instead it may only act as an inert. When the bimetallic sample is aged at 750°C, the mean particle size of $Pt-Pd/Al_2O_3$ is larger than that of the Pt/Al_2O_3 aged at 750°C.

In the case of the model catalysts we see a major effect of Pd, but in both powder catalyst studies, Pd does not greatly improve the stability of Pt, and it does not appear to be a textural promoter. The evidence explaining both cases lies in the role of the vapor phase processes. Pd does not get emitted to the vapor phase, but our work has shown that it is possible for both Pt and Pd to be emitted to the support. Therefore, both species are mobile.

The dominant pathway for ripening is via surface diffusion. At modest temperatures, both Pt and Pd can be emitted from bimetallic nanoparticles to the support, but emission from PdO does not occur. We have shown that both Pt and Pt-Pd sinter, and the differences between the amounts of sintering are small. This has also been shown in previous work by Graham *et al*. [8] At higher temperatures (above 750°C), the vapor phase processes become significant. The oxidative aging of a Pt catalyst leads to the formation of volatile PtO_2 and anomalously large, faceted particles can form. In the case of Pt-Pd, Pd slows the emission and therefore decreases the vapor phase pathway.

Future Work

Future work should involve the implementation of a detailed mathematical model to help describe the model catalyst studies. It is not always feasible to perform experiments which explore the different aspects of aging. A mathematical model should be developed which can predict rates of sintering and rates of emission. The model must be validated by comparing it to experiments to ensure that it correctly models the process. To develop the model, each process (ripening and emission) should be studied by itself. To explore just the ripening process without emission, experiments could be performed on Pd model catalysts in hydrogen because this will not cause the loss of any Pd, but Pd does sinter in reducing atmospheres. To study the emission process without having any sintering, thin films of metal can be used. The goal would be to use EDS to determine the loss of metal on the thin film sample while keeping the film intact. Once the film starts to break up and separate, the surface area becomes much harder to estimate. The film should be as thick as possible while still being electron transparent. The exact emission rates could be quantified by using 100Å thin films of Pt and 50% Pt-50% Pd. The ultimate goal of these mathematical models would be to use them to predict sintering and emission rates on different types of samples. This would provide great insight to the processes governing catalyst aging.

In addition to implementing the mathematical models, another set of mobility studies could be performed in future work. One way would be to use a mask and deposit Pt on only a fraction of the TEM grid and Pd on another portion of the grid, leaving a blank area between the two metals. TEM and STEM could be used to determine whether or not the Pt and/or Pd

migrates to other areas of the grid. The experiments could be done in an open boat with the air flowing above the boat as well as in a closed boat situation where emission would be reduced. If migration did occur by either the Pt or Pd or both, it could be determined whether it was a surface process or vapor phase process. Another way to study mobility would be to deposit Pt on top of a grid containing PdO. The Pd sample would have been aged under oxidizing conditions to create PdO before the deposition. Then the sample could be aged for short intervals to study the role of the Pt on the PdO. The sample would need to be imaged between each aging step and an EDS map would need to be acquired to distinguish between Pt and Pd on the sample. We hypothesize that at some point during the aging treatments the Pt would combine with PdO and make the Pd metallic. It would be very interesting to determine if Pt could make once oxidized palladium metallic, and this would provide better understanding of what happens when Pt and Pd catalysts are physically mixed and aged.

Another set of experiments that should be done in future work would involve adding water vapor to the gas stream since DOCs are exposed to such conditions. A study should be done also to investigate the role of the partial pressure of oxygen. Some of the previous work discussed in the literature has used lower oxygen partial pressures than the 21% that is present in air. [8] Both conditions are valid, however, for DOCs. Therefore, it is important to understand the effect that differing amounts of oxygen may have.

Other future work could involve studying the role of the support. We have explored the ways in which Pd modifies Pt catalysts, but what effect, if any, does the support have on the sintering and emission mechanisms?

A fundamental understanding of the role of Pd on the catalytic activity and long-term performance of Pt catalysts has been gained, but there are many more possibilities of exciting work to be done related to diesel oxidation catalysts.

Appendix

The following is based on the extended abstract to be published in Microscopy and Microanalysis.

Johns, T.R., Gaudet, J.R., Peterson, E.J., Miller, J.T., Kim, C.H., Balogh, M.P., Datye, A.K., *Microstructure of Bimetallic Pt-Pd Nanoparticles Under Working Conditions*, Microscopy and Microanalysis, 2013. *(submitted February 2013)*

Microstructure of Bimetallic Pt-Pd Nanoparticles Under Working Conditions

Tyne R. Johns[1], Jason R. Gaudet[1,2], Eric J. Peterson[1], Jeffrey T. Miller[3], Chang H. Kim[4], Michael P. Balogh[4] and Abhaya K. Datye[1]

[1.] University of New Mexico, Department of Chemical & Nuclear Engineering, Albuquerque, NM, USA
[2.] University of Michigan, Department of Chemical Engineering, Ann Arbor, MI, USA
[3.] Argonne National Laboratory, Advanced Photon Source, Argonne, IL, USA
[4.] General Motors Global R&D, Chemical and Materials Systems Lab, Warren, MI, USA

Diesel oxidation catalysts (DOCs) are currently composed of platinum (Pt) and palladium (Pd). Pt catalysts are very active, but Pt sinters and has poor durability under oxidizing conditions. Reports in the literature show that Pd improves the durability of Pt catalysts but it has been unclear how Pd enhances the durability and performance of these catalysts. [6, 20] Esparza *et al.* demonstrated that core-shell Pt-Pd structures with a surface Pd layer could be prepared via colloidal routes. [37] Ezekoye *et al.* suggested that in their aged Pt-Pd catalysts, particles under 2.5 nm were primarily Pt-rich while those greater than 2.5 nm were Pd-rich. [6] However, it is important to study these catalysts under oxidizing conditions, as encountered in diesel oxidation catalysts. Hence, the extent of alloying during working conditions, how Pd modifies Pt, and whether Pd is present as a surface layer or as Pd, needs further study by HRTEM and EDS. Aging under oxidizing conditions may change the morphology, in which case the core-shell structures may not be stable under working conditions.

Using incipient wetness impregnation, we prepared 0.8 wt. % monometallic Pt and Pd

catalysts and a 1.3 wt. % Pt-Pd catalyst (40:60 atomic ratio) on two supports: La-stabilized alumina and γ-alumina. The Pt and Pd loadings were determined via energy dispersive X-ray spectroscopy (EDS). The samples were calcined in ambient air in a box furnace at 600°C for 4 hr, reduced in flowing 7% H_2/N_2 in a quartz tube furnace at 550°C for 2 hr, then aged in ambient air in a box furnace at 750°C for 10 hr. The catalysts in this state are referred to as "aged." A portion of each catalyst was reduced in 7% H_2/N_2 for 1 hr at 250°C, and these catalysts are referred to as "aged plus reduced."

A JEOL 2010F 200kV FASTEM FEG (field emission gun) TEM/STEM ((scanning) transmission electron microscope) was used to acquire high angle annular dark field (HAADF) images. For compositional analysis by EDS, we used a probe size of 1.0 nm to get adequate counting statistics. For high resolution compositional mapping, we also used a JEOL JEM 2100F AC (aberration-corrected STEM). The nominal point resolution and ultimate probe size for this instrument was similar to that of the JEOL 2010F, but the aberration corrector provides a much higher probe current for EDS analysis.

STEM/EDS was performed on the aged plus reduced La-alumina-supported catalysts. STEM results showed that the Pt-Pd/La-Al_2O_3 had a bimodal distribution of particle sizes. Figure 47 shows two images taken at different magnifications, which shows a dispersed phase coexisting with large bimetallic nanoparticles. The overall composition of this sample was 38 at. % Pt and 62 at. % Pd, as determined by EDS. However, the average composition of the large metallic particles was Pt-rich. It was important to identify the dispersed phase in the bimetallic catalyst to help us explain the discrepancy between the overall EDS analysis and the analysis of the large particles. EDS mapping allowed us to derive the average composition of the particles, as well as the dispersed phase. A spectrum image was obtained, and specific regions of the image could then be chosen and a spectrum derived for all the pixels in the chosen area. A sum spectrum was obtained which determined the composition over the entire image. Then the residual dispersed phase could be obtained by subtracting the region around each large particle from the sum spectrum. It was found that the residual contained 72 at. % Pd which suggests that the dispersed phase in these catalysts is Pd-rich while the large bimetallic particles are Pt-rich.

Figure 48 shows the Pt-Pd/La-Al_2O_3 catalyst after aging in air at 750°C for 10 hr and reduction at 250°C in 7% H_2/N_2 for 1 hr. The different areas shown in the figure were analyzed using EDS. A sum spectrum was taken which showed a composition of 74 at. % Pt and 26 at. % Pd, as shown in the table provided in Figure 48. The individual regions shown in Figure 48 were also analyzed, and the composition of Pt and Pd in these areas are also shown in the table. Pd was only slightly richer on the surface of the nanoparticle (31% vs. 26%), which shows that under working conditions, these catalysts do not form a core-shell morphology. These results were corroborated with EXAFS, XANES, and XRD. Our results suggest that Pd does not significantly slow down the rate of sintering of Pt, and large Pt particles that are alloyed with Pd, are seen on the aged catalyst.

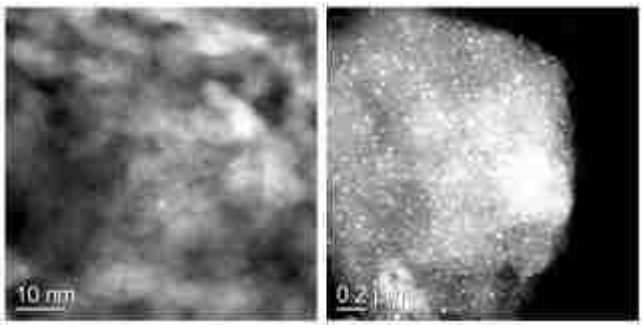

Figure 47. STEM image of (a) dispersed phase and (b) large particles in the aged plus reduced Pt-Pd/La-Al_2O_3 catalyst.

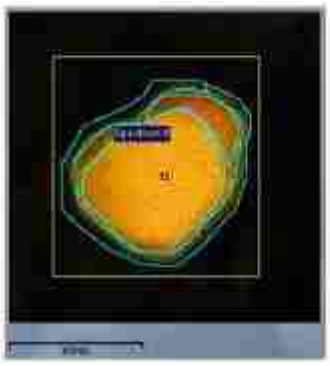

Spectrum	Wt % Pd	Wt % Pt	At % Pd	At % Pt
Sum	16.1	83.9	26.1	73.9
Perimeter	20.0	80.0	31.4	68.6
Top	16.6	83.4	26.7	73.3
Central	15.7	84.3	25.5	74.5
Left	14.2	85.8	23.3	76.7

Figure 48. AC-STEM image of a Pt-Pd/La-Al_2O_3 catalyst aged in air at 750°C for 10 hr and reduced at 250°C in 7% H_2/N_2 for 1 hr with superimposed results from EDS mapping.

Financial Support: NSF GOALI CBET-1067803, NSF IGERT DGE-0504276, and NSF PIRE OISE-0730277. The EDS spectral analysis was performed at General Motors Global R&D.

The following is based on the extended abstract published in Microscopy and Microanalysis.

Johns, T.R., DeLaRiva, A.T., Goeke, R.S., Thüne, P.C., Niemantsverdriet, J.W. (Hans), Datye, A.K., *Adatom Emission from Nanoparticles: Implications for Ostwald Ripening*, Microscopy and Microanalysis, 2011. 17 (Suppl. 2): p. 1692-1693.

Adatom Emission from Nanoparticles: Implications for Ostwald Ripening

T.R. Johns[1], A.T. De La Riva[1], R.S. Goeke[2], P.C. Thüne[3], J.W. Niemantsverdriet[3], and A.K. Datye[1]

[1]Department of Chemical and Nuclear Engineering and Center for Micro-Engineered Materials, University of New Mexico, Albuquerque, NM 87131
[2]Sandia National Laboratories, New Mexico, PO Box 5800, Albuquerque, NM 87185
[3]Schuit Institute of Catalysis, Department of Inorganic Chemistry and Catalysis, Eindhoven University of Technology, P.O. Box 513, 5600 MB Eindhoven, The Netherlands

Currently, precious metals such as Pt, Pd, and Rh are used in catalytic converters for treatment of exhaust gases from gasoline and diesel engines. These catalysts help remove pollutants, such as nitrogen oxides as well as CO and hydrocarbons, all of which result in smog and respiratory problems in urban environments. The supplies of precious metals are limited worldwide, but there is increasing demand for clean energy. Hence, there is a need to develop more active catalysts that provide long-term stable performance at elevated temperatures with minimal use of precious metals such as Pt. A serious problem facing catalysts is the loss of activity during use. The primary mechanism by which automotive catalysts lose activity is through growth of nanoparticles, via a process known as Ostwald ripening. [12] Several research groups have shown that Pt sinters readily under oxidizing conditions, leading to poor durability. [4, 8, 12] The restructuring of Pt under oxidizing conditions can be dramatic, as reported by Wu and Phillips, but Graham et al. demonstrated that addition of Pd to Pt led to improved stability. [8, 14]

In this work, we have used model catalysts to study the emission of atoms from nanoparticles, one of the key steps in Ostwald ripening. Electron beam evaporation was used to synthesize Pt, Pd, and 50% Pt-50% Pd samples on silica TEM grids. Each sample was first reduced in flowing 5% H_2/N_2 at 750˚C for 2 hours. Then each sample was aged in flowing air at 800˚C for 1.5 hours. Figure 49 shows HAADF-STEM (High-Angle Annular

Dark Field Scanning Transmission Electron Microscopy) images of the Pt and the bimetallic sample before and after aging. The Pt-Pd bimetallic sample showed significant growth in particle size after aging and a dramatic drop in the number of particles per square micron, whereas the Pt-only sample showed fewer particles but no significant particle growth. We determined the mass of metal on each sample assuming spherical particles and found that the effective thickness of the Pt layer decreased from 2.4 Å to 1.3 Å, which amounts to a 47% decrease in the mass of Pt. In contrast, the Pt-Pd sample lost only 9% of its mass. Since the loss of the metal is caused by emission of atoms, which is related to the vapor pressure of the metal (or metal oxide complex), the results show a significant decrease in atom emission due to the presence of Pd in the Pt. The vapor pressure of Pt-Pd alloys has been studied in the literature and it was reported that the system shows only a modest degree of non-ideality, implying that the drop in vapor pressure should at most be 50%, while we see over 80% decrease in metal emission rates.

The composition of the bimetallic sample determined from EDS (Energy Dispersive X-ray Spectroscopy) before aging was determined to be 39.4% Pt and 60.6% Pd. After aging, the composition was 32.7% Pt and 67.3% Pd. The images show that the nanoparticles remained in the metallic state, with only a few instances where a palladium oxide phase segregated from the Pt-Pd alloy. The similarity of compositions of the individual nanoparticles after aging to those before aging is very surprising since Pt is known to form a volatile metal oxide, but Pd is not. These results are intriguing because they imply that both Pt and Pd can be transported under oxidizing conditions. We have planned in-situ TEM experiments to study Pt and Pd mobility under oxidizing conditions, and further work is underway to study the role of the oxide support. These model catalyst studies shed light on the atomic scale phenomena involved in Ostwald ripening of automotive catalysts.

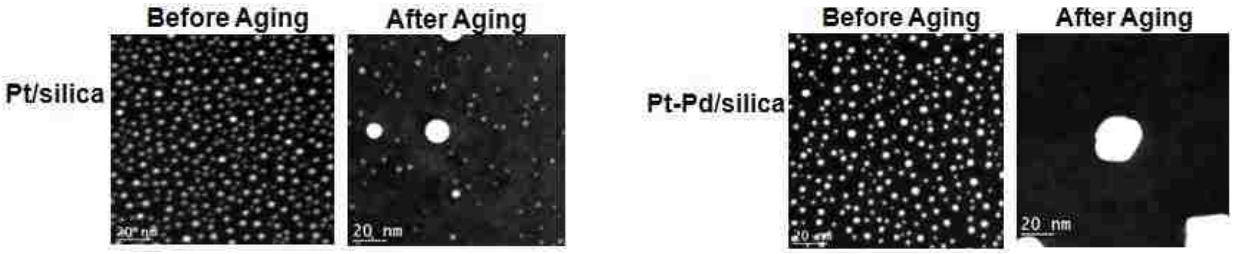

Figure 49. HAADF-STEM images before and after aging of the Pt and Pt-Pd samples.

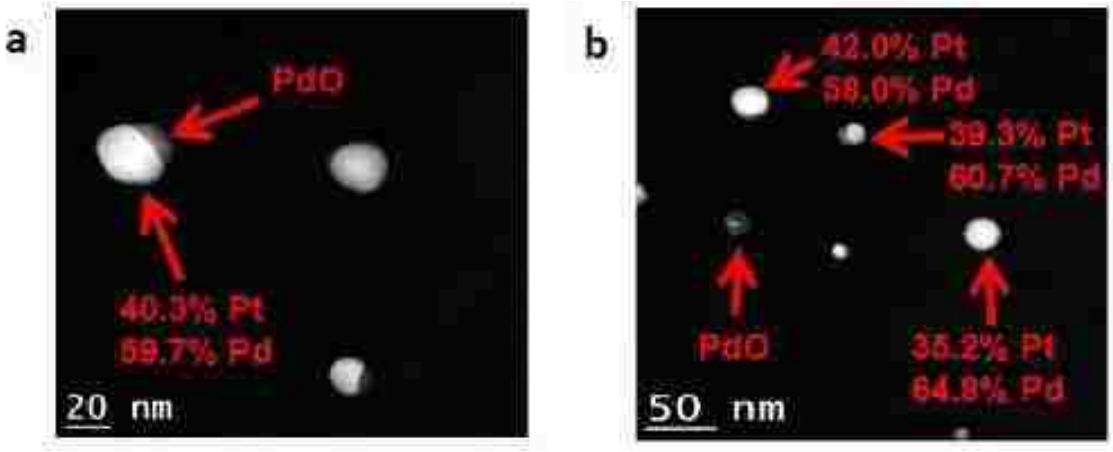

Figure 50. HAADF-STEM images of the bimetallic sample after aging show that compositions almost remained the same and nanoparticles remained metallic and alloyed.

This research was supported by NSF PIRE grant OISE-0730277 and made use of some of the facilities at Sandia National Laboratories. Sandia National Laboratories is a multi-program laboratory managed and operated by Sandia Corporation, a wholly owned subsidiary of Lockheed Martin Corporation, for the U.S. Department of Energy's National Nuclear Security Administration under contract DE-AC04-94AL85000.

References

1. Kallinen, K., et al. *Pt/Pd Diesel Oxidation Catalyst: A Study on the Properties Enhanced by the Use of Pd*. in *SAE Technical Paper 2009-26-0018*. 2009.
2. Watling, T.C., et al., *Development and Validation of a Pt-Pd Diesel Oxidation Catalyst Model.* SAE Int. J. Engines, 2012. 5(3).
3. Kim, C.H., et al., *The Effect of Pt-Pd Ratio on Oxidation Catalysts Under Simulated Diesel Exhaust.* SAE Technical Paper 2011-01-1134, 2011.
4. Adams, K.M. and G.W. Graham, *Impact of redox conditions on thermal deactivation of NOx traps for diesel.* Applied Catalysis B-Environmental, 2008. 80(3-4): p. 343-352.
5. Chen, M. and L.D. Schmidt, *Morphology and composition of Pt---Pd alloy crystallites on SiO_2 in reactive atmospheres.* Journal of Catalysis, 1979. 56(2): p. 198-218.
6. Ezekoye, O.K., et al., *Characterization of alumina-supported Pt and Pt-Pd NO oxidation catalysts with advanced electron microscopy.* Journal of Catalysis, 2011. 280(1): p. 125-136.
7. Graham, G.W., et al., *Coarsening of Pt particles in a model NOx trap.* Catalysis Letters, 2004. 93(3-4): p. 129-134.
8. Graham, G.W., et al., *Effect of alloy composition on dispersion stability and catalytic activity for NO oxidation over alumina-supported Pt-Pd catalysts.* Catalysis Letters, 2007. 116(1-2): p. 1-8.
9. Kaneeda, M., et al., *Improvement of thermal stability of NO oxidation Pt/Al_2O_3 catalyst by addition of Pd.* Applied Catalysis B-Environmental, 2009. 90(3-4): p. 564-569.
10. Morlang, A., et al., *Bimetallic Pt/Pd diesel oxidation catalysts - Structural characterisation and catalytic behaviour.* Applied Catalysis B- Environmental, 2005. 60(3-4): p. 191-199.
11. Mulla, S.S., et al., *Reaction of NO and O_2 to NO_2 on Pt: Kinetics and catalyst deactivation.* Journal of Catalysis, 2006. 241(2): p. 389-399.
12. Simonsen, S.B., et al., *Direct Observations of Oxygen-induced Platinum Nanoparticle Ripening Studied by In Situ TEM.* Journal of the American Chemical Society, 2010. 132(23): p. 7968-7975.
13. Simonsen, S.B., et al., *Ostwald ripening in a Pt/SiO(2) model catalyst studied by in situ TEM.* Journal of Catalysis, 2011. 281(1): p. 147-155.
14. Wu, N.L. and J. Phillips, *Reaction-Enhanced Sintering of Platinum Thin-Films During Ethylene Oxidation.* Journal of Applied Physics, 1986. 59(3): p. 769-779.
15. Wu, N.L. and J. Phillips, *Sintering of Silica-Supported Platinum Catalysts During Ethylene Oxidation.* Journal of Catalysis, 1988. 113(1): p. 129-143.
16. Zhou, Z.M., et al., *Durability study of Pt-Pd/C as PEMFC cathode catalyst.* International Journal of Hydrogen Energy, 2010. 35(4): p. 1719-1726.
17. Kim, D.H., et al., *Relationship of Pt particle size to the NOx storage performance of thermally aged Pt/BaO/Al2O3 lean NOx trap catalysts.* Industrial & Engineering Chemistry Research, 2006. 45(26): p. 8815-8821.

18. Kaya, S., et al., *On the Structure Sensitivity of CO Oxidation on Alumina Supported Pd-Pt Bimetallic Catalysts.* Turkish Journal of Chemistry, 2009. 33(1): p. 11-21.
19. Persson, K., et al., *Influence of molar ratio on Pd-Pt catalysts for methane combustion.* Journal of Catalysis, 2006. 243(1): p. 14-24.
20. Persson, K., K. Jansson, and S.G. Jaras, *Characterisation and microstructure of Pd and bimetallic Pd-Pt catalysts during methane oxidation.* Journal of Catalysis, 2007. 245(2): p. 401-414.
21. Ward, M.R., et al., *Nanostructural Studies of Fresh and Road-Aged Practical Pt/SiO2 and Pt-Pd/Al2O3 Diesel Oxidation Catalysts by using Aberration-Corrected (Scanning) Transmission Electron Microscopy.* Chemcatchem, 2012. 4(10): p. 1622-1631.
22. Gaudet, J.R., et al., *Improved Low Temperature CO Oxidation Performance of Pd Supported on La-Stabilized Alumina.* ACS Catalysis, 2013, submitted.
23. Li, M., et al., *Importance of re-oxidation of palladium by interaction with lanthana for propane combustion over Pd/Al2O3 catalyst.* Catalysis Today, 2013. 201: p. 19-24.
24. Alcock, C.B. and G.W. Hooper, *Thermodynamics of the Gaseous Oxides of the Platinum-Group Metals.* Proceedings of the Royal Society of London Series a-Mathematical and Physical Sciences, 1960. 254(1279): p. 551-561.
25. Moodley, P., et al., *Is there a correlation between catalyst particle size and CNT diameter?* Carbon, 2009. 47(8): p. 2002-2013.
26. Ravel, B., *ATOMS: crystallography for the X-ray absorption spectroscopist.* Journal of Synchrotron Radiation, 2001. 8: p. 314-316.
27. Ankudinov, A.L., et al., *Real-space multiple-scattering calculation and interpretation of x-ray-absorption near-edge structure.* Physical Review B, 1998. 58(12): p. 7565-7576.
28. Kittel, C., *Introduction to Solid State Physics*. 8th ed. 2005, Hoboken, NJ: John Wiley & Sons.
29. Waser, J., H.A. Levy, and S.W. Peterson, *THE STRUCTURE OF PDO.* Acta Crystallographica, 1953. 6(7): p. 661-663.
30. *International Tables for Crystallography, Volume A: Space Group Symmetry*. 5th ed, ed. T. Hahn. 2002: Kluwer Academic Publishers. 938.
31. Persson, K., et al., *Catalytic combustion of methane over bimetallic Pd-Pt catalysts: The influence of support materials.* Applied Catalysis B-Environmental, 2006. 66(3-4): p. 175-185.
32. Persson, K., et al., *Influence of molar ratio on Pd-Pt catalysts for methane combustion.* Journal of Catalysis, 2006. 243(1): p. 14-24.
33. Persson, K., et al., *Stability of palladium-based catalysts during catalytic combustion of methane: The influence of water.* Applied Catalysis B-Environmental, 2007. 74(3-4): p. 242-250.
34. Darby, J.B. and K.M. Myles, *Thermodynamic Study of Solid Pd-Pt Alloys.* Metallurgical Transactions, 1972. 3(3): p. 653-657.
35. Matyi, R.J., L.H. Schwartz, and J.B. Butt, *Particle-Size, Particle-Size Distribution, and Related Measurements of Supported Metal-Catalysts.* Catalysis Reviews-Science and Engineering, 1987. 29(1): p. 41-99.

36. Xu, Q., et al., *The Sintering of Supported Pd Automotive Catalysts.* Chemcatchem, 2011. 3(6): p. 1004-1014.
37. Esparza, R., et al., *Structural Characterization of Pt-Pd Core-Shell Nanoparticles by Cs-Corrected STEM.* Journal of Nanoparticle Research, 2013. 15(1).
38. Challa, S.R., et al., *Relating Rates of Catalyst Sintering to the Disappearance of Individual Nanoparticles during Ostwald Ripening.* Journal of the American Chemical Society, 2011. 133(51): p. 20672-20675.
39. Johns, T.R., et al., *Microstructure of Bimetallic Pt-Pd Catalysts Under Oxidizing Conditions.* ChemCatChem, 2013. DOI 10.1002/cctc.201300181.
40. Hermans, P.M.J.A., *High-Temperature Volatilisation of Catalytically Active Metals Supported on Alumina*, in *Department of Radiochemistry of the Interfaculty Reactor Institute*. 2004, Delft University of Technology: Delft. p. 172.
41. Hohenberg, P. and W. Kohn, *Inhomogeneous Electron Gas.* Physical Review B, 1964. 136(3B): p. B864-B871.
42. Kresse, G. and J. Furthmuller, *Efficiency of ab-initio total energy calculations for metals and semiconductors using a plane-wave basis set.* Computational Materials Science, 1996. 6(1): p. 15-50.
43. Kresse, G. and J. Hafner, *Ab-Initio Molecular-Dynamics for Open-Shell Transition-Metals.* Physical Review B, 1993. 48(17): p. 13115-13118.
44. Kresse, G. and J. Hafner, *Norm-Conserving and Ultrasoft Pseudopotentials for First-Row and Transition-Elements.* Journal of Physics-Condensed Matter, 1994. 6(40): p. 8245-8257.
45. Perdew, J.P. and Y. Wang, *Accurate and Simple Analytic Representation of the Electron-Gas Correlation-Energy.* Physical Review B, 1992. 45(23): p. 13244-13249.
46. Blochl, P.E., *Projector Augmented-Wave Method.* Physical Review B, 1994. 50(24): p. 17953-17979.
47. Kresse, G. and D. Joubert, *From ultrasoft pseudopotentials to the projector augmented-wave method.* Physical Review B, 1999. 59(3): p. 1758-1775.
48. Pearson, W.B., *Handbook of Lattice Spacings and Structures of Metals*. 1 ed. Vol. 2. 1967: Pergamon Press Ltd. 1446.
49. Abild-Pedersen, F. and M.P. Andersson, *CO absorption energies on metals with correction for high coordiantion adsorption sites - A density functional theory study.* Surface Science, 2007. 601(7): p. 1747-1753.
50. Halevi, B., et al., *Aerosol-Derived Bimetallic Alloy Powders: Bridging the Gap.* J. Phys. Chem. C, 2010(Copyright (C) 2010 American Chemical Society (ACS). All Rights Reserved.): p. ACS ASAP.
51. Makov, G. and M.C. Payne, *Periodic Boundary-Conditions in Ab-Initio Calculations.* Physical Review B, 1995. 51(7): p. 4014-4022.
52. Neugebauer, J. and M. Scheffler, *Adsorbate-Substrate and Adsorbate-Adsorbate Interactions of Na and K Adlayers on Al(111).* Physical Review B, 1992. 46(24): p. 16067-16080.
53. Mulla, S.S., et al., *NO_2 inhibits the catalytic reaction of NO and O_2 over Pt.* Catalysis Letters, 2005. 100(3-4): p. 267-270.